CLICdp-Note-2018-005
17 December 2018

A detector for CLIC: main parameters and performance

Dominik Arominski[a,b], Jean-Jacques Blaising[c], Erica Brondolin[a], Dominik Dannheim[a], Konrad Elsener[a], Frank Gaede[d], Ignacio García García[a,e], Steven Green[f], Daniel Hynds[a,1], Emilia Leogrande[a,*], Lucie Linssen[a], John Marshall[g,2], Nikiforos Nikiforou[a,3], Andreas Nürnberg[a,4], Estel Perez-Codina[a], Marko Petrič[a], Florian Pitters[a,h], Aidan Robson[i,5], Philipp Roloff[a], André Sailer[a,*], Ulrike Schnoor[a], Frank Simon[j], Rosa Simoniello[a,6], Simon Spannagel[a], Rickard Stroem[a], Oleksandr Viazlo[a], Matthias Weber[a,*], Boruo Xu[f]

On behalf of the CLICdp Collaboration

[a] *CERN, Geneva, Switzerland,* [b] *Warsaw University of Technology, Warsaw, Poland,* [c] *Laboratoire d'Annecy-le-Vieux de Physique des Particules, Annecy-le-Vieux, France,* [d] *DESY, Hamburg, Germany,* [e] *IFIC, Universitat de Valencia/CSIC, Valencia, Spain,* [f] *University of Cambridge, Cambridge, United Kingdom,* [g] *University of Warwick, Coventry, United Kingdom,* [h] *Technische Universität Wien, Vienna, Austria,* [i] *University of Glasgow, Glasgow, United Kingdom,* [j] *Max-Planck-Institut für Physik, Munich, Germany*

Abstract

Together with the recent CLIC detector model CLICdet a new software suite was introduced for the simulation and reconstruction of events in this detector. This note gives a brief introduction to CLICdet and describes the CLIC experimental conditions at 380 GeV and 3 TeV, including beam-induced backgrounds. The simulation and reconstruction tools are introduced, and the physics performance obtained is described in terms of single particles, particles in jets, jet energy resolution and flavour tagging. The performance of the very forward electromagnetic calorimeters is also discussed.

*Corresponding Editor
[1]Now at Nikhef, Amsterdam, The Netherlands
[2]Formerly at University of Cambridge, Cambridge, United Kingdom
[3]Now at University of Texas at Austin, Austin, Texas, USA
[4]Now at Karlsruhe Institute of Technology, Karlsruhe, Germany
[5]Also at CERN, Geneva, Switzerland
[6]Now at Johannes Gutenberg Universität Mainz, Mainz, Germany

Contents

1. Introduction

A state-of-the-art detector, built using cutting-edge technology and optimised through simulation, is crucial to exploit the physics potential of CLIC. Two detector models were previously defined, based on concepts for the ILC detectors and adapted for the higher centre-of-mass energies at CLIC. The CLIC_ILD and CLIC_SiD models were used for physics studies in the CDR [1]. Based on the lessons learnt for the CDR as well as the experience from several additional optimisation studies, a new model, dubbed CLICdet, has been designed for the forthcoming physics benchmark studies. The CLICdet model is described in detail in [2]. A summary of the main parameters of CLICdet is given in Chapter 2. Chapter 3 gives an overview of CLIC experimental conditions linked to the characteristics of the beam and of the detector requirements.

In parallel to the development of a new detector design and its hardware technologies, the software chain for simulation and reconstruction has been re-designed. The simulated model of CLICdet has been implemented using the DD4hep detector description toolkit. The performances of the simulated CLICdet model with the new software chain have been assessed in terms of lower level physics observables, including flavour tagging and jet energy resolution. Performance results for CLIC operation at 380 GeV and 3 TeV are shown in Chapter 4.

2. CLICdet Layout and Main Parameters

2.1. Overview

The CLICdet layout follows the typical collider detector scheme of a vertex detector surrounding the beryllium beam pipe, a large tracker volume with barrel and disks of silicon sensors, and an ECAL and HCAL, all embedded inside a superconducting solenoid providing a 4 T field. The surrounding iron yoke is interleaved with muon chambers needed for a clean muon identification in complex events. A quarter-view of the cross section of CLICdet is shown in Figure 1, and an isometric view is presented in Figure 2. Key parameters of the CLICdet model are compared to CLIC_ILD and CLIC_SiD in Table 1.

An important change with respect to the CDR detector models concerns the location of the final focusing quadrupole (QD0): to improve the angular coverage of the HCAL endcap to reach smaller polar angles, this quadrupole is moved outside of the detector into the tunnel. Nevertheless, the QD0 must be as close as possible to the interaction point (IP). The overall length of CLICdet has been minimised by reducing the thickness of the iron yoke endcaps. The missing iron is compensated by a set of end coils, shown schematically in Figure 1.

Figure 3 shows a vertical cut-view of CLICdet installed on the interaction point, together with a section of accelerator tunnel on either side. The QD0 quadrupoles, located just outside of the detector at $L^* = 6\,\text{m}$ are also shown. L^* is the distance from the downstream end of QD0 to the interaction point. The next magnetic elements, further upstream, are located outside the tunnel section covered by the drawing.

Table 1: Comparison of key parameters of the different CLIC detector concepts. CLIC_ILD and CLIC_SiD values are taken from the CDR [1]. The inner radius of the electromagnetic calorimeter (ECAL) is given by the smallest distance of the calorimeter to the main detector axis. For the hadronic calorimeter (HCAL), materials are given separately for the barrel and the endcap.

Concept	CLICdet	CLIC_ILD	CLIC_SiD
Be vacuum pipe inner radius [mm]	29.4	29.4	24.5
Be vacuum pipe wall thickness [mm]	0.6	0.6	0.5
Vertex technology	Silicon	Silicon	Silicon
Vertex inner radius [mm]	31	31	27
Tracker technology	Silicon	TPC/Silicon	Silicon
Tracker half length [m]	2.2	2.3	1.5
Tracker outer radius [m]	1.5	1.8	1.3
ECAL technology	Silicon	Silicon	Silicon
ECAL absorber	W	W	W
ECAL radiation lengths	22	23	23
ECAL barrel r_{min} [m]	1.5	1.8	1.3
ECAL barrel Δr [mm]	202	172	139
ECAL endcap z_{min} [m]	2.31	2.45	1.66
ECAL endcap Δz [mm]	202	172	139
HCAL technology	Scintillator	Scintillator	Scintillator
HCAL absorber barrel / endcap	Fe / Fe	W / Fe	W / Fe
HCAL nuclear interaction lengths	7.5	7.5	7.5
HCAL barrel r_{min} [m]	1.74	2.06	1.45
HCAL barrel Δr [mm]	1590	1238	1177
HCAL endcap z_{min} [m]	2.45	2.65	1.80
HCAL endcap Δz [mm]	1590	1590	1595
Solenoid field [T]	4	4	5
Solenoid length [m]	8.3	8.3	6.5
Solenoid bore radius [m]	3.5	3.4	2.7
Yoke with muon system barrel r_{min} [m]	4.46	4.40	3.91
Yoke with muon system barrel Δr [mm]	1.99	2.59	3.09
Yoke with muon system endcap z_{min} [m]	4.18	4.24	3.40
Yoke with muon system endcap Δz [mm]	1.52	1.96	2.81
Overall height [m]	12.9	14.0	14.0
Overall length [m]	11.4	12.8	12.8
Overall weight [t]	8100	10800	12500

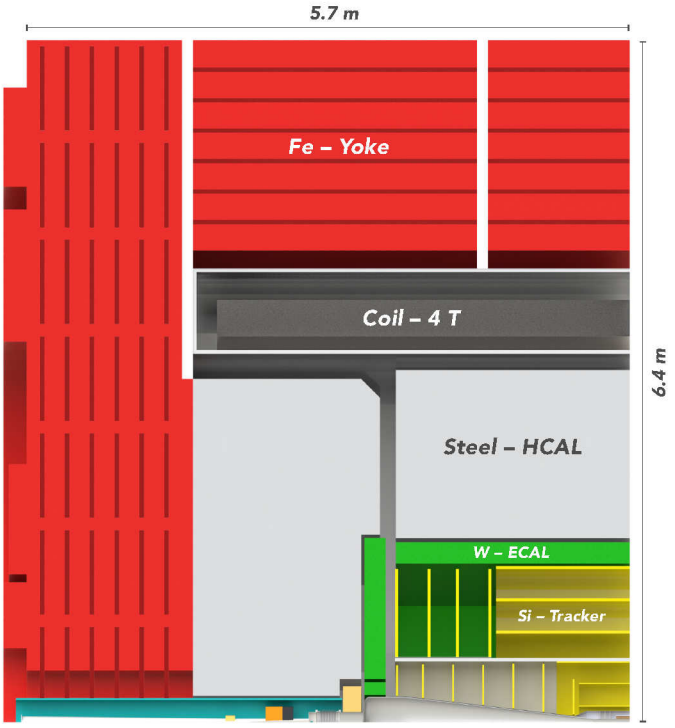

Figure 1: Longitudinal cross section showing a quadrant of CLICdet (side view) [2]. The structures shown on the left of the image (i.e. outside of the yoke) represent the end coils.

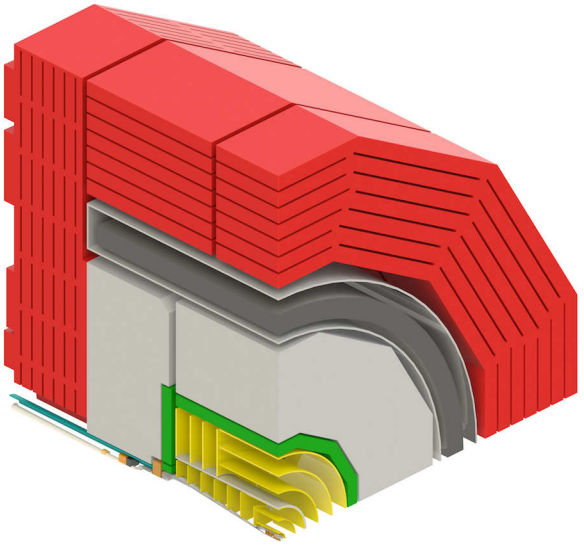

Figure 2: Isometric view of CLICdet.

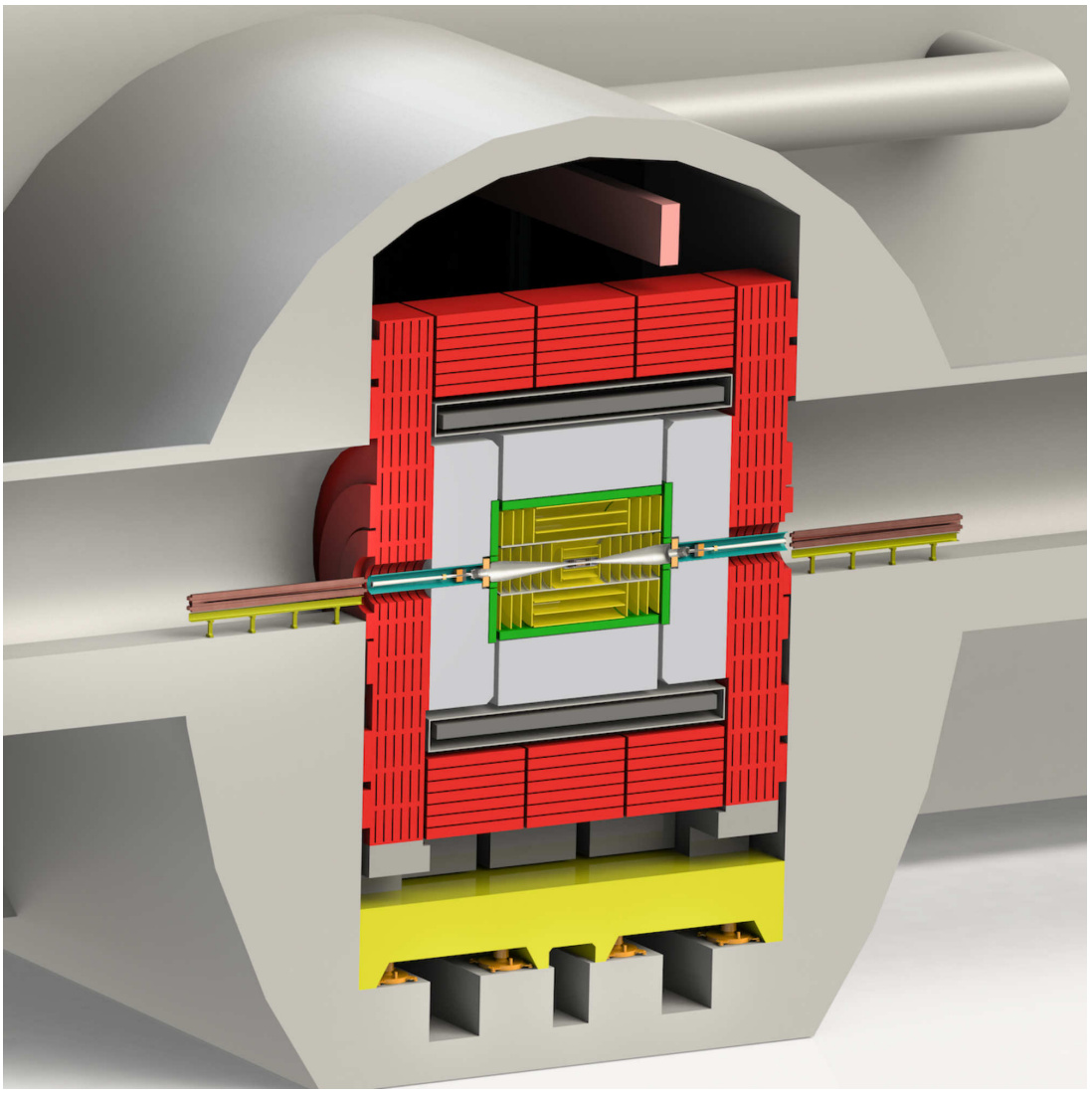

Figure 3: Cut view of CLICdet on the interaction point. The QD0 quadrupoles in the accelerator tunnel are visible on both sides of the detector.

2.2. Vertex and Tracker

The vertex detector in CLICdet, similarly to the CDR detector models, consists of a cylindrical barrel detector closed off in the forward directions by "disks". The layout is based on double layers, i.e. two sensitive layers fixed on one support structure, in both barrel and forward region. The barrel consists of three double layers. In the forward region, the three "disks" are split up in 8 segments which are arranged to create a "spiral". This spiral geometry allows efficient air-flow cooling of the vertex detector. The air-flow imposes that both spirals have the same sense of rotation – this leads to an asymmetric layout of the vertex "disks". The vertex detector is built from modules of 50 µm thin silicon pixel detectors (plus an additional 50 µm thick ASIC) with a pixel size of $25 \times 25\ \mu m^2$.

Figure 4 shows the arrangement of the three vertex barrel layers and the forward spirals in the $X-Z$ plane, together with the vacuum tube and additional material representing supports and a surrounding air-guiding cylinder. An $X-Y$ section through the vertex barrel layers is shown in Figure 5, indicating the arrangement of modules as currently implemented in the simulation model of CLICdet. Appendix A contains further images indicating polar angles relevant for the efficiency studies.

The all-silicon tracker volume has a radius of 1.5 m and a half-length of 2.2 m. The main support tube, among other things needed to carry the weight of the vacuum tube and the vertex detector, has an inner and outer radius of 0.575 m and 0.600 m, respectively, and a half-length of 2.25 m. This support

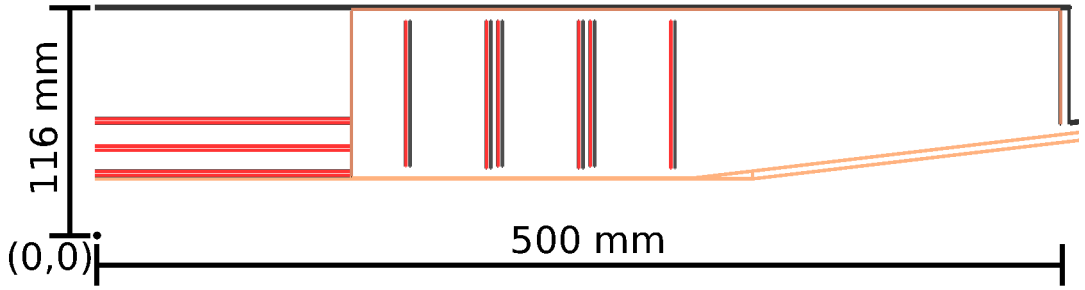

Figure 4: Sketch of the barrel and forward vertex detector region in the $X-Z$ plane. The vacuum tube is shown in yellow, sensors in red, support structures in black and cables in brown. Note that the spiral structure of the vertex forward disks is not visible in this cut view. However, due to the choice of the cut, the two middle disks appear "double" due to the small azimuthal overlap between modules.

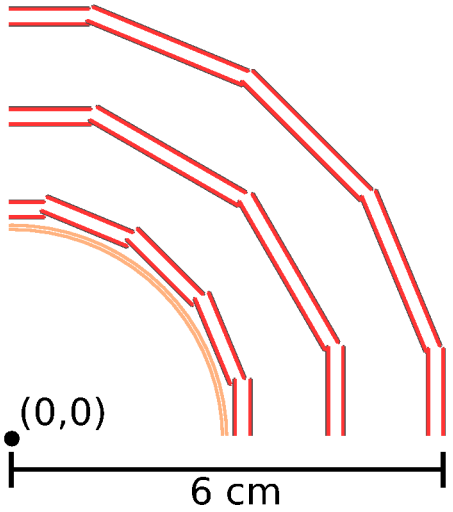

Figure 5: Sketch of the barrel vertex detector region in the $X-Y$ plane; colour coding as in Figure 4.

Table 2: Vertex and tracker pixels/strips, and assumed single point resolutions. The smaller numbers for each of the strips refer to the direction in the bending plane. Note that the tracker numbers in the second column are driven by occupancy studies [3], while the resolutions in the third column are the values currently used in the reconstruction software.

Subdetector	Layout sizes	Resolutions
Vertex (Barrel and Disks)	25 µm × 25 µm	3 µm × 3 µm
Inner Tracker Disk 1	25 µm × 25 µm	5 µm × 5 µm
Inner Tracker Disks 2–7	50 µm × 1 mm	7 µm × 90 µm
Outer Tracker Disks	50 µm × 10 mm	7 µm × 90 µm
Inner Tracker Barrel 1–2	50 µm × 1 mm	7 µm × 90 µm
Inner Tracker Barrel 3	50 µm × 5 mm	7 µm × 90 µm
Outer Tracker Barrel 1–3	50 µm × 10 mm	7 µm × 90 µm

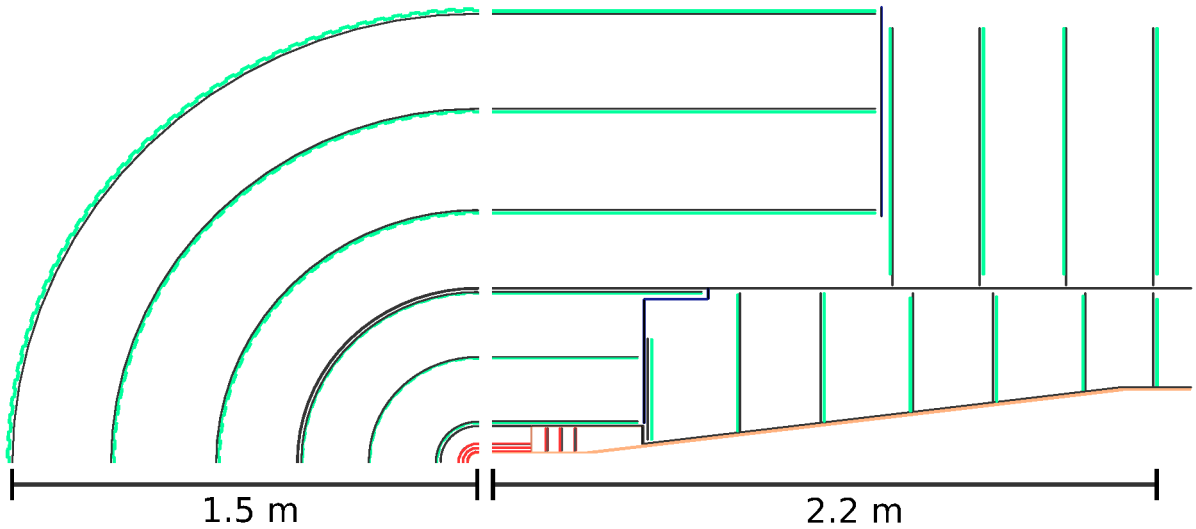

Figure 6: Layout of the tracking system in the $X-Y$ plane (left) and the $X-Z$ plane (right). Tracker sensors are shown in green, support material in black. The blue lines represent additional material (e.g. cables), which has only been added in critical regions.

tube effectively divides the tracker volume into two regions: the "Inner Tracker" and "Outer Tracker". The Inner Tracker contains three tracker barrel layers and, on each side of the barrel, seven inner tracker disks. The Outer Tracker is built from three large barrel layers complemented on either side by four outer tracker disks. The layout of the CLICdet tracker as implemented in the simulation model is shown in Figure 6. The sensors envisaged have a thickness of 200 µm including electronics and, in the simulation model, are assembled in modules either $15 \times 15\,\text{mm}^2$ or $30 \times 30\,\text{mm}^2$.

In reconstruction, the hits are smeared with Gaussian distributions in order to represent the single point resolution. A certain degree of charge sharing/cluster size is assumed when estimating resolutions from a given pixel/strip size – verifying these assumptions is part of an ongoing R&D programme. The σ values as used in reconstruction are given in Table 2.

When compared to CLIC_SiD, CLICdet has a much larger tracking system, in particular extending the forward region acceptance. The number of expected hits in CLICdet as a function of the polar angle θ is shown in Figure 7. The total material budget considering all elements up to the calorimeters is presented in Figure 8.

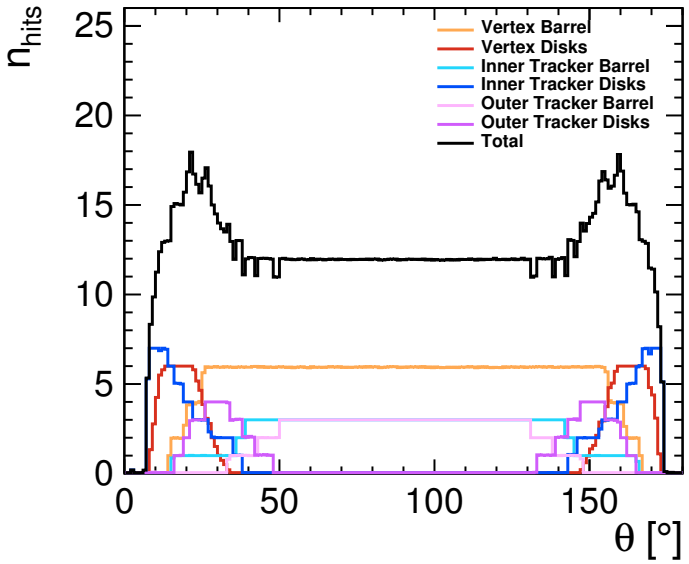

Figure 7: The coverage of the tracking systems with respect to the polar angle θ [2]. Shown is the mean number of hits created by 500 GeV muons in full simulation. Only primary muon hits are taken into consideration (hits from secondary particles are ignored). At least eight hits are measured for all tracks with a polar angle down to about 8°.

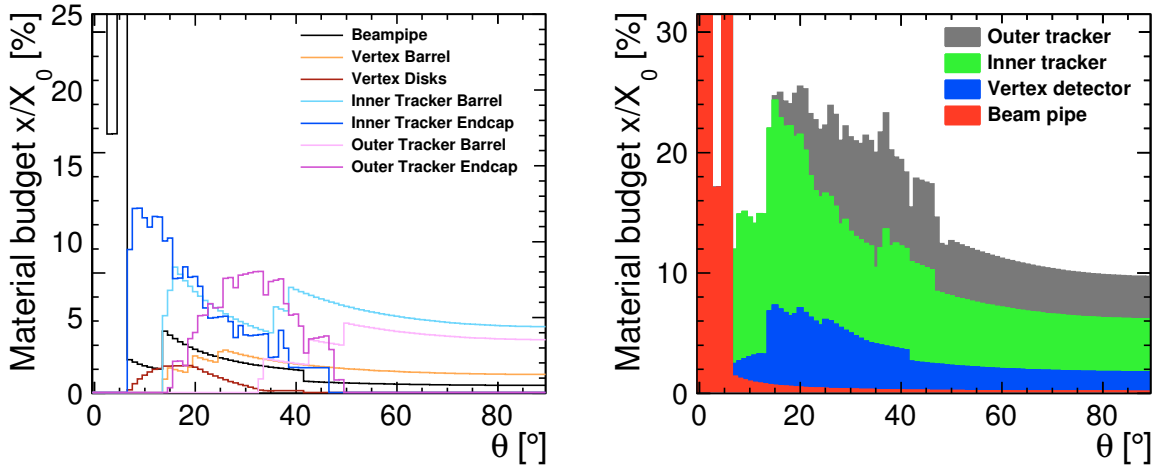

Figure 8: Material budget as a function of the polar angle and averaged over azimuthal angles, distinguished for the beam pipe and subdetectors in the tracking system (left) and stacked material budget of the different regions inside the tracking system (right). Contributions from sensitive layers, cables, supports and cooling are included in the respective regions.

2.3. Calorimetry

Calorimetry at CLIC is designed according to requirements given by the particle flow paradigm. An additional design criterion is good photon energy resolution over a wide energy range. The ECAL and HCAL barrel of CLICdet are arranged in dodecagons around the tracker volume. The endcap calorimeters are arranged to provide good coverage in the transition region, and maximum coverage to small polar angles. The overall dimensions of the calorimeters are given in Table 1.

The ECAL is a highly granular array of 40 layers of silicon sensors and tungsten plates. The 1.9 mm

tungsten plates, together with sensors and readout, add up to 22 radiation lengths. The lateral segmentation of the 300 µm thick sensors is chosen to be $5 \times 5\,\mathrm{mm}^2$. The present layout of the ECAL allows for excellent energy resolution (e.g. for high energy photons), see Section 4.2.1.

The HCAL is built from 60 layers of plastic scintillator tiles, read out by silicon photomultipliers, interleaved with 20 mm thick steel absorber plates. The scintillator tiles are 3 mm thick and have lateral dimensions of $3 \times 3\,\mathrm{cm}^2$. Together with tracker and ECAL, and using the Pandora particle-flow analysis software [4–6], jet energy resolutions in the order of 4% to 5% are obtained (see Section 4.2.3).

Earlier studies had shown that about 7.5 nuclear interaction lengths (λ_I) of depth are needed in the HCAL, in addition to the 1 λ_I from the ECAL [1]. The integrated thickness of the CLICdet calorimeters, in terms of nuclear interaction lengths λ_I, is shown in Figure 9.

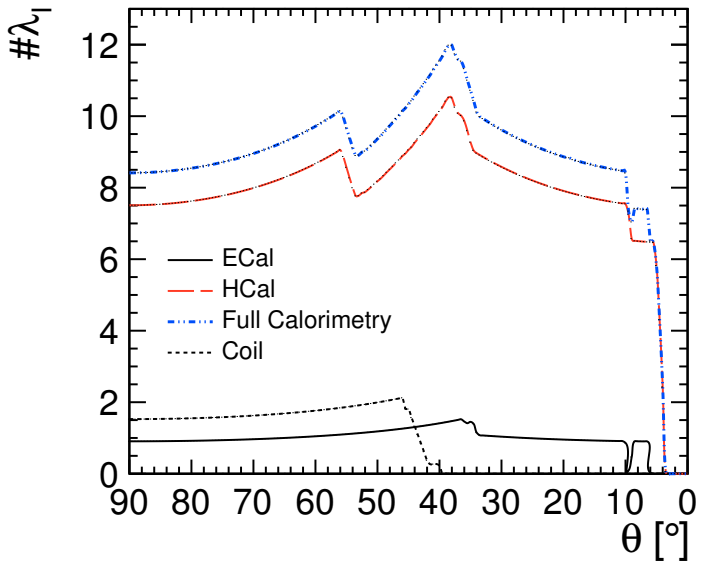

Figure 9: Nuclear interaction lengths λ_I in the calorimeters with respect to the polar angle θ [2]. The interaction length corresponding to the material of the superconducting coil is shown for completeness.

2.4. Muon Detector System

The muon system contains 6 layers of detectors interleaved with the yoke steel plates. In the barrel, a 7^{th} layer as close as possible to the coil is foreseen, which can also act as tail catcher for the calorimeter system. The layout of the muon system is shown in Figure 10.

As in the CDR, the muon detection layers are proposed to be built as RPCs with cells of $30 \times 30\,\mathrm{mm}^2$ (alternatively, crossed scintillator bars could be envisaged). The free space between yoke steel layers is 40 mm, which is considered generous given present-day technologies for building RPCs.

2.5. Very Forward Calorimeters LumiCal and BeamCal

Two smaller electromagnetic calorimeters close the very forward angular region of CLICdet: LumiCal, covering an angular range from 39 mrad to 134 mrad, and BeamCal, covering from 10 mrad to 46 mrad. The layout of the very forward region is shown schematically in Figure 11. Both calorimeters are built from 40 layers of 3.5 mm thick tungsten plates, interleaved with sensors. The readout electronics is located at the periphery of these calorimeters. LumiCal sensors will be 300 µm thick silicon pads, in a

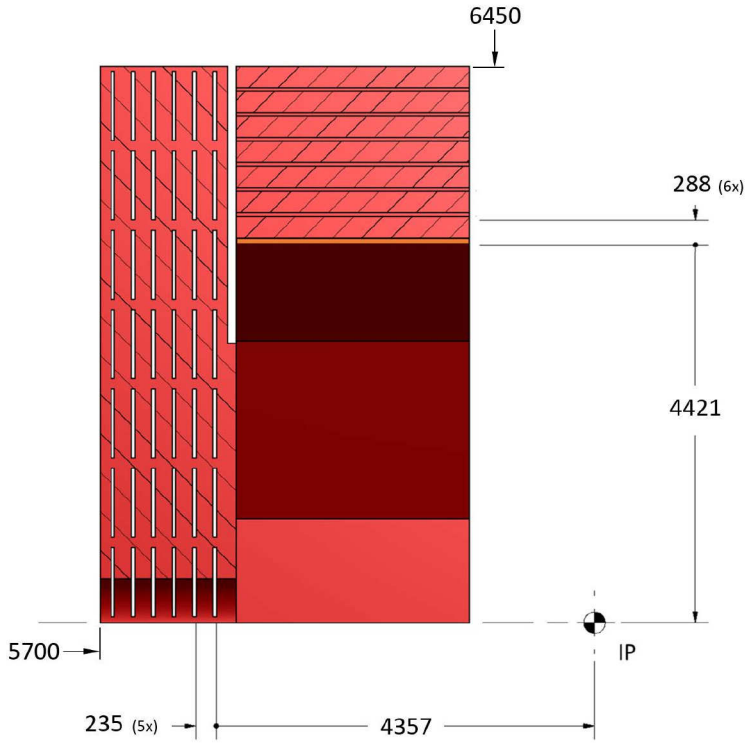

Figure 10: Schematic cross section of the muon system layout in the yoke of CLICdet [2].

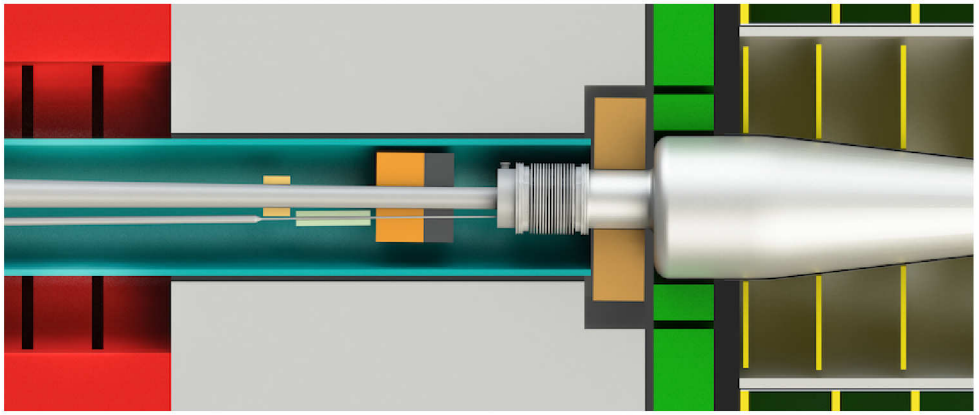

Figure 11: Layout of the forward region in CLICdet (top view) [2]. The LumiCal is shown in khaki, the BeamCal in orange. Downstream of LumiCal are the bellows of the vacuum system. A graphite cylinder is installed upstream of BeamCal – this allows one to considerably reduce backscattering from BeamCal into the central detector region.

layout optimised for high precision luminosity measurements using Bhabha events. The LumiCal sensor pads have a radial size of 3.75 mm and an azimuthal size of 7.5°. In the BeamCal, the sensors must be more radiation tolerant, but at the moment silicon sensors are used in the simulation model. The BeamCal cell sizes are constant in radius and $R\phi$ with about $8 \times 8\,\mathrm{mm}^2$.

3. Summary of CLIC Experimental Conditions and Detector Requirements

The design requirements for a detector at CLIC have been described in detail in the CDR [1, Chapter 2]. An updated summary, using beam optics parameters for the new default $L^* = 6\,\text{m}$, and with emphasis on the first stage of CLIC at 380 GeV centre-of-mass energy, is given here.

3.1. The CLIC Beam

The main parameters of the CLIC beam of relevance to the physics reach, to the beam–beam backgrounds at the IP and thus the detector design are summarised in Table 3 for the first CLIC energy stage, 380 GeV, and the ultimate high energy stage at 3 TeV [7].

The time structure of the CLIC beam, with bunch trains colliding every 20 ms, is very similar at 380 GeV and at 3 TeV. Bunches inside the trains are separated by 0.5 ns. The number of bunches per train is slightly larger at 380 GeV, and the number of particles per bunch is significantly larger at 380 GeV than at 3 TeV.

The beam–beam effects strongly vary with increasing centre-of-mass energy of CLIC. This fact manifests itself e.g. in the difference of the number of coherent and incoherent pairs produced, as well as the number of hadronic events produced by gamma-gamma interactions. As described in [1], this leads also to very different luminosity spectra at different energies, as illustrated in Figure 12: while there is a strong tail to lower energies at 3 TeV CLIC, the tail at 380 GeV is much less prominent. The fraction of luminosity in different regions of the luminosity spectrum, both for 380 GeV and 3 TeV, is given in Table 4.

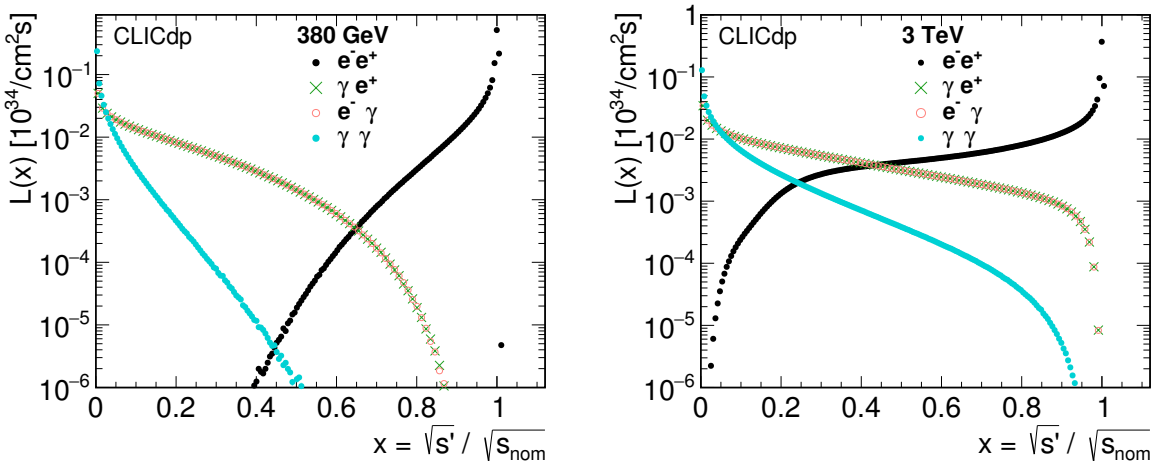

Figure 12: Luminosity distributions at 380 GeV (left) and at 3 TeV (right).

3.2. Beam-Induced Backgrounds

All the sources of beam related backgrounds, in particular for the 3 TeV stage of CLIC, have been discussed in detail in the CDR [1, Section 2.1.2]. Comparisons of background particle distributions at 380 GeV, direct hits in all subdetectors as well as indirect hits from secondary and backscattered particles are given in the following.

Background hits from coherent pairs, which are produced in large quantities and have high energy, are avoided by the design of the interaction region, and in particular the shape of the outgoing beam pipe: a cone with opening angle 10 mrad allows sufficient space for the coherent pairs to leave the detector

Table 3: The main parameters of the CLIC machine and background rates at the interaction point. The listed variables are: θ_c, the horizontal crossing angle of the beams at the IP; f_{rep}, the repetition frequency; n_b, the number of bunches per bunch train; Δt, the separation between bunches in a train; N, the number of particles per bunch; σ_x, σ_y, and σ_z, the bunch dimensions at the IP; β_x and β_y, the beta functions at the IP; L^*, the distance from the last quadrupole to the IP; $\mathscr{L}$, the design luminosity; $\mathscr{L}_{0.01}$, the luminosity with $\sqrt{s'} > 0.99\sqrt{s}$; $\Delta E/E$, the average fraction of energy lost through beamstrahlung; n_γ, the average number of beamstrahlung photons per beam particle; N_{coh}, the number of coherent pair particles per bunch crossing (BX); E_{coh}, the total energy of coherent pair particles per BX; N_{incoh}, the number of incoherent pair particles per BX; E_{incoh}, the total energy of incoherent pair particles per BX; and, n_{Had}, the number of $\gamma\gamma \to$ hadron events per BX for a $\gamma\gamma$ centre-of-mass energy threshold of $W_{\gamma\gamma} > 2\,\text{GeV}$. The background rates and energy releases are quoted excluding safety factors representing the simulation uncertainties.

Parameter	Units	$\sqrt{s} = 380\,\text{GeV}$	$\sqrt{s} = 3\,\text{TeV}$
θ_c	mrad	16.5	20
f_{rep}	Hz	50	50
n_b		352	312
Δt	ns	0.5	0.5
N		$5.2 \cdot 10^9$	$3.72 \cdot 10^9$
σ_x	nm	≈ 149	≈ 45
σ_y	nm	≈ 2.9	≈ 1
σ_z	µm	70	44
β_x	mm	8	7
β_y	mm	0.1	0.12
L^*	m	6	6
$\mathscr{L}$	$\text{cm}^{-2}\text{s}^{-1}$	$1.5 \cdot 10^{34}$	$5.9 \cdot 10^{34}$
$\mathscr{L}_{0.01}$	$\text{cm}^{-2}\text{s}^{-1}$	$0.9 \cdot 10^{34}$	$2.0 \cdot 10^{34}$
n_γ		1.4	2.0
$\Delta E/E$		0.08	0.25
N_{coh}		≈ 0	$6.1 \cdot 10^8$
E_{coh}	TeV	≈ 0	$2.1 \cdot 10^8$
N_{incoh}		$4.6 \cdot 10^4$	$2.8 \cdot 10^5$
E_{incoh}	TeV	$2.1 \cdot 10^2$	$2.1 \cdot 10^4$
n_{Had} ($W_{\gamma\gamma} > 2$ GeV)		0.17	3.1

region. The post-collision line is designed to transport these particles to the beam dump, together with the spent beam and the beamstrahlung photons.

Backscattering from the post-collision line and the main CLIC beam dumps, 315 m downstream of the IP, has been investigated [8]. The average flux of backscattered photons and neutrons hitting the detector area was found to be negligible.

Beam halo muons can be largely suppressed by optimising the beam delivery system, and in particular the collimation system. The expected level of halo muons traversing the detector should be easily handled by CLICdet, mainly due to the high granularity and timing resolution of the subdetector systems [1].

Incoherent pairs, produced from the interaction of real or virtual photons with individual particles of

Table 4: Fraction of luminosity above $\sqrt{s'}/\sqrt{s}$.

Fraction $\sqrt{s'}/\sqrt{s}$	380 GeV	3 TeV
> 0.99	60%	36%
> 0.90	90%	57%
> 0.80	97,6%	69%
> 0.70	99.5%	76.8%
> 0.50	99.99%	88.6%

the oncoming beam, can be produced at larger angles than coherent pairs, and are potentially a significant source of background hits, in particular in the vertex detector. The energy and angular distribution of the incoherent pairs at 380 GeV centre-of-mass energy are shown in Figure 13.

The interaction of real or virtual photons from the colliding beams can produce hadronic final states. These $\gamma\gamma \to$ hadron interactions can produce particles at a large angle to the beam line. The energy and angular distributions of these background particles are also shown in Figure 13. The impact of backgrounds is discussed in Section 3.4.

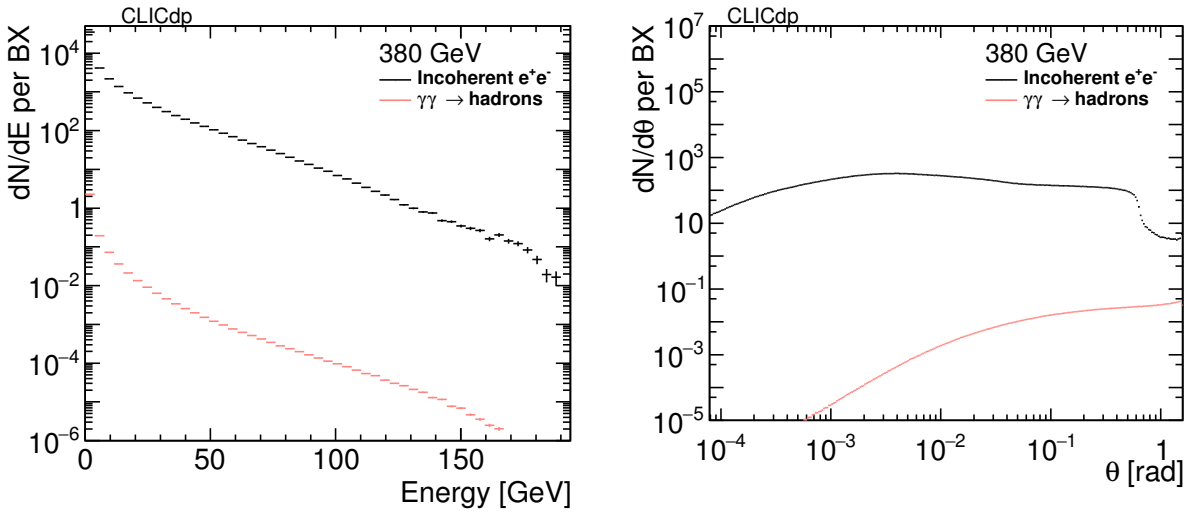

Figure 13: Energy distribution (left) and polar angle distribution (right) per BX of beam-induced backgrounds. Both figures are for CLIC at 380 GeV. Generated particle distributions are shown, no cuts other than the 2 GeV centre-of-mass threshold for $\gamma\gamma \to$ hadrons are applied.

3.3. Overview of Requirements for Physics Reconstruction

The detector requirements, in particular for a 3 TeV CLIC collider, have been described in detail in the CDR [1, Section 2.2]. Summarising the findings, from the perspective of the likely physics measurements at CLIC the detector requirements are:

- jet energy resolution of $\sigma_E/E \lesssim 5$–3.5% for light quark jet energies in the range 50 GeV–1 TeV;
- track momentum resolution of $\sigma_{p_T}/p_T^2 \lesssim 2 \cdot 10^{-5}\,\text{GeV}^{-1}$ for high momentum tracks;
- transverse impact parameter resolution $\sigma_{d_0}(p,\theta) = \sqrt{a^2 + b^2 \cdot \text{GeV}^2/(p^2 \sin^3(\theta))}$ with $a \lesssim 5$ µm, $b \lesssim 15$ µm;
- lepton identification efficiency: $> 95\%$ over the full range of energies;

- detector coverage for electrons down to very small angles.

3.4. Impact of Backgrounds on the Detector Requirements

The main beam-related backgrounds in the CLIC detector are from incoherent pairs, and particles from $\gamma\gamma \to$ hadron events. As discussed in the CDR, particles from incoherent pairs are the dominant backgrounds in the vertex and the very forward region. The particles from $\gamma\gamma \to$ hadrons are less forward-peaked and the dominant source of background in the silicon tracker and the calorimeters. As shown in Table 3, the number of background particles varies strongly with the CLIC centre-of-mass energy.

A detailed optimisation of the position of BeamCal, and the openings to allow for the incoming and outgoing beam pipes, had been performed at the time of the CDR and was not repeated for CLICdet. In the following, results from full simulation studies, thus including all multiple- and back-scattering effects, are demonstrating the impact of these beam-related backgrounds.

3.4.1. Impact on Vertex and Tracking Detectors

The dense core of particles from the incoherent pair background, spiralling near the beam axis due to the 4 T solenoid field, must not intercept any material of the detector. As shown in the CDR, at the 3 TeV stage of CLIC this imposes an inner radius of the beryllium beam pipe of 29.4 mm.

In the silicon vertex and tracker sensor layers of CLICdet, hits caused by direct and backscattering particles from incoherent pairs and $\gamma\gamma \to$ hadrons add up to significant occupancies, as shown in Figures 14 to 19. The goal at CLIC is to keep occupancies below 3% per bunch train, including safety factors of 5 for incoherent pairs, and 2 for $\gamma\gamma \to$ hadron events[2]. The pixel sizes of the vertex detector and the cell sizes in the tracker disks and barrel layers are chosen so that the occupancies are below this limit, as described for 3 TeV CLIC in [3].

As shown in the figures below, and as expected from the total numbers of background particles given in Table 3, the hit density and rates from beam induced background particles are considerably lower at 380 GeV. The cell sizes in the CLICdet silicon tracker at 3 TeV, given in [3], can therefore safely be used for all CLIC energy stages.

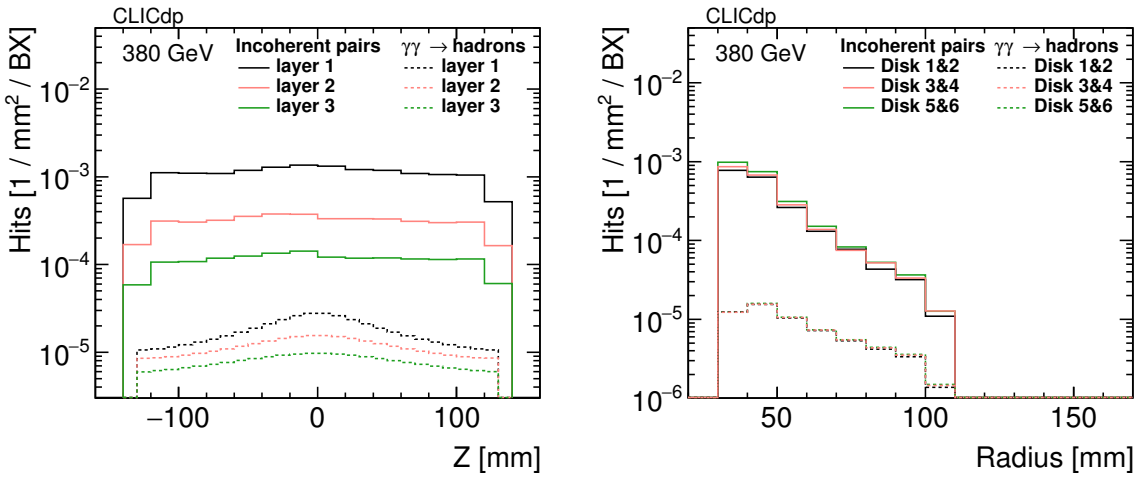

Figure 14: Hit densities per bunch crossing in the vertex barrel (left) and disks (right) from incoherent electron–positron pairs and $\gamma\gamma \to$ hadrons at 380 GeV. Safety factors are not included.

[2] For the definition of occupancy see [3, Equation 2]

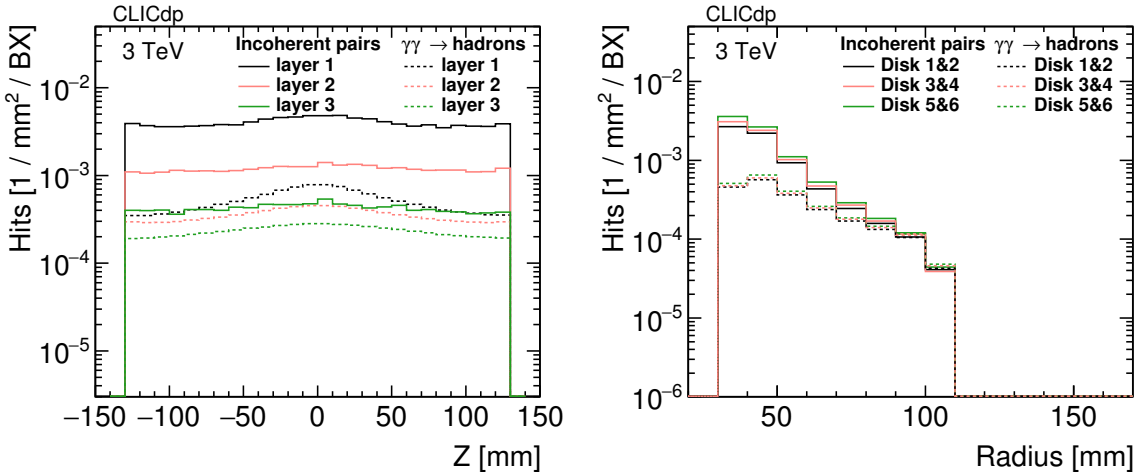

Figure 15: Hit densities per bunch crossing in the vertex barrel (left) and disks (right) detector from incoherent electron–positron pairs and $\gamma\gamma \to$ hadrons at 3 TeV. Safety factors are not included.

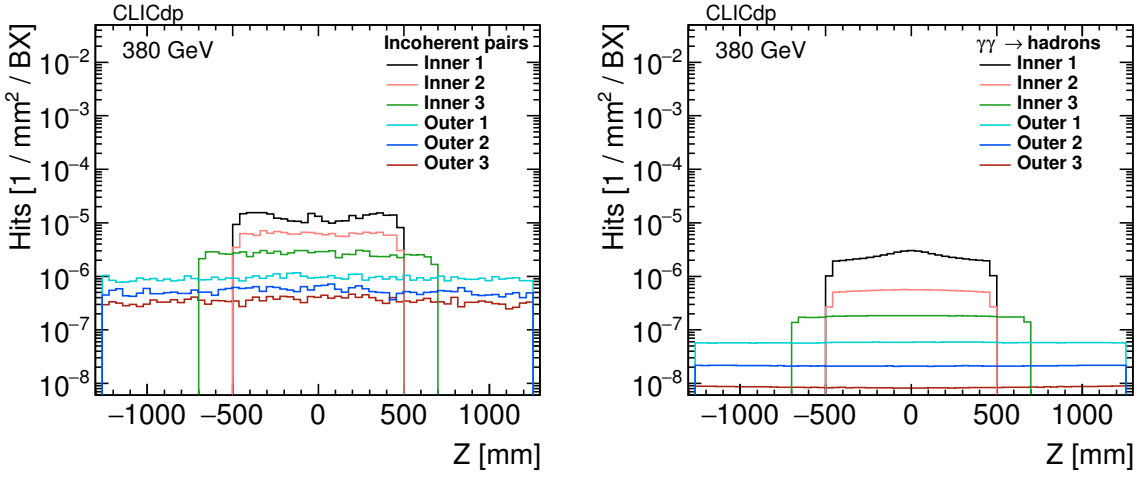

Figure 16: Hit densities per bunch crossing in the tracker barrel layers from incoherent electron–positron pairs (left) and $\gamma\gamma \to$ hadrons (right) at 380 GeV. Safety factors are not included.

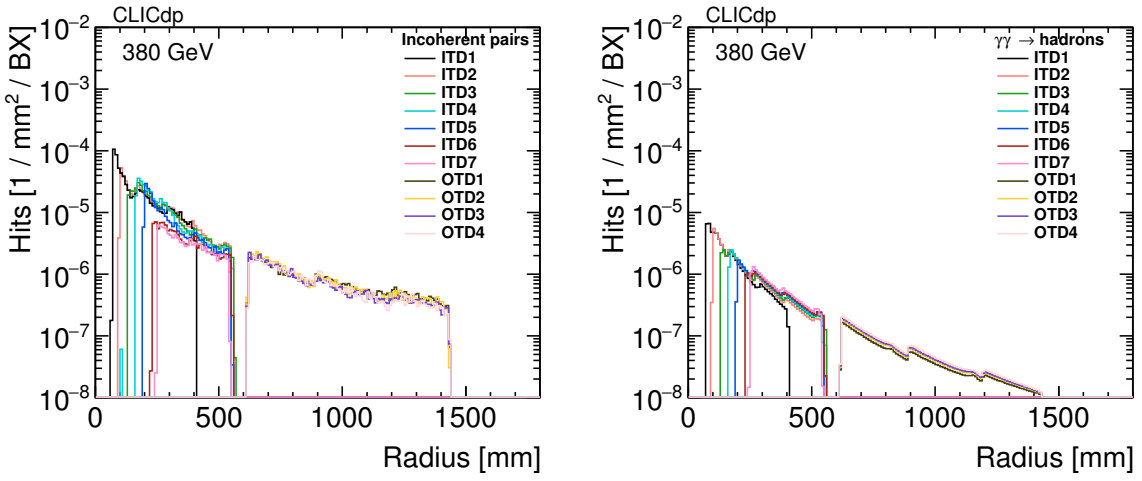

Figure 17: Hit densities per bunch crossing in the tracker disks from incoherent electron–positron pairs (left) and $\gamma\gamma \to$ hadrons (right) at 380 GeV. Safety factors are not included.

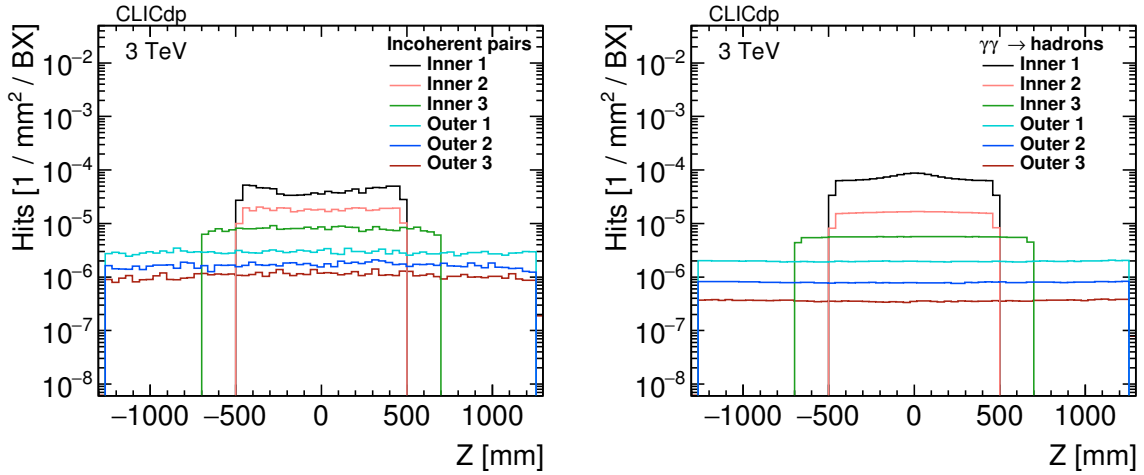

Figure 18: Hit densities per bunch crossing in the tracker barrel layers from incoherent electron–positron pairs (left) and $\gamma\gamma \to$ hadrons (right) at 3 TeV. Safety factors are not included.

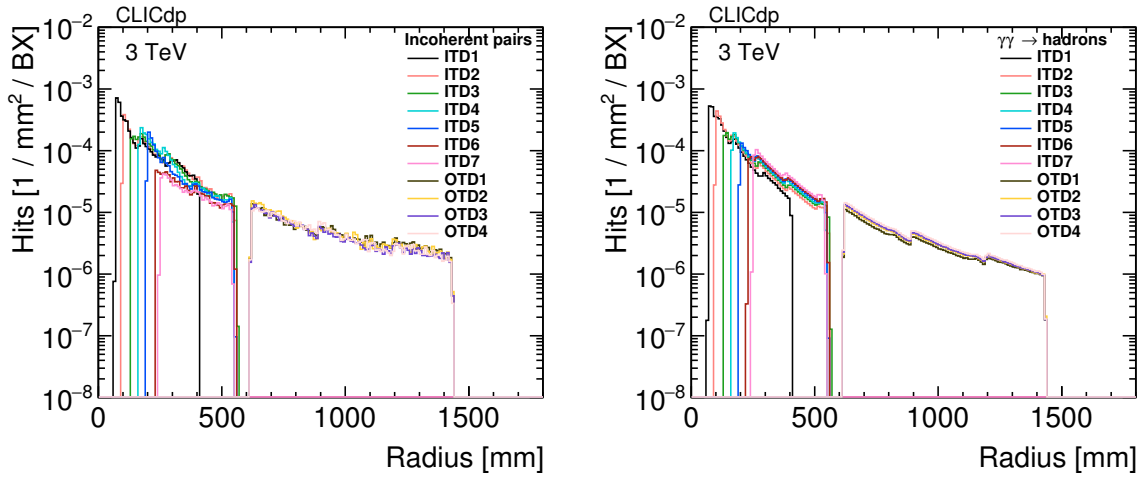

Figure 19: Hit densities per bunch crossing in the tracker disks from incoherent electron–positron pairs (left) and $\gamma\gamma \to$ hadrons (right) at 3 TeV. Safety factors are not included.

Table 5: Energy from beam-induced backgrounds in the CLICdet calorimeters. The numbers correspond to the background for an entire CLIC bunch train and nominal background rates. Safety factors representing the simulation uncertainties are not included.

Energy stage	380 GeV		3 TeV	
Subdetector	Incoherent pairs [TeV]	$\gamma\gamma \to$ hadrons [TeV]	Incoherent pairs [TeV]	$\gamma\gamma \to$ hadrons [TeV]
ECAL barrel	0.13	0.077	0.49	1.9
ECAL endcaps[a]	0.40	0.34	1.4	9.0
HCAL barrel	0.003	0.009	0.011	0.24
HCAL endcaps	154	0.37	632	17
ECAL&HCAL	155	0.80	634	28
LumiCal	5.6	0.37	23	16
BeamCal	6370	0.66	31 500	63

[a] Including the ECAL plugs

3.4.2. Backgrounds in ECAL and HCAL

The distribution of deposited energy from incoherent pairs and $\gamma\gamma \to$ hadrons, including backscattering, has been studied for both the ECAL and the HCAL. The radial calorimetric energy distributions from both types of background in the ECAL endcap are shown in Figure 20 and for the HCAL endcap in Figure 21. The general features found in the CDR [1, Section 2.4.3] are confirmed for CLICdet. The energy deposition and occupancy are found to increase significantly at the lowest radii of the HCAL endcap, now at $R = 250\,\text{mm}$, instead of 400 mm for CLIC_ILD.

Table 5 summarises the simulated background conditions in CLICdet calorimeters for an entire CLIC bunch train. The total calorimetric energy deposition is large compared to the centre-of-mass energy and implies strict requirements on the timing resolution of CLIC calorimeters. Even excluding the HCAL contribution from the incoherent pair background, the overall energy deposited in the CLIC ECAL and HCAL detectors corresponds to more than 28 TeV per bunch train at 3 TeV. This is predominantly forward peaked, but nevertheless poses a serious challenge to the design of a detector at CLIC. The deposited energies without applied calibration factors can be found in Table B.1 in Appendix B.

Another important consideration is the level of occupancy per calorimeter cell. In CLICdet, the ECAL silicon cells are $5 \times 5\,\text{mm}^2$, while the scintillator tiles in the HCAL are $30 \times 30\,\text{mm}^2$. For the occupancy calculation the time window of 200 ns from the start of the bunch train was divided into eight 25 ns time windows. The mean number of hits above the threshold of 0.3 minimum ionising particle equivalents is shown for the ECAL in Figure 22 and for the HCAL in Figure 23.

The occupancies in the ECAL are acceptable, both at 380 GeV and at 3 TeV. In the HCAL endcap at small radii, occupancies exceeding 0.1 per train are observed. This is clearly too high, and studies are on-going to reduce these occupancies which are mainly stemming from neutrons produced by incoherent pair particles in BeamCal, which is located inside the HCAL endcap opening. One possibility could be improved shielding, along the lines of what has been studied previously [9]. Other options include the use of a different active material less sensitive to neutrons, or increasing the transverse segmentation to resolve the occupancy issue.

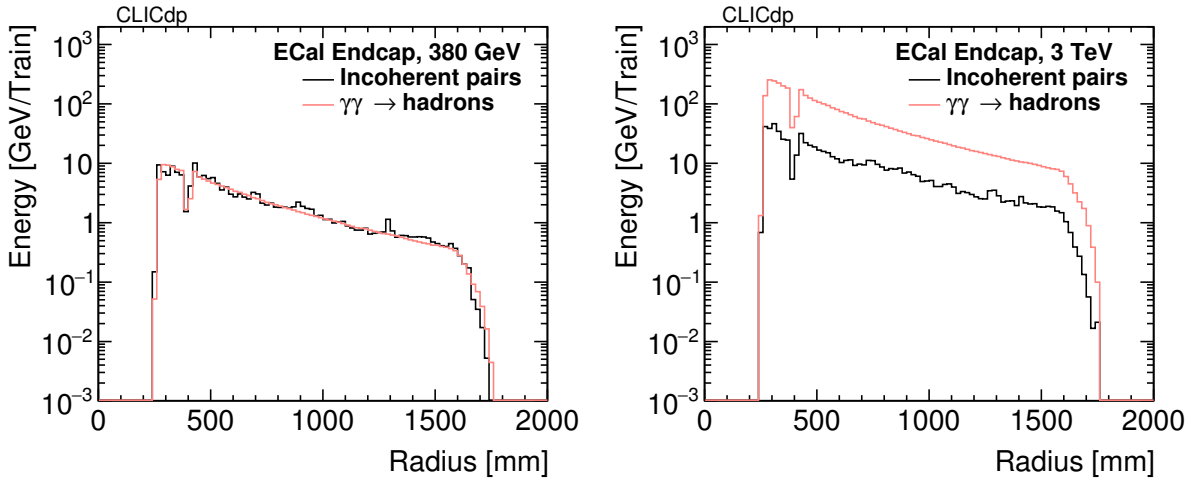

Figure 20: Radial distribution of the calorimetric energy deposition in the ECAL endcap of CLICdet, for 380 GeV (left) and for 3 TeV (right), for an entire bunch train, within 200 ns from the start of the train. Safety factors representing the simulation uncertainties are not included. The bin width is 20 mm. The dip visible around $R = 400$ mm corresponds to the space between ECAL 'plug' and ECAL endcap, which is 30 mm wide.

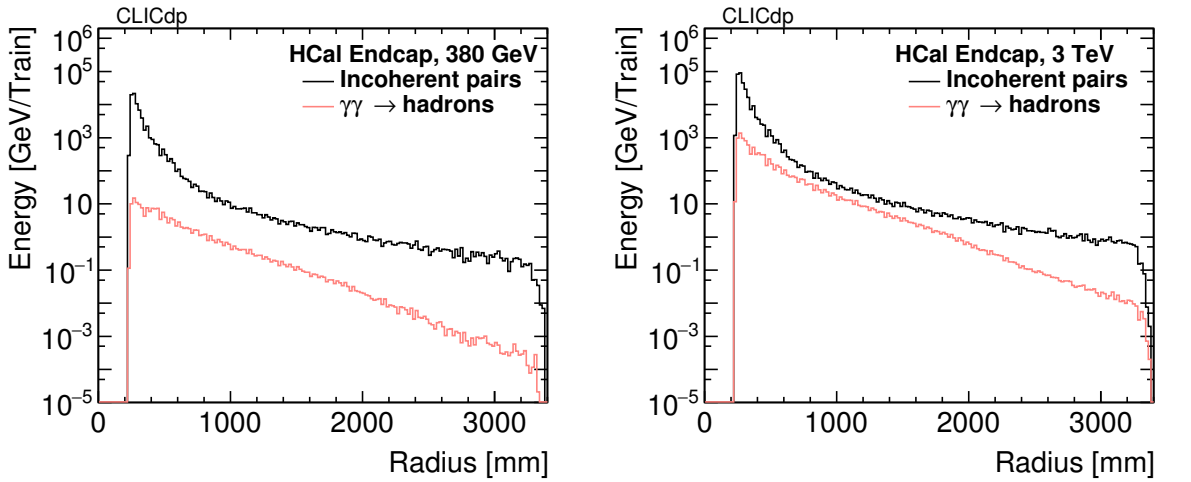

Figure 21: Radial distribution of the calorimetric energy deposition in the HCAL endcap of CLICdet, for 380 GeV (left) and for 3 TeV (right), for an entire bunch train, within 200 ns from the start of the train. Safety factors representing the simulation uncertainties are not included. The bin width is 20 mm.

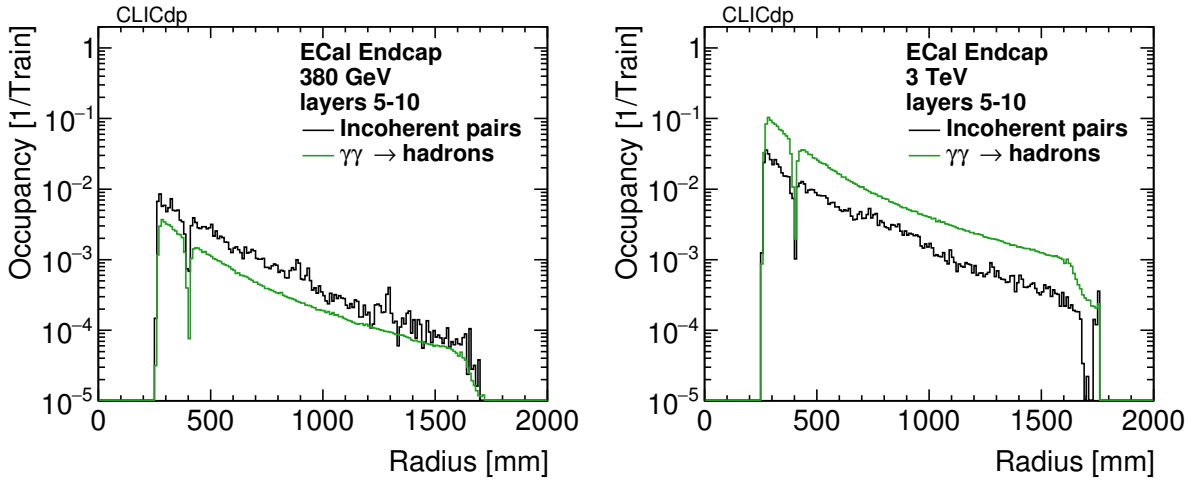

Figure 22: Average cell occupancy in the ECAL endcaps of CLICdet, at 380 GeV (left) and 3 TeV (right). The average is given for layers 5–10 which broadly correspond to maximum energy deposit of typical electromagnetic showers. The results are obtained for nominal background rates, excluding safety factors representing the simulation uncertainties.

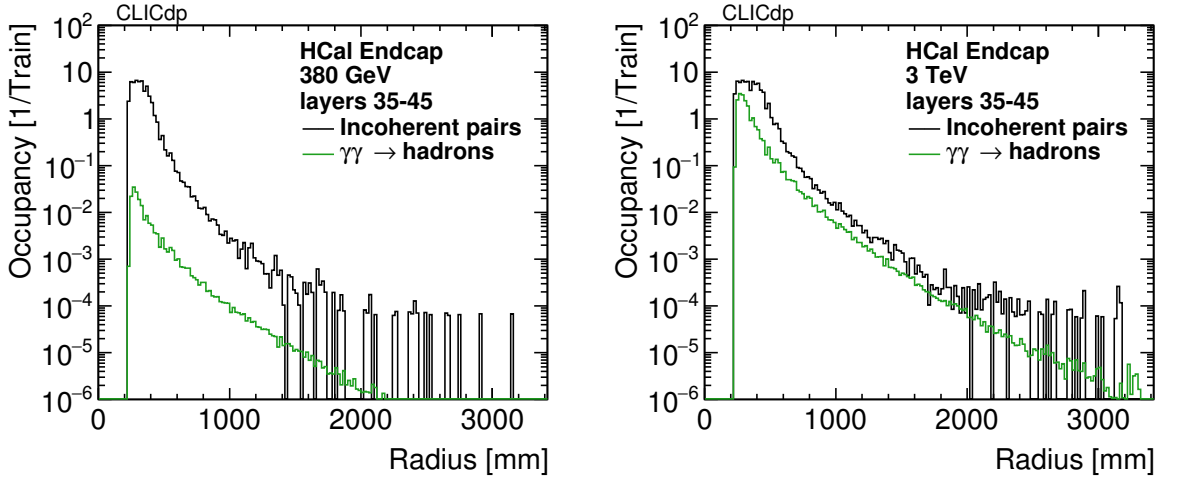

Figure 23: Average cell occupancy in the HCAL endcaps of CLICdet, at 380 GeV (left) and at 3 TeV (right). The average is quoted for layers 35–45 where the maximum activity from the neutron background is observed. The results are obtained for nominal background rates, excluding safety factors representing the simulation uncertainties.

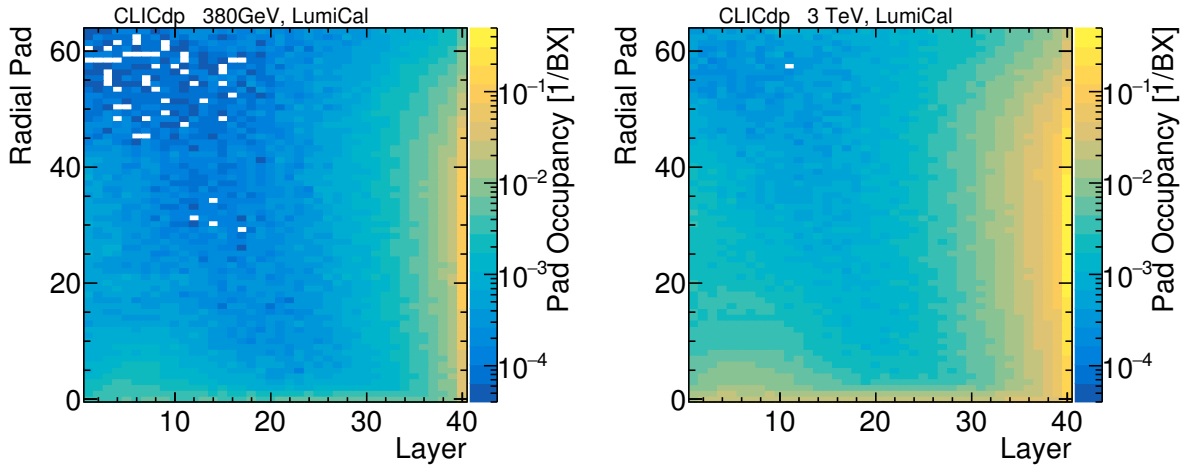

Figure 24: Occupancy per bunch crossing per pad in LumiCal, from incoherent pairs, for 380 GeV (left) and 3 TeV (right) collisions.

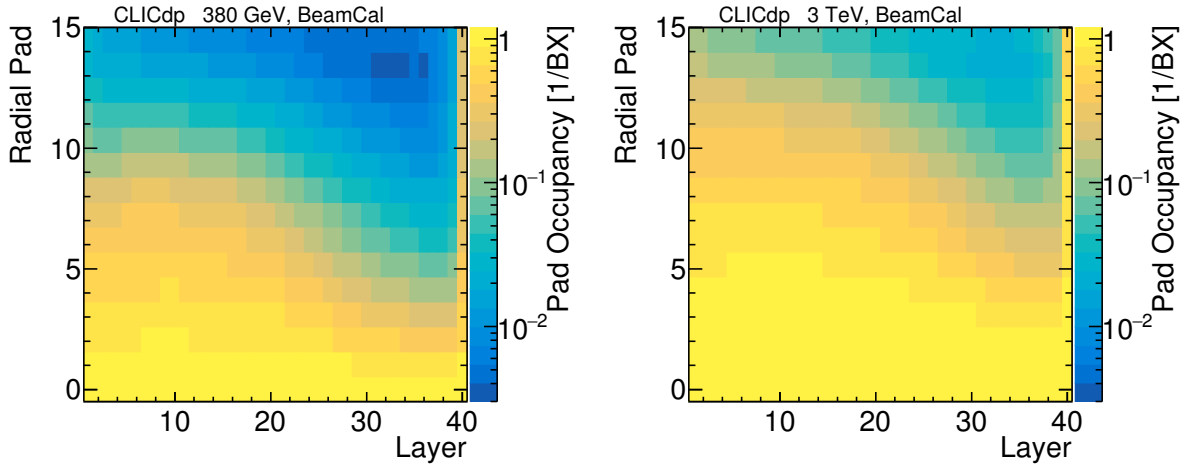

Figure 25: Occupancy per bunch crossing per pad in the BeamCal, from incoherent pairs, for 380 GeV (left) and 3 TeV (right) collisions.

3.4.3. Backgrounds in LumiCal and BeamCal

Due to the angular dependence of the incoherent pairs the very forward calorimeters – the LumiCal and the BeamCal – receive larger background contributions from incoherent pairs than from $\gamma\gamma \to$ hadron events. See Table 5 for the background energies in the forward calorimeters.

Figure 24 shows the occupancies per bunch crossing in the LumiCal from incoherent pairs at 380 GeV and 3 TeV. The occupancies are averaged over all pads with the same radius. The largest occupancy of the LumiCal is in its last layer and is caused by particles scattering back from the BeamCal. Similarly the innermost pads suffer from backscattered particles. In the largest part of the LumiCal the occupancy is below 1%.

The BeamCal occupancies at 380 GeV and 3 TeV are shown in Figure 25. Both at 380 GeV and at 3 TeV, the pads of the BeamCal with the smallest radii with respect to the outgoing beam axis will receive an energy deposit in each bunch crossing. This limits the electron identification efficiency in BeamCal at the smallest polar angles as described in Section 4.2.7.

Table 6: Assumed time windows used for the event reconstruction and the required single hit time resolutions.

Subdetector	Reconstruction window	Hit resolution
ECAL	10 ns	1 ns
HCAL	10 ns	1 ns
Silicon detectors	10 ns	$10/\sqrt{12}$ ns

3.5. Overview of Detector Timing Requirements at CLIC

The timing requirements and the impact of timing cuts at CLIC are described in detail in the CDR [1, Section 2.5]. For CLICdet, these requirements remain unchanged, with one notable difference: since the HCAL absorber material is now steel in both barrel and endcap – instead of tungsten in the barrel and steel in the endcap – the timing requirements are the same for the entire HCAL. The time windows and required single hit time resolutions are summarised in Table 6.

3.6. A Detector at CLIC for 380 GeV, 1.5 TeV and 3 TeV

As illustrated in the previous sections, the CLIC beam conditions and parameters (see Table 3) and the resulting beam-induced background conditions are rather different for the different CLIC energy stages. A priori, this would allow one to consider a somewhat different detector layout for each of the CLIC stages. However, from a practical point of view, it is very likely that the calorimeters, the solenoid, the yoke and muon systems but also the outer tracker will remain unchanged.

On the other hand, the different crossing angle alone imposes a change of the vacuum pipes, which in turn implies replacing the BeamCal when moving from the initial 380 GeV stage to the higher centre-of-mass energies. The diameter of the incoming and outgoing beam pipes must also be adjusted.

In addition, because of the reduced number and lower p_{T} of the incoherent pairs produced at the 380 GeV stage, the radius of the central, cylindrical beryllium beam pipe can be 6 mm smaller [1, Section 12.4.7]. This, in turn, allows one to move the first vertex barrel detector layer to a smaller radius and the positions of the remaining vertex barrel layers can be re-optimised. The need for also adapting the inner tracker layout still remains to be studied.

At the present stage of the CLIC detector and physics studies, it was decided to use CLICdet, i.e. the detector with a layout optimised for the 3 TeV stage, for all energy stages. This is mainly motivated by the need to optimise the use of resources in the studies.

4. Physics Performance

4.1. Simulation and Reconstruction

The detector simulation and reconstruction programs used for the results presented here are developed together with the Linear Collider community. The DD4HEP [10] detector simulation and geometry framework was developed in the AIDA and AIDA2020 projects. Large simulation and reconstruction samples were produced with the ILCDIRAC grid production tool [11, 12]. The software packages of iLCSoft-2018-10-11_gcc62 have been used throughout the study with the CLICdet geometry version CLIC_o3_v14.

4.1.1. Event Generation

The detector performance is studied with single particles or simple event topologies. The individual particles are used to probe the track reconstruction and the particle ID. The reconstruction of particles

inside jets is tested through Z/γ^* events decaying into pairs of u, d, or s quarks at different centre-of-mass energies. These events were created with PYTHIA 6.4 [13]. To study the track reconstruction and particle ID in complex events and for the flavour tagging studies $u\bar{u}$, $d\bar{d}$, $s\bar{s}$, $c\bar{c}$, $b\bar{b}$, and $t\bar{t}$ events were created with WHIZARD 1.9 [14, 15]. The $\gamma\gamma \to$ hadrons event initial states are created in the GUINEAPIG [16] simulation of the CLIC collisions and hadronised in PYTHIA. In all cases, parton showering, hadronisation, and fragmentation is performed in PYTHIA with the fragmentation parameters tuned to the OPAL data taken at LEP [1, Appendix B].

4.1.2. Detector Simulation

The CLICdet detector geometry is described with the DD4HEP software framework, and simulated in GEANT4 [17–19] via the DDG4 [20] package of DD4HEP. The GEANT4 simulations are done with the `FTFP_BERT` physics list of GEANT4 version 10.02p02.

4.1.3. Event Reconstruction

The reconstruction software is implemented in the Linear Collider MARLIN-framework [21]. The reconstruction algorithms take advantage of the geometry information provided via the DDREC [22] data structures and surfaces. The reconstruction starts with the overlay of simulated hits from $\gamma\gamma \to$ hadrons events via the *overlay* processor [23], which selects only the energy deposits inside the timing windows of 10 ns following the physics event (cf. Section 3.5). In the next step, the hit positions in the tracking detectors are smeared with Gaussian distributions according to the expected resolutions described in Section 2.2. For the calorimeter and muon system digitisation, the hit position is taken from the centre of the cell. No smearing of the hit energy is done. The calorimeter hits are scaled with the calibration constants obtained from the reconstruction of mono-energetic 10 GeV photons and 50 GeV K_L^0.

Tracking *ConformalTracking* is the tracking algorithm used for reconstruction at CLICdet [24]. It is composed of a novel pattern recognition strategy followed by a Kalman-filter based fit. A detailed description is given below.

In modern pattern recognition algorithms, the use of cellular networks has been shown to be a powerful tool, providing robustness against missing hits and the addition of noise to the system. For a detector with solenoid field and barrel plus endcap configuration, a cellular automaton (CA) may be applied to provide efficient track finding. Several aspects of CA algorithms may however impact performance negatively: producing many possible hit combinations requires a fit to be performed on a large number of track candidates. This may be costly in processing time. Methods to reduce combinatorics at this stage may, in turn, compromise the final track finding performance. One way around such issues is the additional application of conformal mapping.

Conformal mapping is a geometry transformation which has the effect of mapping circles passing through the origin of a set of axes (in this case the global xy plane) onto straight lines in a new uv co-ordinate system, with u and v defined as follows [25]:

$$u = \frac{x}{x^2+y^2} \qquad v = \frac{y}{x^2+y^2}. \tag{1}$$

By performing such a transform on an xy projection of the detector (where the xy plane is the bending plane of the solenoid), the pattern recognition can be reduced to a straight line search in two dimensions. A cellular automaton can then be applied in this 2D space, with the use of a simple linear fit to differentiate between track candidates. Figure 26 shows an example of the cellular automaton in conformal space.

To make this approach flexible for changes in the geometry and for applications to other detector systems, all hits in conformal space are treated identically, regardless of sub-detector and layer. Cells

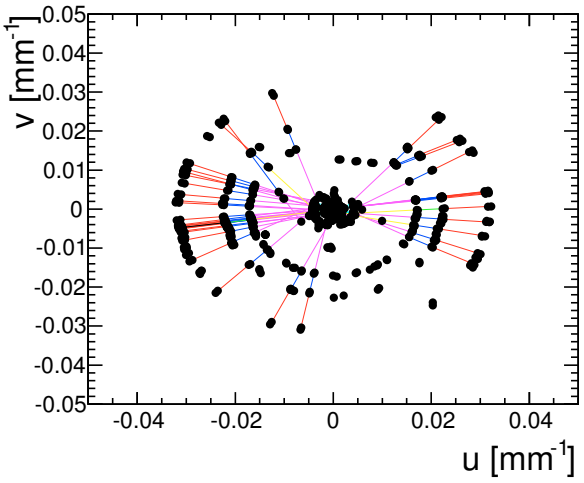

Figure 26: Cellular automaton in conformal space.

between hits are produced within a given spatial search window, employing *kd*-trees [26] for a fast neighbour lookup. This provides additional robustness against missing hits in any given detection layer. A second 2D linear fit in the *sz* parametrisation[3] of the helix is also implemented, to recover the lost information resulting from the 2D projection onto the *xy* plane and reduce the number of *ghost* tracks. A minimum number of 4 hits is required to reconstruct a track.

For displaced tracks, which do not comply with the requirement of passing through the origin of the global *xy* plane, second-order corrections are applied to the transformation equations. Additionally, the search strategy was modified:

- broader angles in the search for nearest neighbours;
- minimum number of 5 hits to reconstruct a displaced track;
- inverted search order, from tracker to vertex hits.

Tracks reconstructed via the pattern recognition are then fitted with a Kalman filter approach. A preliminary helical trajectory is obtained by fitting only three hits (typically the first, last and intermediate hits on the track). The helix parameters are then given as initial input to the Kalman filter, which refits the track while adding hits one by one and progressively updating the track parameters. The default Kalman filter starts from the innermost hits (vertex hits) and proceeds outward. The fit is complemented by a smoothing backward to the IP.

The performance studies presented in this note assume a homogeneous magnetic field of 4 T.

Particle Flow Clustering The calorimeter clusters are reconstructed in the particle flow approach by PandoraPFA [4–6]. PandoraPFA uses the reconstructed tracks and calorimeter hits as input to reconstruct all visible particles. The procedure is optimised to achieve the best jet energy resolution. This may not be the ideal procedure for isolated particles, which can benefit from a dedicated treatment. The output of the particle flow reconstruction are *particle flow objects* (PFOs).

Forward Calorimeter Reconstruction The high energy electrons and photons in the forward calorimeters LumiCal and BeamCal are reconstructed with special considerations for the large amount of incoherent pairs impacting on them [27]. The expected average energy deposits from incoherent pair

[3] *s* is the coordinate along the helix path.

background is subtracted from the total amount of deposited energy before a nearest neighbour clustering is performed on the pads which have sufficient remaining energy. LumiCal and BeamCal performances are described in Section 4.2.7.

4.1.4. Treatment of $\gamma\gamma \to$ hadrons Background

The largest impact on the detector performance from beam-induced backgrounds comes in the form of the $\gamma\gamma \to$ hadron events as discussed in Chapter 3. When studying the detector performance degradation due to these backgrounds the expected number of events n_{Had} (Table 3) are overlaid for 30 bunch crossings around the physics event, which is placed in bunch crossing 11. Accounting for the expected detector timing resolutions and integration times, time windows of 10 ns following the physics event are applied to the hits of the background events and physics event. All hits inside the time window are then passed forward to the reconstruction.

Once the particle flow clustering is finished, additional p_{T} dependent timing cuts are applied. Depending on the particle type – photon, neutral hadron, or charged particle – and the transverse momentum and based on the time of the clusters, reconstructed particles are rejected. The time of a clusters is the truncated energy-weighted mean time of its hits. To allow for different physics topologies three sets of timing cuts were created, *Loose*, *Selected*, and *Tight* timing cuts for the studies at $\sqrt{s} = 3\,\text{TeV}$ and $\sqrt{s} = 1.5\,\text{TeV}$. More relaxed cuts were also created for $\sqrt{s} = 500\,\text{GeV}$ and below. Detailed information on the timing cuts are given in the CDR [1, Appendix B] and in a separate study for the 380 GeV energy stage [28].

4.2. Performance for Lower Level Physics Observables

4.2.1. Single Particle Performances

Impact-Parameter, Angular and Momentum Resolution To identify heavy-flavour quark states and tau-leptons with high efficiency, a precise measurement of the impact parameter point and of the charge of the tracks originating from the secondary vertex is required. Monte Carlo simulations show that these goals can be met with a constant term in the transverse impact-parameter resolution of $a \simeq 5\,\mu\text{m}$ and a multiple-scattering term of $b \simeq 15\,\mu\text{m}$, using the parametrization:

$$\sigma_{d_0}(p,\theta) = \sqrt{a^2 + b^2 \cdot \text{GeV}^2/(p^2 \sin^3(\theta))}. \tag{2}$$

Figure 27(left) shows the transverse impact-parameter resolutions obtained with the baseline configuration for CLICdet (single point resolution in the vertex detector of 3 µm) for isolated muon tracks with momenta of 1 GeV, 10 GeV and 100 GeV, as a function of the polar angle. Each data point corresponds to 10 000 single muons simulated at fixed energy and polar angle. For each dataset, the resolution is calculated as the width of the Gaussian fit of the residual distributions. Residuals are obtained as difference between the reconstructed and simulated parameters per track. Also shown, for reference, are three dashed lines corresponding to Equation (2) for the three energies, with the target values of $a \simeq 5\,\mu\text{m}$ and $b \simeq 15\,\mu\text{m}$. The resolution for 100 GeV muons is well below the high-momentum limit of 5 µm. At 10 GeV, the effect of an increased material becomes visible in the forward region. The same effect impacts the 1 GeV result for all angles. Note that the results for CLICdet at low momenta are slightly worse than those obtained in the CDR [1], due to a more realistic material budget in CLICdet.

The dependence of the d_0 resolution on the pixel size has been studied by varying the single point resolution for the vertex detector layers from the baseline value of 3 µm (which would correspond to a pixel size of 10 µm if no charge-sharing is assumed) to 5 µm and 7 µm (corresponding to pixel sizes of 17 and 24 µm respectively). The resulting resolutions are shown in Figure 27(right). The single point resolution dominates at higher energies, especially in the central region, where a change from 3 µm to 5 µm results in an increase by approximately 50%. However, even in the worst scenario of 7 µm single

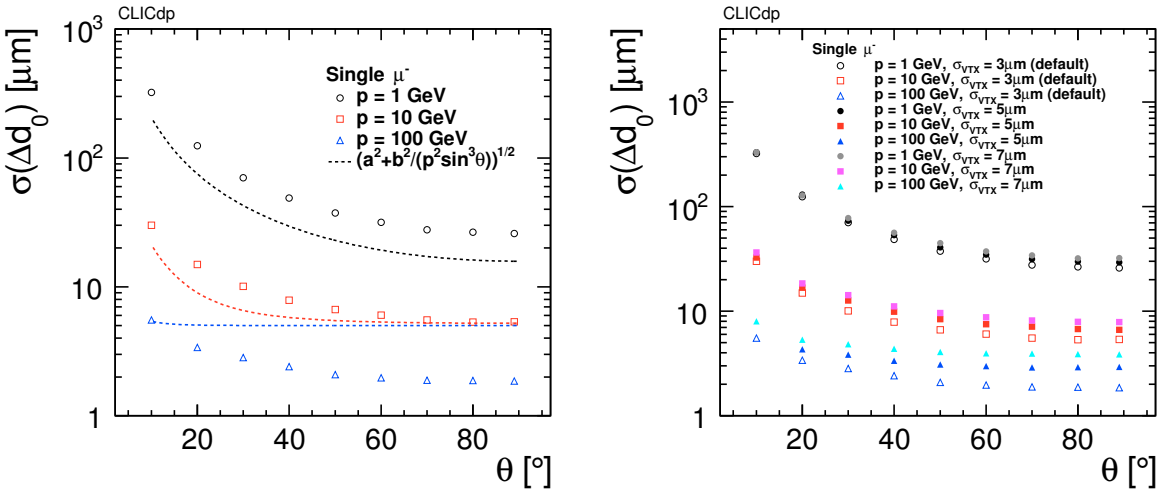

Figure 27: Transverse impact-parameter resolutions as a function of the polar angle for muons with momenta of 1 GeV, 10 GeV and 100 GeV, obtained with the baseline 3 µm single point resolution (left) and different single point resolutions (right) in the vertex detector.

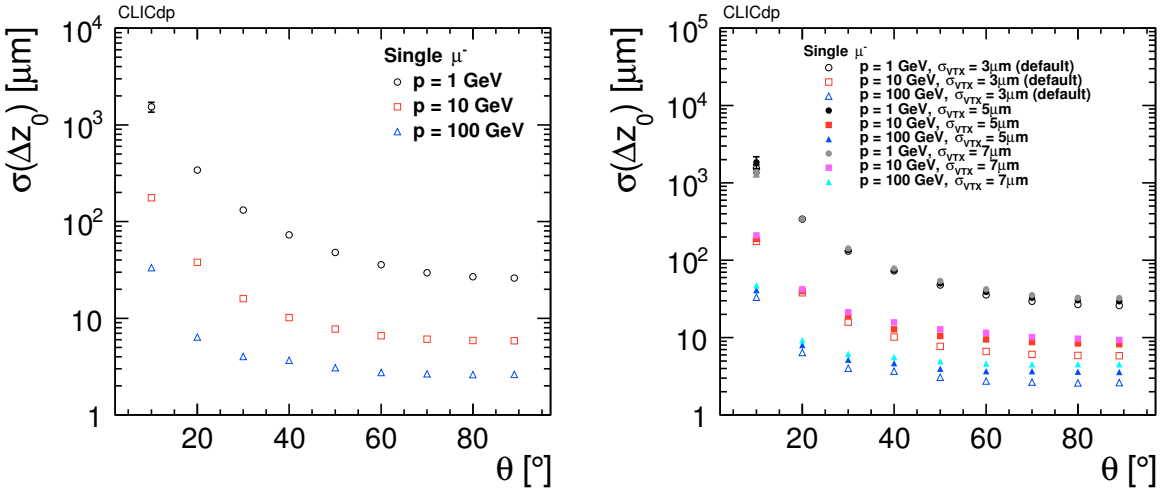

Figure 28: Longitudinal impact-parameter resolutions as a function of the polar angle for muons with momenta of 1 GeV, 10 GeV and 100 GeV, obtained with the baseline 3 µm single point resolution (left) and different single point resolutions (right) in the vertex detector.

point resolution, the d_0 resolution for 100 GeV tracks does not exceed the target value for the high-momentum limit of $a \simeq 5\,\mu\text{m}$. For the 10 GeV tracks, on the other hand, with the d_0 resolution already at the limit for the default 3 µm, any increase in single point resolution is detrimental. For 1 GeV muons, where multiple scattering dominates, the effect of a single point resolution increase from 3 µm to 5 µm amounts to at most 8%.

Similarly, the longitudinal impact-parameter resolution for isolated muon tracks with momenta of 1 GeV, 10 GeV and 100 GeV is shown as a function of the polar angle in Figure 28(left). The achieved resolution for high-energy muons at all polar angles is smaller than the longitudinal bunch length of 44 µm at 3 TeV centre-of-mass energy. A minimum of approximately 1.5 µm is reached for 100 GeV muons at 90°. As for the transverse impact-parameter resolution, the variation of the single point resolution of the vertex detector, shown in Figure 28(right), affects mostly the z_0 resolution of higher-energy muons.

The ϕ dependence of transverse and longitudinal impact-parameter resolutions has been investigated

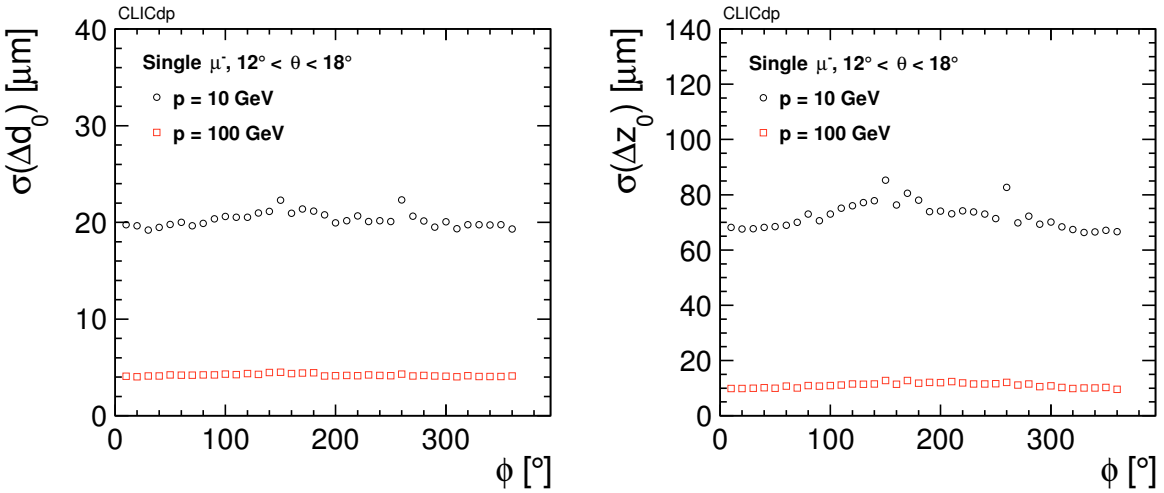

Figure 29: Transverse (left) and longitudinal (right) impact-parameter resolutions as a function of the azimuthal angle in the region $12^\circ < \theta < 18^\circ$ for muons with momenta of 10 GeV and 100 GeV.

in the region $12^\circ < \theta < 18^\circ$ for muons with momenta of 10 GeV and 100 GeV. As shown in Figure 29, the angular dependence is negligible for the highest-energy muons, but it is visible for the lower-energy ones, which, due to multiple scattering and higher curvature, may hit non-equidistant sensors in the different spiral-shaped layers. This results in a non-uniform impact parameter resolution. The variation for the 10 GeV muons, however, amounts to at most 15% for both d_0 and z_0, thus validating the robustness of the spiral geometry of the vertex disks.

Figure 30 shows the polar angle resolution (left) and the azimuthal angle resolution (right), both as a function of the polar angle θ, for isolated muon tracks with momenta of 1 GeV, 10 GeV and 100 GeV. The polar angle resolution follows different trends according to the muon energy. For 1 GeV muons, it decreases slightly while going from the forward to the transition region and levels up in the central region. For 10 GeV muons, the dependence on polar angle is negligible. On the contrary, a visible dependence is observed for 100 GeV muons: smaller resolutions are obtained in the transition regions, where a higher number of measurements (traversed layers) is available, while resolutions in the barrel are limited by single point resolution. The azimuthal angle resolution follows a similar trend for different muon energies, decreasing monotonically while going from the forward to the central region. For high-energy muons, it reaches a minimum of 0.025 mrad in the barrel. The same value is obtained for the polar angle resolution in the transition region.

The p_T resolution $\sigma(\Delta p_\mathrm{T}/p_\mathrm{T}^2)$ for single muons is determined from a single Gaussian fit of the distribution $(p_\mathrm{T,MC} - p_\mathrm{T,rec})/p_\mathrm{T,MC}^2$ and is shown in Figure 31 as a function of the polar angle θ and of the momentum. Each data point corresponds to 10 000 muons simulated at a fixed energy and polar angle. In the barrel region, the p_T resolution reaches $3 \cdot 10^{-5}\,\mathrm{GeV}^{-1}$ for muons with a momentum of 100 GeV. The dashed lines correspond to the fit of the data points according to the parametrization:

$$\sigma(\Delta p_\mathrm{T}/p_\mathrm{T}^2) = a \oplus \frac{b}{p \sin^{3/2}\theta} \tag{3}$$

where parameter a represents the contribution from the curvature measurement and parameter b is the multiple-scattering contribution. The values of these parameters for the different fitted curves are summarised in Table 7. Requirements on the momentum resolution follow from dedicated studies of BSM scenarios. As an example, the determination of the smuon and neutralino masses from the muon momentum distribution in the process $\mathrm{e^+e^-} \to \tilde{\mu}^+\tilde{\mu}^- \to \mu^+\mu^-\tilde{\chi}_1^0\tilde{\chi}_1^0$ requires a momentum resolution of $2 \cdot 10^{-5}\,\mathrm{GeV}^{-1}$ in order for the high momentum part of the spectrum not to be distorted [1, Section 2.2.1]. This is achieved for central tracks with momenta larger than 500 GeV. For low momentum

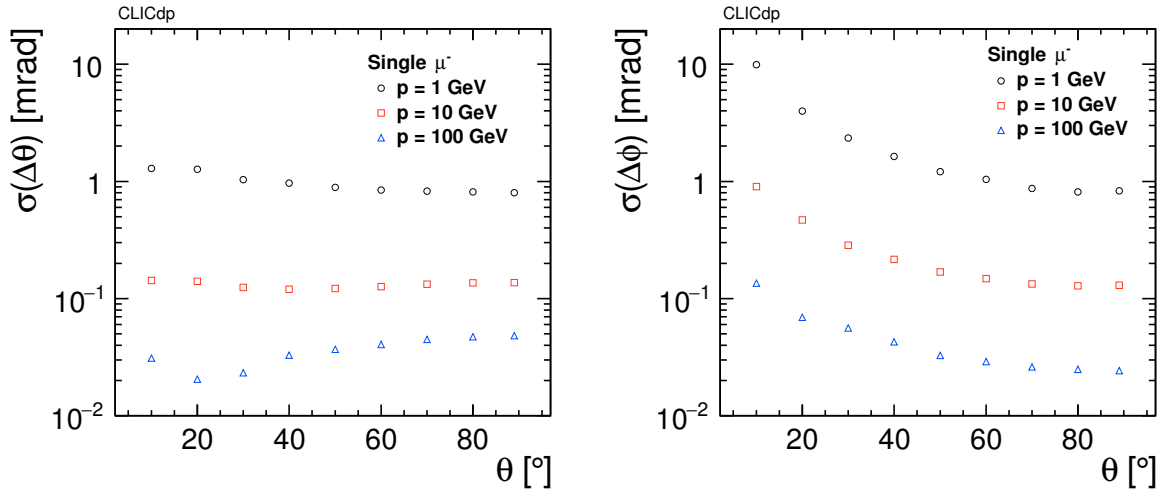

Figure 30: Polar angle (left) and azimuthal angle (right) resolutions as a function of the polar angle for muons with momenta of 1 GeV, 10 GeV and 100 GeV.

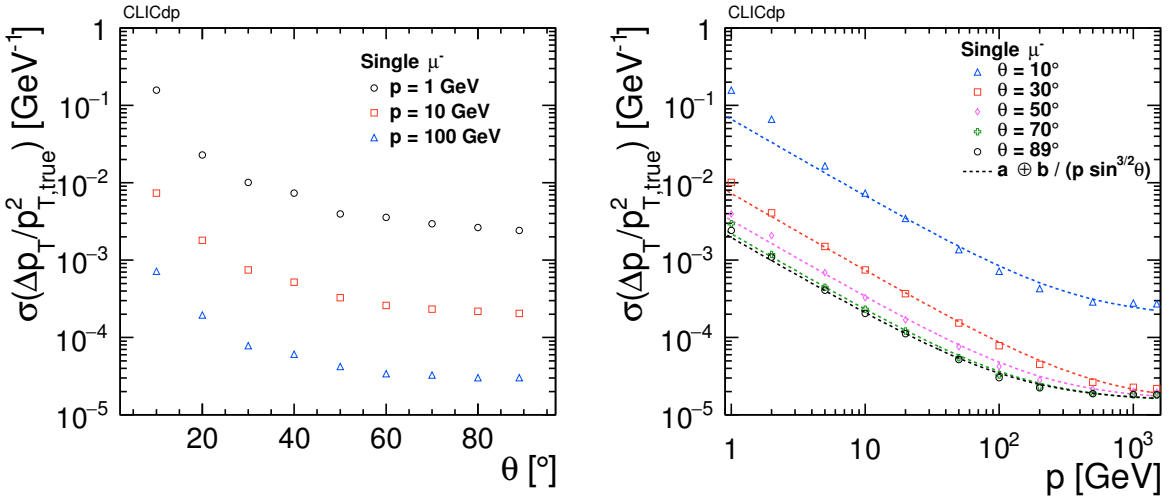

Figure 31: Transverse momentum resolution as a function of the polar angle for muons with momenta of 1 GeV, 10 GeV and 100 GeV (left) and as a function of the momentum for muons at polar angles $\theta = 10^\circ, 30^\circ, 50^\circ, 70^\circ, 89^\circ$ (right). The lines represent the fit of each curve with the parametrization $a \oplus b/(p \cdot \sin^{3/2}\theta)$.

tracks, the values deviate from the parametrization due to the larger amount of material traversed.

Similarly, the momentum resolution for isolated electron and pion tracks was studied and is shown in Figure 32. Performances are comparable with those for isolated muon tracks.

Tracking Efficiency Tracking efficiency is defined as the fraction of reconstructable Monte Carlo particles that have been reconstructed. A particle is considered reconstructable if it is stable at generator level (genStatus = 1), if $p_T > 100\,\text{MeV}$, $|\cos\theta| < 0.99$ and if it has at least 4 unique hits (i.e. hits which do not occur on the same subdetector layer). The efficiency for isolated muon tracks has been computed by reconstructing 2 million muons simulated at polar angles $\theta = 10^\circ, 30^\circ, 89^\circ$ and with a descending power-law energy distribution defined between 100 MeV and 500 GeV. It is shown in Figure 33 as a function of p_T. The tracking efficiency is constant at 100% for all polar angles, with a maximum drop of roughly 1% for $p_T < 200\,\text{MeV}$. Figure 34 shows the muon efficiency as a function of the polar

Table 7: Parameter values from the fit of Equation (3) for Figure 31(right)

Angle	Parameter a [GeV^{-1}]	Parameter b
10°	$1.8 \cdot 10^{-4}$	0.0048
30°	$1.4 \cdot 10^{-5}$	0.0026
50°	$1.5 \cdot 10^{-5}$	0.0022
70°	$1.5 \cdot 10^{-5}$	0.0020
89°	$1.5 \cdot 10^{-5}$	0.0019

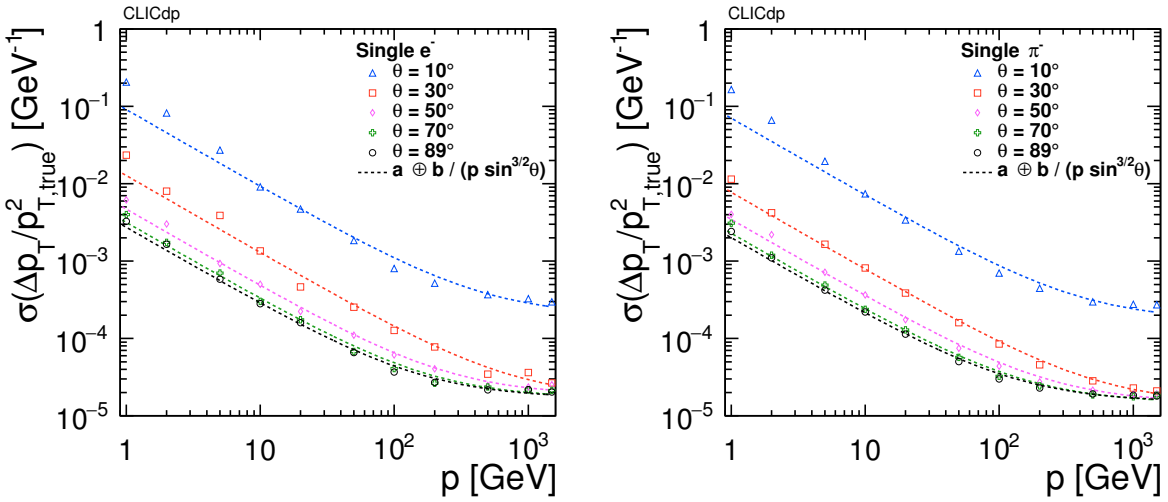

Figure 32: Transverse momentum resolution as a function of the momentum for electrons (left) and pions (right) at polar angles θ =10°, 30°, 50°, 70°, 89°. The lines represent the fit of each curve with the parametrization $a \oplus b/(p \cdot \sin^{3/2}\theta)$.

angle (left) and the azimuthal angle (right). For all energies, fully efficient performances are obtained at any ϕ and θ, except in the region $10^\circ < \theta < 20^\circ$, where the geometrical layout of the tracking system (see Figure A.2 in Appendix A) contributes to an efficiency loss of at most 1% at 10° and 15°. It has been demonstrated that this efficiency loss is fully recovered when performing the Kalman filter fit in the inverted direction by starting from the outermost hits. A study aimed at upgrading the fitting procedure is currently ongoing.

Similarly, 100 000 isolated electrons and pions simulated at polar angles $\theta = 10^\circ, 30^\circ, 89^\circ$ and with a descending power-law energy distribution defined between 100 MeV and 500 GeV have been simulated and reconstructed. The tracking efficiency is shown in Figure 35 as a function of the transverse momentum. For both particle species, the reconstruction of central tracks is fully efficient, while for lower-energy electrons and pions the efficiency loss appears at higher p_T than for muons, and it amounts to a maximum of 2% within statistical uncertainties.

To probe the tracking performances for displaced tracks, 10 000 single muons have been simulated, requiring their production vertex to be within 0 cm $< y <$ 60 cm and their angular distribution in a cone of 10° width around the y axis, i.e. $80^\circ < \theta, \phi < 100^\circ$. This is done for simplicity, such that particles are produced in the barrel and they traverse roughly the same amount of material. The efficiency as a function of the production vertex radius $R = \sqrt{x^2 + y^2}$, is shown in Figure 36 for muons with momenta of 1 GeV, 10 GeV and 100 GeV. For 1 GeV muons that are produced with $R \geq 60$ mm outside the vertex detector the efficiency drops by 20%, due to the fact that by losing energy while traversing the detector

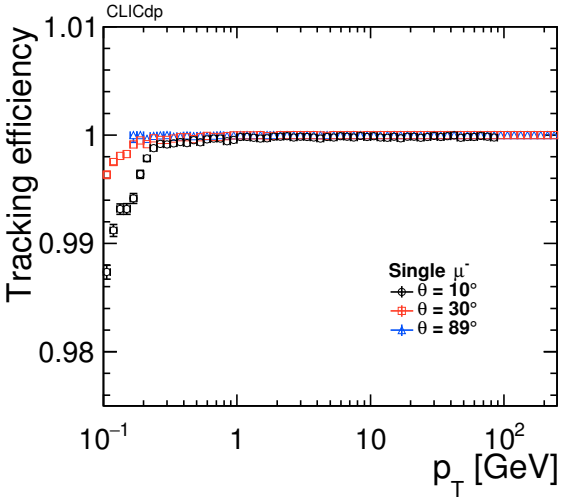

Figure 33: Tracking efficiency as a function of p_{T} for muons at polar angles θ =10°, 30°, 89°.

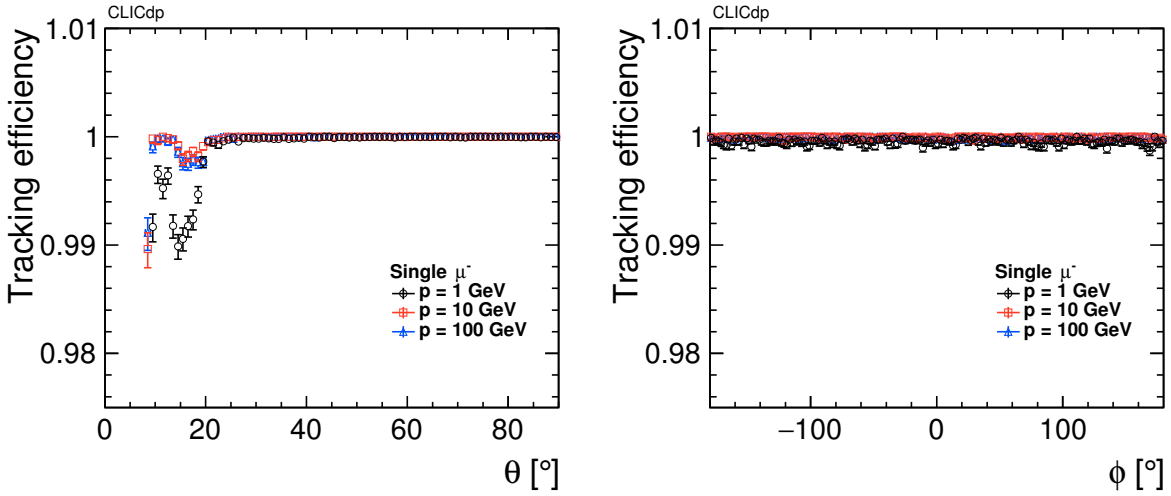

Figure 34: Tracking efficiency as a function of the polar (left) and the azimuthal (right) angle for muons with momenta of 1 GeV, 10 GeV and 100 GeV.

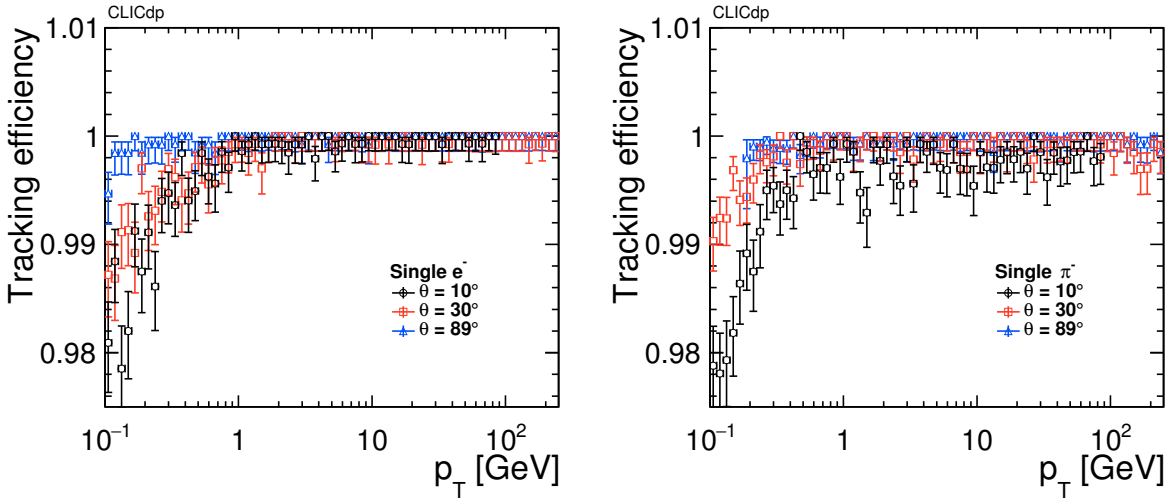

Figure 35: Tracking efficiency as a function of p_{T} for electrons (left) and pions (right) at polar angles $\theta = 10^{\circ}, 30^{\circ}, 89^{\circ}$.

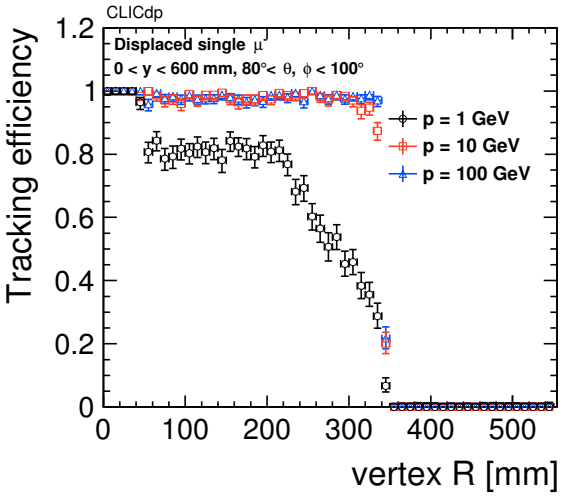

Figure 36: Tracking efficiency as a function of the production vertex radius for muons with momenta of 1 GeV, 10 GeV and 100 GeV, uniformly generated in a range $0 < y < 600$ mm and $80^\circ < \theta, \phi < 100^\circ$.

layers, those particles have not enough left-over momentum to reach the required minimum number of hits. For higher-energy muons, instead, the efficiency is above 95% at any radius. Regardless of the energy, an abrupt fall-off is observed for all tracks with a production radius of 350 mm or more. This is an effect of the reconstruction cuts, since for displaced tracks a minimum number of 5 hits is required to reconstruct the track, while only 4 sensitive layers are traversed by tracks starting beyond $R = 350$ mm.

Particle Reconstruction and Identification Particles are reconstructed and identified using the PandoraPFA C++ Software Development Kit [4]. These particle flow reconstruction algorithms have been studied extensively in full GEANT4 simulations of the CLIC_ILD detector concept [6]. Particle flow aims to reconstruct each visible particle in the event using information from all subdetectors. The high granularity of calorimeters is essential in achieving the desired precision measurements. Electrons are identified using clusters largely contained within ECAL and matched with a track. Muons are determined from a track and a matched cluster compatible with a minimum ionising particle signature in ECAL and HCAL, plus corresponding hits in the muon system. A hadronic cluster in ECAL and HCAL matched to a track is used in reconstructing charged hadrons. Hadronic clusters without a corresponding track give rise to neutrons, and photons are reconstructed from an electromagnetic cluster in ECAL. In jets typically 60% of the energy originates from charged hadrons and 30% from photons. The remaining 10% of the jet energy are mainly carried by neutral hadrons.

The performance of the Pandora reconstruction algorithms is studied in single particle events at several energies, generated as flat distributions in $\cos\theta$. The ECAL energy resolution is studied using single photon events. At each energy point in three different regions (barrel, endcap, and transition region) the photon energy response distribution is fitted with a Gaussian. The σ of the Gaussian is a measure for the energy resolution in ECAL. At very large photon energies the photon energy resolution is affected by energy leakage into HCAL. The energy dependence of the photon energy resolution of CLICdet is shown in Figure 37(left), for the three detector regions. The stochastic term is $15\%/\sqrt{E}$, determined from a two parameter fit within the energy range between 5 GeV and 200 GeV.

For hadrons, the HCAL hits are reweighted using the software compensation technique implemented within PandoraPFA, and developed by the CALICE (Calorimeter for Linear Collider Experiment) collaboration [29, 30]. In the non-compensating calorimeters of CLICdet the detector response for electromagnetic subshowers is typically larger than for hadronic showers. On average the electromagnetic

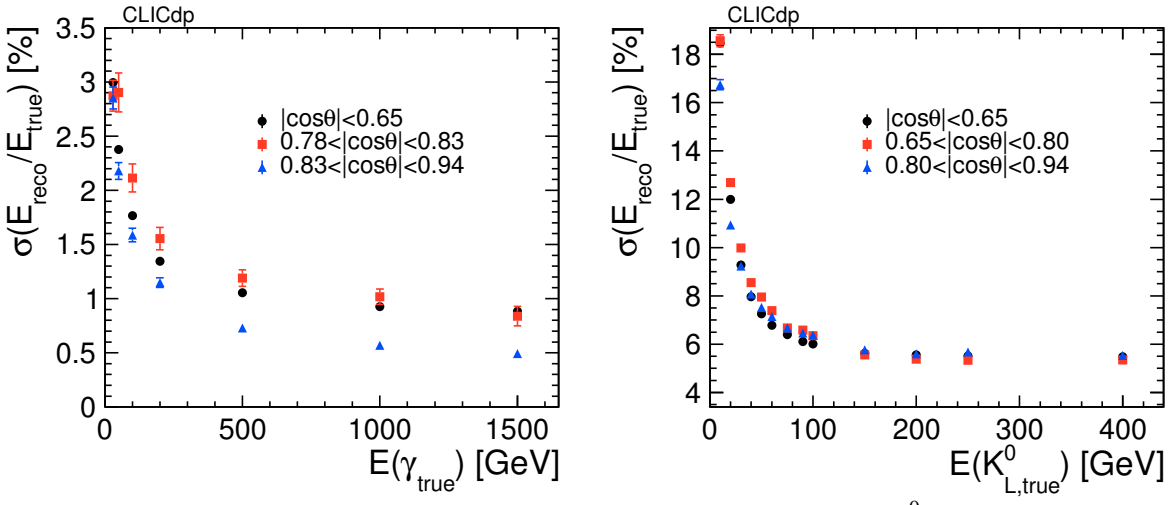

Figure 37: Photon energy resolution (left) and neutral hadron resolutions of K_L^0's (right) as a function of the energy. Results are shown for the barrel region, transition region and endcap.

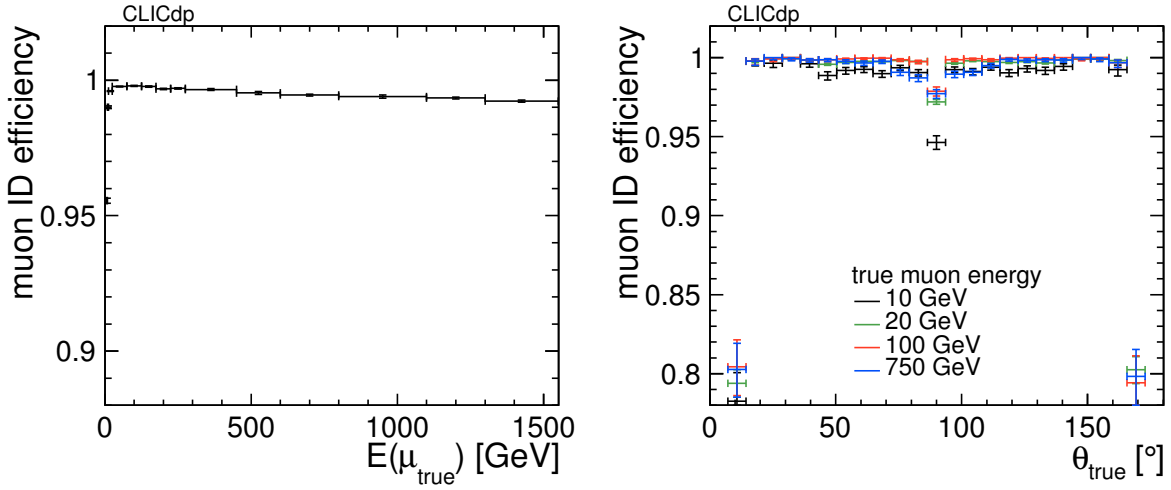

Figure 38: Particle identification efficiency for muons as a function of the energy (left) and as a function of the polar angle θ for four different energies (right).

component of the shower has larger hit energy densities. The weights depend on the hit energy density and the unweighted energy of the calorimeter cluster, where hits with larger hit energy densities receive smaller weights. In a dedicated calibration procedure within PandoraPFA, software compensation weights are determined using single neutron and K_L^0 events over a wide range of energy points. At each energy point equal statistics is required, i.e. using the same number of events for neutrons and K_L^0. Only events with one cluster fully contained within ECAL plus HCAL are used in this calibration. Software compensation improves the energy resolution of hadronic clusters. The resulting energy resolution of neutral hadrons is shown for K_L^0 as a function of the energy in Figure 37(right).

The particle identification efficiency of Pandora particle flow algorithms is studied in single particle events separately for muons, electrons, photons and pions. The events are produced as flat distributions in $\cos\theta$. The reconstructed particle is required to be of the same type as the generated particle, and spatially matched within 1° around it. The identification efficiency is studied as a function of the energy and polar angle θ. To avoid any bias from lower efficiencies in the forward tracking, the energy dependence is studied for events where the true particle direction is restricted to $|\cos\theta| < 0.95$. Identification for muons

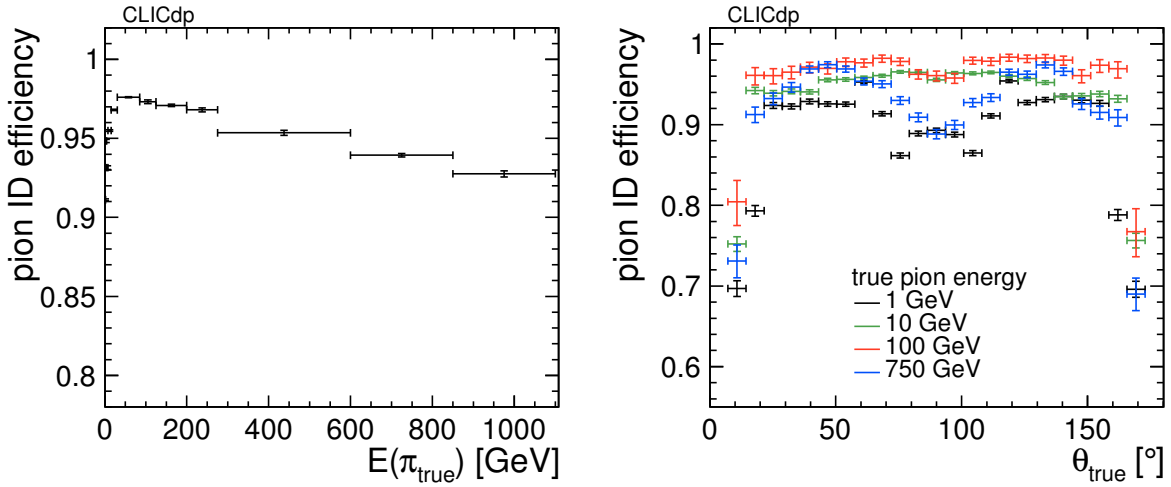

Figure 39: Particle identification efficiency for pions as a function of the energy (left) and as a function of the polar angle θ for four different energies (right).

are illustrated in Figure 38(left) as a function of the energy and in Figure 38(right) as a function of the polar angle θ. The efficiency reaches a plateau beyond 99% from energies of 10 GeV up to 1.5 TeV, flat as a function of the polar angle. The drop at 90° appears to be an artifact of the reconstruction, which is currently being fixed. The efficiency of pion identification is beyond 90% already from 1 GeV on, about 98% at 100 GeV, but drops below 95% at very high energies (Figure 39(left)), particularly due to inefficiencies around polar angles of 90° (Figure 39(right)). The electron identification efficiency as a function of the energy is shown in Figure 40(left). At 10 GeV, the efficiency is around 85% in the barrel and around 80% in the endcaps, as can be seen in Figure 40(right). For energies of about 30 GeV and higher, the efficiencies reach 90% both in the endcap and barrel. The lack of electron identification efficiency at low energies can be attributed to incomplete recovery of Bremsstrahlung photon energy. In the transition region between barrel and endcaps the efficiency is 5%–10% lower than in the endcaps.

While for muons and pions the reconstructed energy is typically well within 10% of the true energy, for electrons the reconstructed energy has, due to Bremsstrahlung, a long tail towards lower values compared to the true energy. Work is ongoing to develop a Bremsstrahlung recovery algorithm, using close by photons to dress the electron momentum by summing their four momenta. This procedure shows a good performance for electron energies below 250 GeV. The energy response is recovered and the width of the energy response is within 10%. However, at higher electron energies sizeable tails are introduced. Thus at large electron energies the recovery algorithm needs to be improved.

For single photons, the signatures for unconverted and converted photons are considered separately. The fraction of converted photons is around 11% overall, for all energy points. This fraction increases from around 7% at 90° to around 20% for very forward polar angles. The particle identification efficiency for unconverted and converted photons is shown in Figure 41. For unconverted photons the identification efficiency is beyond 99% for all energies if only angular matching is required. An additional requirement on the reconstructed energy (must be within 5 σ_E, based on the two parameter fit on the resolution curves shown in Figure 37(left)) leads to a slight reduction of the efficiency, in particular at the highest photon energies, as shown in Figure 41(left): At such high photon energies, leakage into HCAL leads to larger tails in the photon energy response distribution.

In addition the photon cluster might be split into two clusters. In a separate study it has been found that merging of these two clusters increases the angular and energy matched ID efficiency from 95% to 97% for 1.5 TeV photons.

For converted photons, requiring only angular matching results in a high efficiency at high energies, but is only about 75% at 50 GeV. Adding the energy matching criterion to the leading photon in the

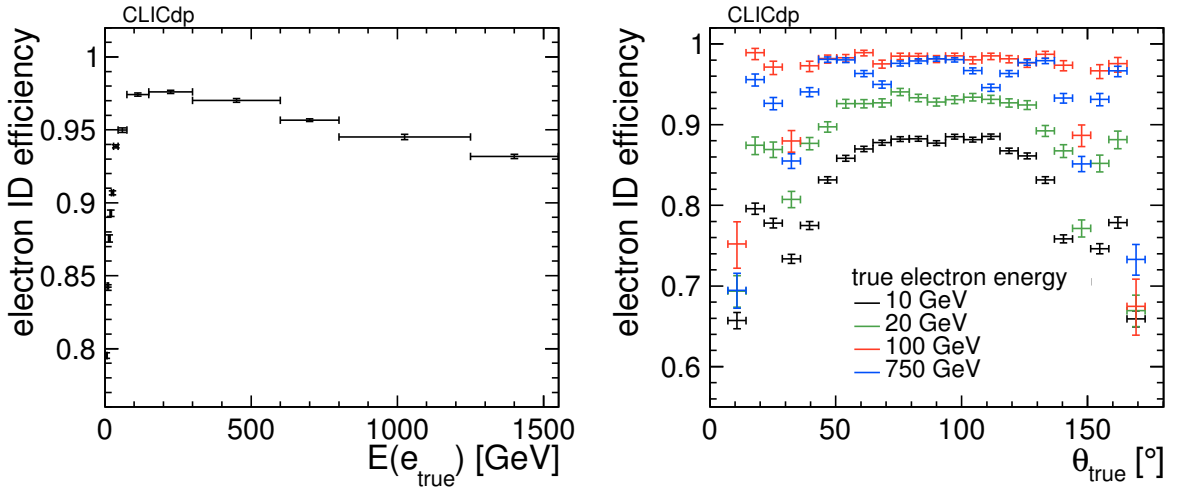

Figure 40: Particle identification efficiency for electrons as a function of the energy (left) and as a function of the polar angle θ for four different energies (right).

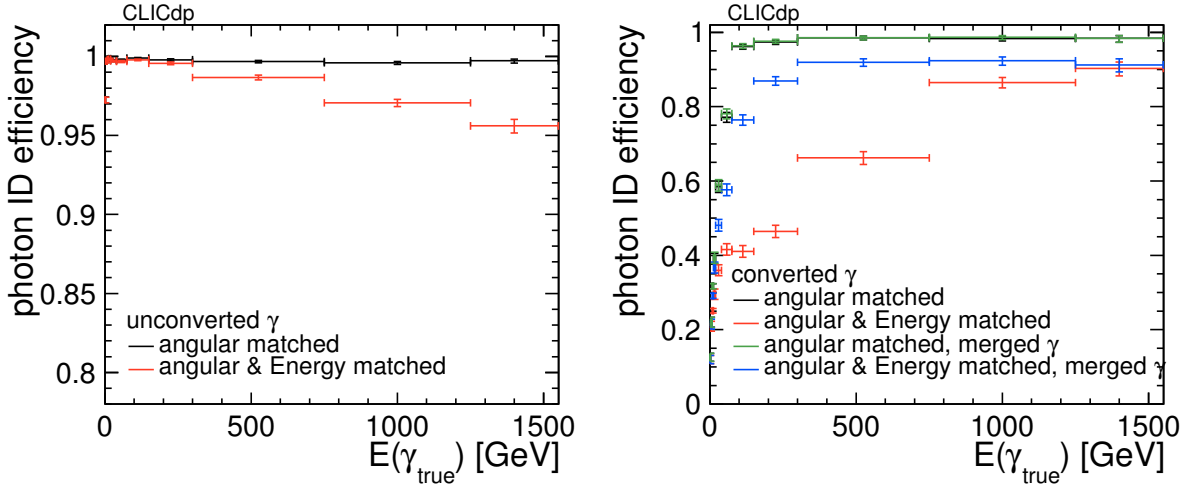

Figure 41: Particle identification efficiency for unconverted (left) and converted photons (right) as a function of the energy. In the case of unconverted photons, the efficiency is shown when requiring either angular, or angular and energy, matching. In the case of converted photons both criteria are, additionally, applied after merging leading photon candidates (i.e. their electromagnetic clusters) into one new photon candidate.

event leads to a strongly reduced efficiency, as expected (see the red curve in Figure 41(right)). For high energies both electrons from the converted photon are so collimated that a single cluster is reconstructed, thus efficiencies beyond 80% are reached even when requiring energy matching. In many conversion events PandoraPFA reconstructs two photons in its default configuration. Merging both reconstructed candidate clusters, if they are within a distance of 2°, and applying the identification criteria on the merged candidate, significantly improves the efficiency for the angular and energy matched case (see the blue curve in Figure 41(right)).

Around 60% of all conversions occur before reaching the last 4 layers of the tracker. The tracking algorithm requires at least four hits in the tracker. Work has started on a CLIC specific conversion algorithm in Pandora which should improve identification of converted photons particularly at low energies.

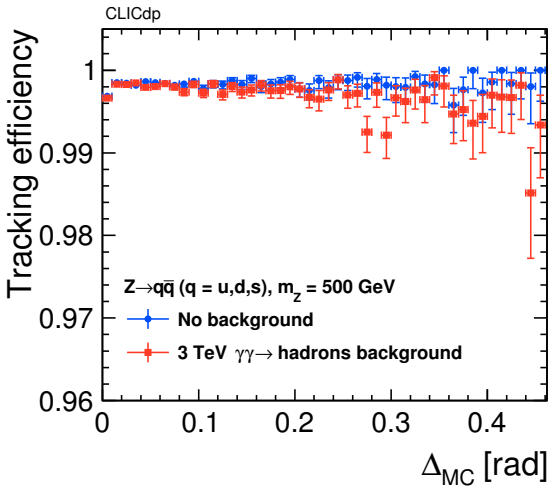

Figure 42: Tracking efficiency as a function of the particle proximity Δ_{MC} for 500 GeV light flavour $Z/\gamma^* \to q\bar{q}$ events, with and without 3 TeV $\gamma\gamma \to$ hadron background overlay.

4.2.2. Performances for Complex Events

Tracking Efficiency The tracking performances for particles in jets have been studied in samples of different energy and event type. In the following, results will be presented for 10 000 $t\bar{t}$ and $b\bar{b}$ events at 3 TeV centre-of-mass energy and for 10 000 light flavour $Z/\gamma^* \to q\bar{q}$ events of 380 GeV and 500 GeV centre-of-mass energy.

Tracking efficiency is defined as the fraction of reconstructable[4] Monte Carlo particles which have been reconstructed as *pure* tracks. A track is considered pure if at least 75% of its hits belong to the same Monte Carlo particle. The fraction of reconstructed tracks that are not pure defines the fake rate.

In jet events, the vicinity of other particles may affect the performance of the pattern recognition in assigning the right hits to the proper track. Therefore, the tracking efficiency in Z/γ^* events decaying to light quarks at 500 GeV has been monitored as a function of the particle proximity Δ_{MC}. This is defined as the smallest distance between the Monte Carlo particle associated to the track and any other Monte Carlo particle, $\Delta_{MC} = \sqrt{(\Delta\eta)^2 + (\Delta\phi)^2}$, where η is the pseudorapidity. The efficiency is shown in Figure 42, in which the following cuts are applied: $10^\circ < \theta < 170^\circ$, $p_T > 1$ GeV and production radius smaller than 50 mm.

The efficiency has been estimated for events with and without overlay of 30 BX of $\gamma\gamma \to$ hadron background for the 3 TeV CLIC machine, with negligible differences observed between the two cases. A cut on the particle proximity of $\Delta_{MC} > 0.02$ rad has been applied in all following tracking efficiency results.

Figure 43(left) shows the tracking efficiency in 500 GeV light flavour $Z/\gamma^* \to q\bar{q}$ events, with and without overlay of 30 BX of $\gamma\gamma \to$ hadron background for the 3 TeV CLIC machine, as a function of the transverse momentum. The following cuts are applied for each particle in this plot: $10^\circ < \theta < 170^\circ$, $\Delta_{MC} > 0.02$ rad, and a production radius smaller than 50 mm. The effect of the $\gamma\gamma \to$ hadron background is visible mostly in the low-p_T region, since background particles have mostly $p_T < 5$ GeV, where it results at most in a 10% efficiency loss at 100 MeV with respect to the case without background. In the region at intermediate and high p_T, the impact from background is negligible, and the efficiency reaches 100%. For comparison, 30 BX of $\gamma\gamma \to$ hadron background for the 380 GeV CLIC machine have been overlaid to a 380 GeV light flavour $Z/\gamma^* \to q\bar{q}$ sample. The resulting efficiency as a function of the transverse momentum is shown in Figure 43(right). The effect of 380 GeV $\gamma\gamma \to$ hadron background

[4] The definition of reconstructable particle is the same as given for single particle efficiency in Section 4.2.1.

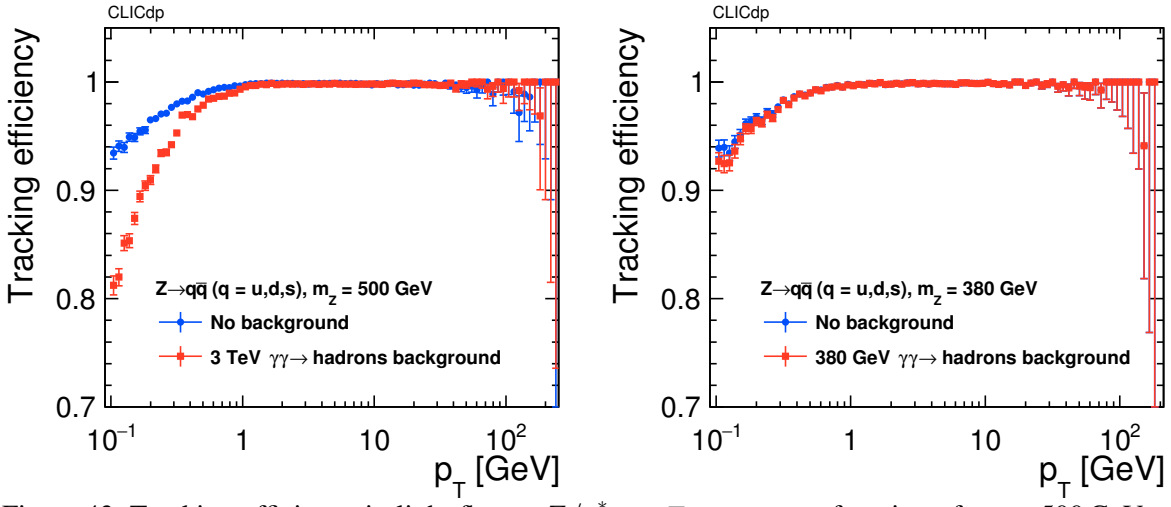

Figure 43: Tracking efficiency in light flavour $Z/\gamma^* \to q\bar{q}$ events as a function of p_T at 500 GeV, with and without 3 TeV $\gamma\gamma \to$ hadron background overlay (left), and at 380 GeV, with and without 380 GeV $\gamma\gamma \to$ hadron background overlay (right).

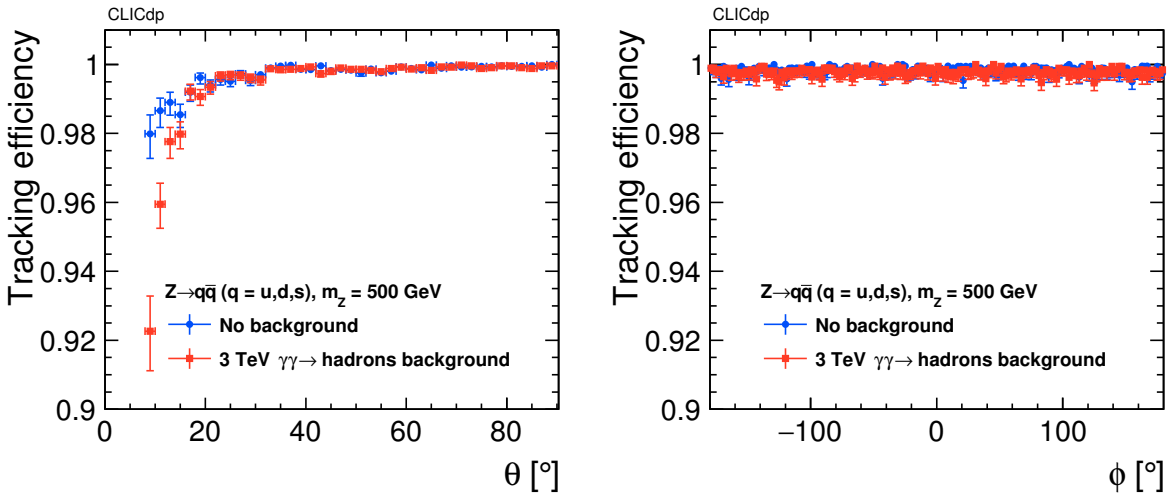

Figure 44: Tracking efficiency as a function of the polar (left) and the azimuthal (right) angle for 500 GeV light flavour $Z/\gamma^* \to q\bar{q}$ events, with and without 3 TeV $\gamma\gamma \to$ hadron background overlay.

is negligible. Therefore, performances are shown hereafter only for the overlay of 3 TeV $\gamma\gamma \to$ hadron background.

For 500 GeV light flavour $Z/\gamma^* \to q\bar{q}$ events, the tracking efficiency is shown in Figure 44 as a function of the polar (left) and the azimuthal angle (right). The following cuts are applied in these plots: $p_T > 1\,\text{GeV}$, $\Delta_{MC} > 0.02\,\text{rad}$, and a production radius smaller than 50 mm, with an additional cut in polar angle ($10^\circ < \theta < 170^\circ$) for Figure 44(right). Fully efficient performances are observed at all ϕ angles and in the whole θ range, with the exception of the region $10^\circ < \theta < 20^\circ$, where a maximum efficiency loss of 8% occurs with and a loss of 2% occurs without background overlay.

Finally, for the same events, the tracking efficiency as a function of the production vertex radius is shown in Figure 45. In this plot, the following cuts are applied: $p_T > 1\,\text{GeV}$, $10^\circ < \theta < 170^\circ$ and $\Delta_{MC} > 0.02\,\text{rad}$. The trend reflects the same behaviour observed for single displaced low-momentum muons in Figure 36, since the low-energy component of the particle spectrum dominates. Selecting $p_T > 10\,\text{GeV}$ allows one to remove the efficiency drop at $R = 50\,\text{mm}$. The effect of background amounts to at most a 1% efficiency loss for particles produced outside the vertex detector with $R \geq 60\,\text{mm}$.

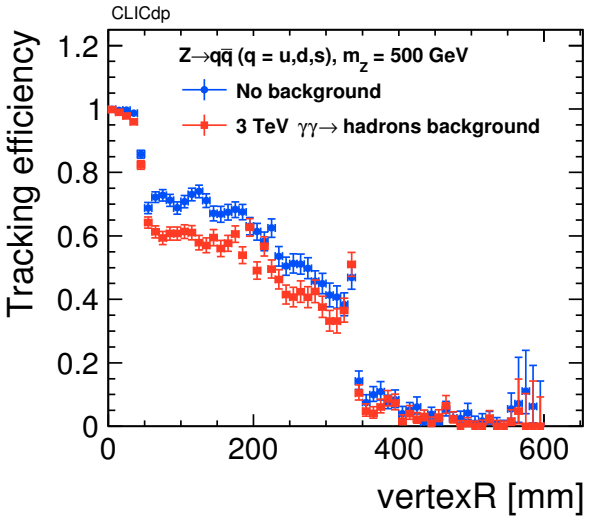

Figure 45: Tracking efficiency as a function of the production vertex radius for 500 GeV light flavour $Z/\gamma^* \to q\bar{q}$ events, with and without 3 TeV $\gamma\gamma \to$ hadron background overlay.

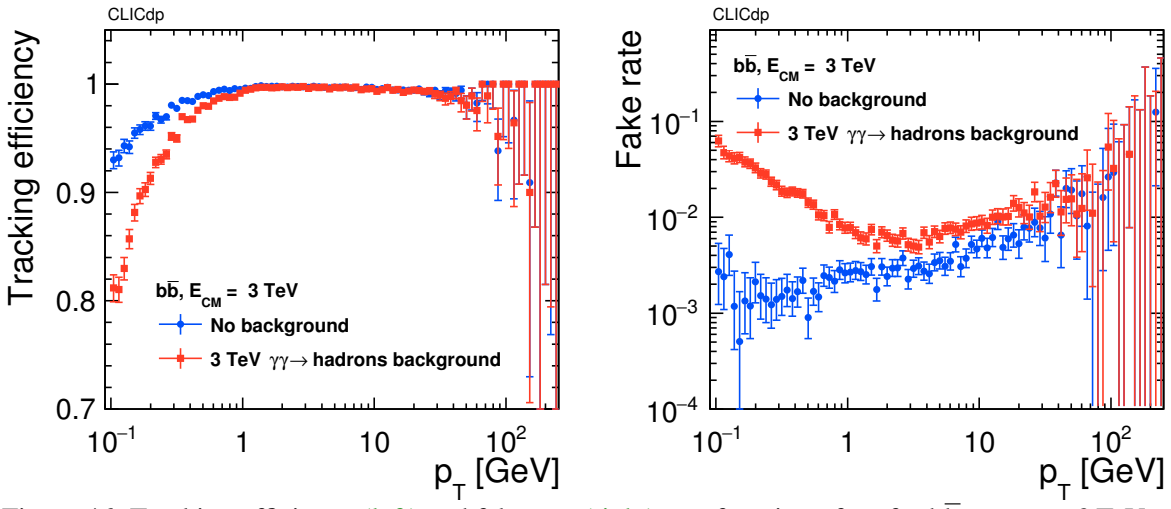

Figure 46: Tracking efficiency (left) and fake rate (right) as a function of p_T for $b\bar{b}$ events at 3 TeV, with and without 3 TeV $\gamma\gamma \to$ hadron background overlay.

More complex events allow one to complete the performance study with the evaluation of fake rate. Figures 46 to 48 show the efficiency (left) and fake rate (right) for $b\bar{b}$ events at 3 TeV as a function of the transverse momentum, particle proximity and production vertex radius. The corresponding cuts used for each plot are the same as for Z-boson events. Results are presented for the cases with and without 3 TeV $\gamma\gamma \to$ hadron background overlay. The trend of tracking efficiency as a function of all observables does not show a deviation from that of 500 GeV light flavour $Z/\gamma^* \to q\bar{q}$ events, proving that the performance is overall independent of the physics process and centre-of-mass energy. The fake rate increases as a function of the transverse momentum (Figure 46(right)) and with decreasing particle proximity (Figure 47(right)), due to the increased confusion in distinguishing, respectively, too straight tracks and tracks in more dense environment. Moreover, the fake rate increases with the production vertex radius (Figure 48(right)), suffering from the lower number of measurements (traversed layers) available. The effect of the $\gamma\gamma \to$ hadron background is particularly large for $p_T < 1$ GeV, in which case the fake rate increases by roughly one order of magnitude down to 100 MeV, where it reaches a maximum of 6%.

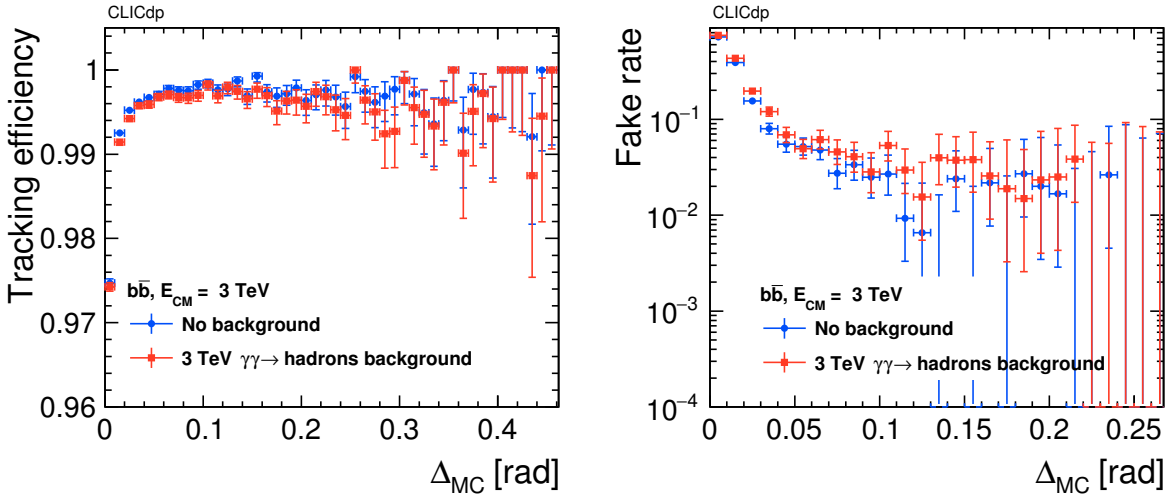

Figure 47: Tracking efficiency (left) and fake rate (right) as a function of the particle proximity Δ_{MC} for $\text{b}\bar{\text{b}}$ events at 3 TeV, with and without 3 TeV $\gamma\gamma \to$ hadron background overlay.

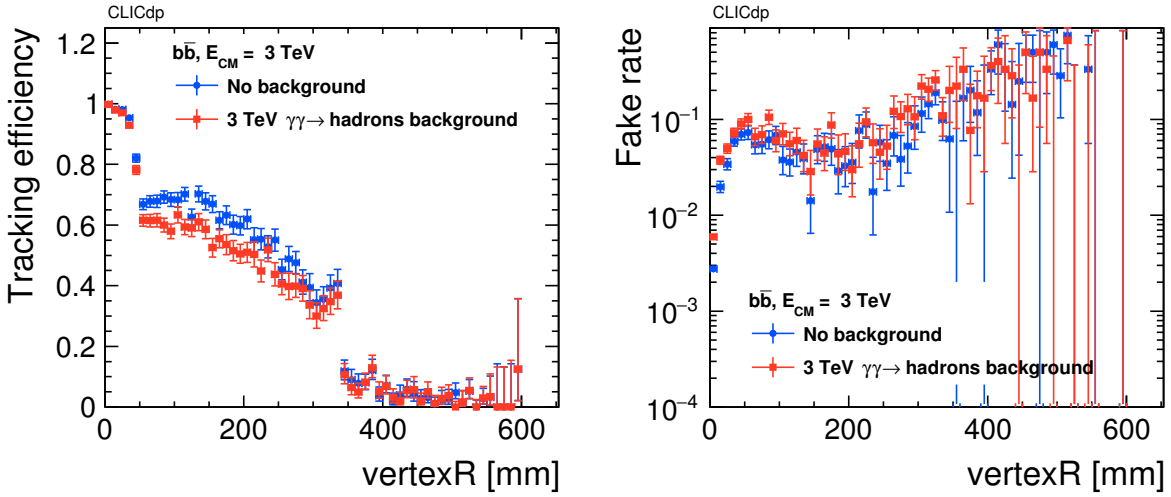

Figure 48: Tracking efficiency (left) and fake rate (right) as a function of the production vertex radius for $\text{b}\bar{\text{b}}$ events at 3 TeV, with and without 3 TeV $\gamma\gamma \to$ hadron background overlay.

For comparison, the same study has been performed for $\text{t}\bar{\text{t}}$ events at 3 TeV centre-of-mass energy. Efficiencies and fake rates are shown in Figures 49 to 51 as a function of the transverse momentum, particle proximity and production vertex radius, with and without 3 TeV $\gamma\gamma \to$ hadron background overlay.

The remarkable effect of $\gamma\gamma \to$ hadron background on the fake rate for tracks with $p_{\text{T}} < 1\,\text{GeV}$ is similar in $\text{t}\bar{\text{t}}$ and $\text{b}\bar{\text{b}}$ events. Effort is ongoing to improve the tracking efficiency and reduce the fake rate for prompt and displaced tracks at low transverse momenta.

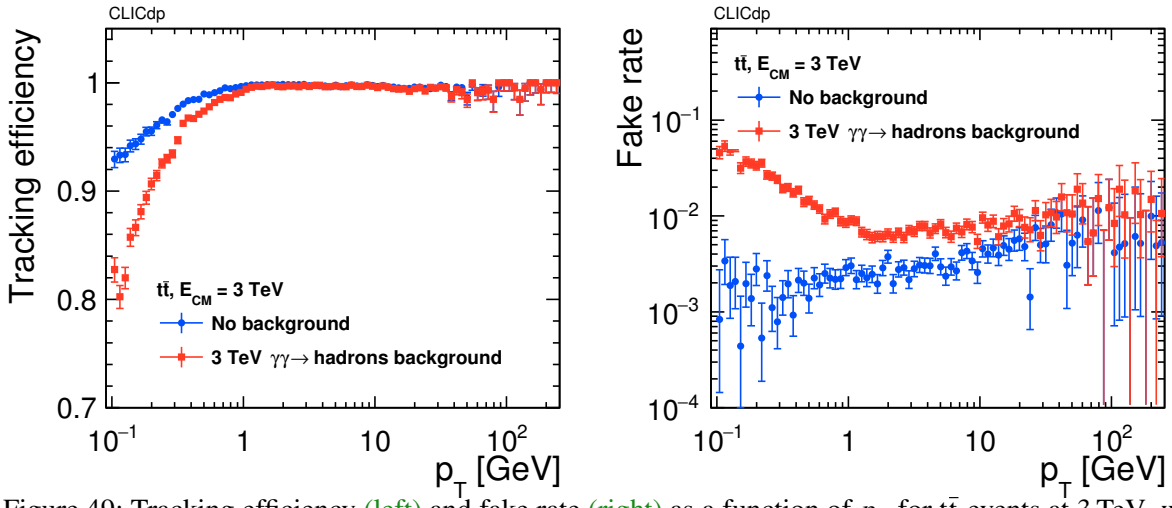

Figure 49: Tracking efficiency (left) and fake rate (right) as a function of p_T for $t\bar{t}$ events at 3 TeV, with and without 3 TeV $\gamma\gamma \rightarrow$ hadron background overlay.

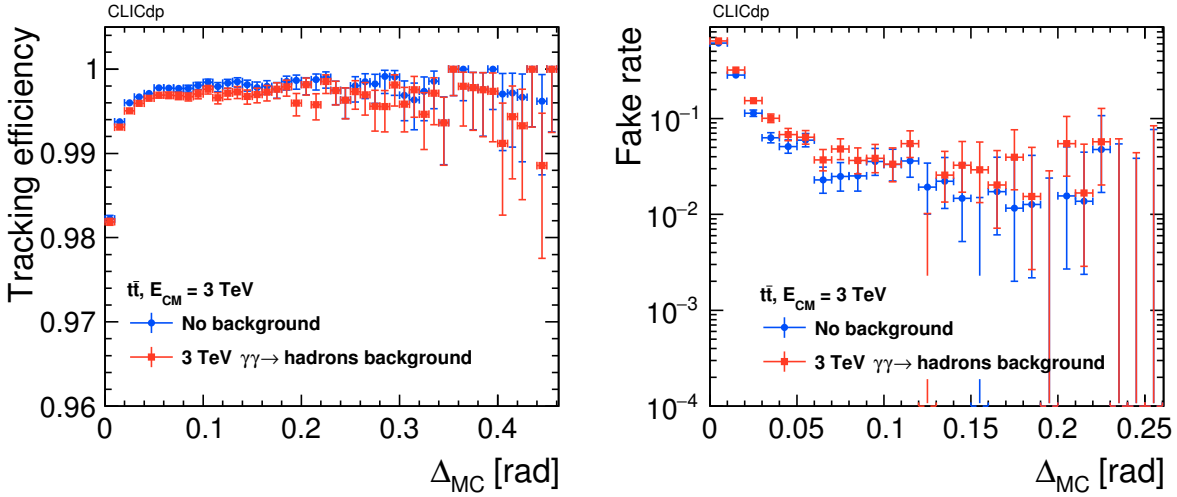

Figure 50: Tracking efficiency (left) and fake rate (right) as a function of the particle proximity Δ_{MC} for $t\bar{t}$ events at 3 TeV, with and without 3 TeV $\gamma\gamma \rightarrow$ hadron background overlay.

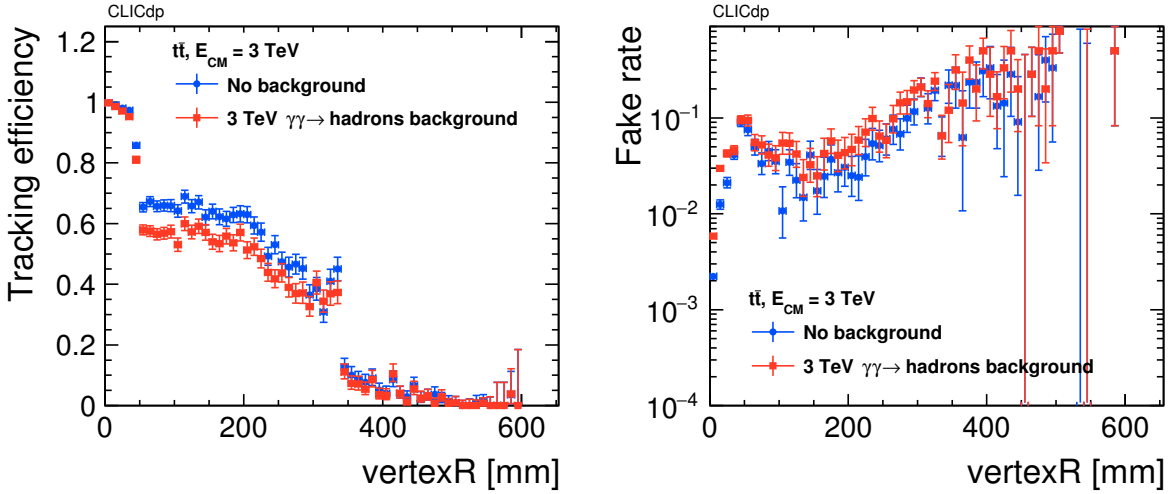

Figure 51: Tracking efficiency (left) and fake rate (right) as a function of the production vertex radius for $t\bar{t}$ events at 3 TeV, with and without 3 TeV $\gamma\gamma \rightarrow$ hadron background overlay.

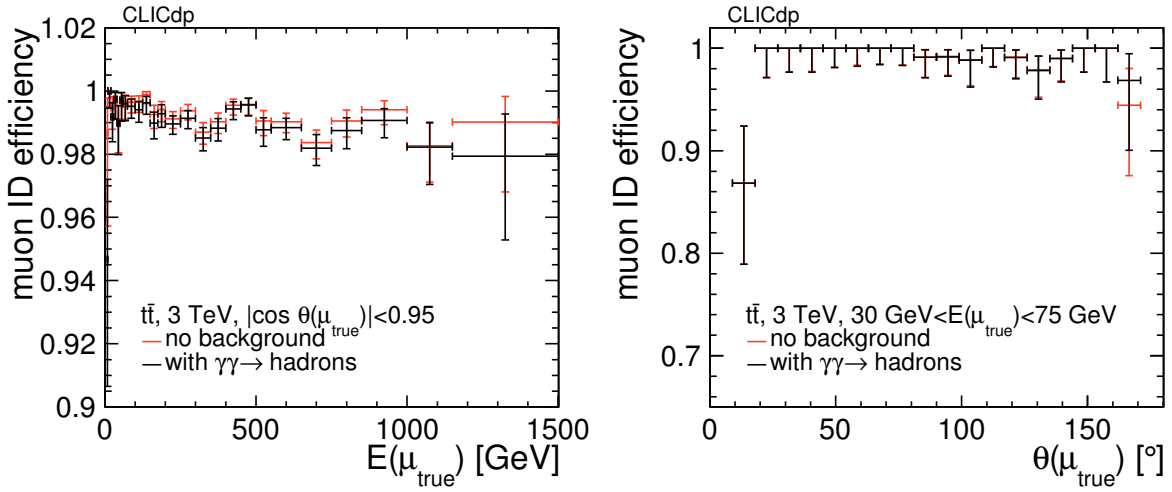

Figure 52: Muon identification efficiency in $t\bar{t}$ events at 3 TeV, without and with $\gamma\gamma \to$ hadron background overlay as a function of the energy for $|\cos\theta_{\mu^{\text{true}}}| < 0.95$ (left) and as a function of the polar angle θ in events with $30\,\text{GeV} < E_{\mu^{\text{true}}} < 75\,\text{GeV}$ (right).

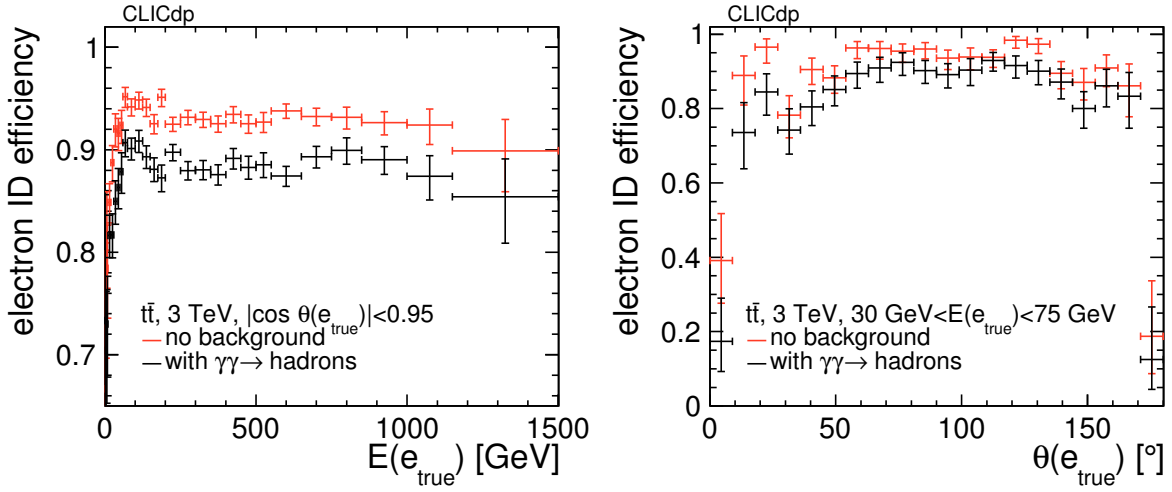

Figure 53: Electron identification efficiency in $t\bar{t}$ events at 3 TeV, without and with $\gamma\gamma \to$ hadron background overlay as a function of the energy for $|\cos\theta_{e^{\text{true}}}| < 0.95$ (left) and as a function of the polar angle θ in events with $30\,\text{GeV} < E_{e^{\text{true}}} < 75\,\text{GeV}$ (right).

Lepton Identification Lepton identification efficiencies for muons and electrons are studied in more complex $t\bar{t}$ sample at 3 TeV. Investigating the identification efficiency as a function of the lepton energy, an additional restriction of $|\cos\theta_{\text{lep}}| < 0.95$ is imposed to ensure the presence of a well-reconstructed track. In this study direct leptons from W decays are considered. Reconstructed leptons are required to be spatially matched within an angle of 1° around the "true" lepton momentum. The impact of beam background is evaluated by overlaying 30 BX of $\gamma\gamma \to$ hadron events. Muons are identified with more than 98% efficiency for all energies and polar angles, as shown in Figures 52(left) and 52(right). The impact of beam background on muon identification is negligible.

Electrons are correctly identified in 90% to 95% of all cases at energies of 20 GeV and higher, as illustrated in Figure 53(left). The identification efficiency is lower in the endcaps by about 5%, see Figure 53(right). In the presence of beam background the identification efficiency decreases by about 5% for all energies, both in barrel and endcaps.

4.2.3. Jet Energy Resolution

The accurate jet energy resolution obtained using highly granular calorimeters and Particle Flow algorithms, allows differentiating between different decays, e.g. between jets originating from W and Z boson decays. The jet performance in CLICdet is studied in di-jet events using Z/γ^* decays into light quarks (u, d, s) at several centre-of-mass energies. Tracks are reconstructed using either the ConformalTracking or TruthTracking. The Pandora particle flow algorithms [4–6] are used to reconstruct each particle, combining information from tracks, calorimeter clusters and hits in the muon system. Software compensation is applied to clusters of reconstructed hadrons to improve their energy measurement, using local energy density information provided by the high granularity of the calorimeter system [30]. The jet energy resolution is determined using the energy sum of all reconstructed particles $E_{\text{tot}}^{\text{PFOs}}$ compared to the sum of all stable visible particles on MC truth level [31] E_{true}. Since the vast majority of $Z/\gamma^* \to q\bar{q}$ events is reconstructed in a di-jet signature, this procedure effectively measures the energy resolution of jets with an energy of half the centre-of-mass energy E_{cm}, assuming that all particles are clustered into two jets. RMS_{90} is used as a measure for the jet energy resolution. RMS_{90} is defined as the RMS in the smallest range of the reconstructed energy containing 90% of the events [6]. This measure is a good representation for the resolution of the bulk of events, while it is relatively insensitive to the presence of tails. The relative energy resolution for a jet energy of $E_j = 1/2 \cdot E_{\text{cm}}$ is then calculated as $\Delta E_j/E_j = \sqrt{2} \cdot \text{RMS}_{90}(E_{\text{tot}}^{\text{PFOs}}/E_{\text{true}})/\text{Mean}_{90}(E_{\text{tot}}^{\text{PFOs}}/E_{\text{true}})$.

In a second method the response of particle-level jets (clustering stable visible particles, j_G) is compared to reconstructed jets at detector level (clustering PandoraPFOs, j_R), using the VLC algorithm [32] as implemented in the FastJet[5] library [33] in exclusive mode to force the event into two jets. The VLC algorithm combines a Durham-like inter-particle distance based on energy and polar angle with a beam distance. The algorithm applies a sequential recombination procedure, similar to those present in hadron collider algorithms, providing a robust performance at e^+e^- colliders with non-negligible background. For these studies, the VLC parameter values are $\gamma = \beta = 1.0$ and $R = 0.7$. The two reconstructed jets are required to be matched to each of the particle level jets within an angle of 10°. Studies using both methods in di-jet events lead to equivalent values of the jet energy resolution for most of the range as shown in Figure 54 for several jet energies as a function of the quark $|\cos\theta|$. For low energy jets at 50 GeV, the jet energy resolution values are around 4.5–5.5% for barrel ($|\cos\theta| < 0.7$) and endcap jets ($0.80 < |\cos\theta| < 0.925$). For jets beyond 150 GeV, the jet energy resolutions are between 3–4.0% over most of the angular range. For forward jets with $|\cos\theta|$ between 0.925 and 0.975 the jet energy resolutions increase by typically 0.5–2.0% points. For very forward jets with $0.975 < |\cos\theta| < 0.985$, the jet can be partly outside of the tracker volume.

Figure 55 shows that applying software compensation improves the energy resolution of jets significantly for most jet energies, for jets with $|\cos\theta| < 0.65$ by about 5–15%, for endcap jets with $0.8 < |\cos\theta| < 0.925$ by 5–10%. In events including beam-induced backgrounds from $\gamma\gamma \to$ hadrons from the 3 TeV collider the improvement is on a similar level for both detector regions.

As alternative the response distribution is fitted with a double sided Crystal ball function [34], using the Minuit2 library [35] as implemented in ROOT 6.08.00 [36]. The procedure starts by fitting a Gaussian over the full range, iteratively changing the fit range until the standard deviation σ of the fit stabilises within 5%. The range of the σ parameter of the Crystal Ball fit is restricted to be within a factor of 2 around the width of the Gaussian fit. Non-Gaussian tails are particularly significant in simulated data that include $\gamma\gamma \to$ hadron backgrounds. Figure 56 compares the resolutions obtained with RMS_{90} and the one from the Crystal Ball σ for different jet energies in events with 3 TeV $\gamma\gamma \to$ hadron beam-induced background. In events where 3 TeV beam-induced backgrounds from $\gamma\gamma \to$ hadrons are overlaid on the physics event, *tight* [6] selection cuts are applied to the PandoraPFOs prior to jet clustering.

[5] FastJet version 3.2.1. and FastJet Contrib version 1.025. The difference in the beam-distance calculation $d_{iB} = E_i^{2\beta}\left(\frac{p_{T,i}}{X}\right)^{2\gamma}$, where X is E_i instead of p_i (corrected in FastJet Contrib from 1.040), does not affect the results presented in this note.

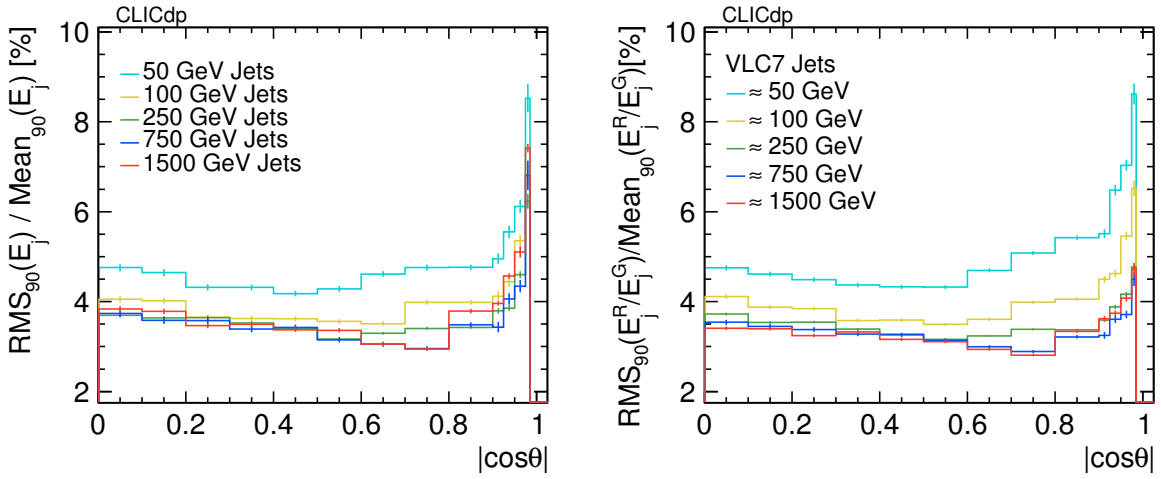

Figure 54: Jet energy resolution distributions for various jet energies as a function of the $|\cos\theta|$ of the quark using two methods. The first method compares the total reconstructed energy with the energy sum from all visible particles on MC truth (left). The second method compares the jet energy of reconstructed jets and matched MC truth particle jets, using the VLC algorithm with an $R = 0.7$ (VLC7, right)

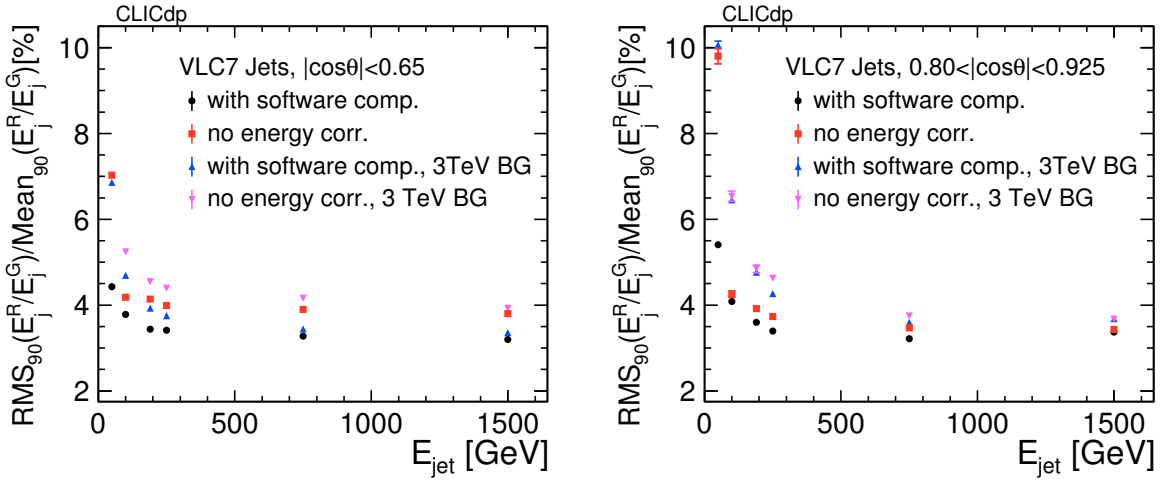

Figure 55: Jet energy resolution for central light flavour jets with $|\cos\theta| < 0.65$ (left) and endcap jets with $0.8 < |\cos\theta| < 0.925$ (right) in $Z/\gamma^* \to q\bar{q}$ events as a function of the jet energy with and without 3 TeV beam-induced backgrounds from $\gamma\gamma \to$ hadrons. PFO reconstruction without energy correction is compared to PFO reconstruction applying software compensation.

When 380 GeV $\gamma\gamma \to$ hadron backgrounds are used, the *low energy loose* [28] selection cuts are applied. These beam-induced backgrounds represent 30 bunch crossings. The mean of the jet energy response distribution $E_{\text{recojet}}/E_{\text{genjet}}$ between the reconstructed and the matched MC truth particle jet for events with and without beam-induced backgrounds ranges from 0.98 to 1.01 for jet energies between 50 GeV and 1.5 TeV for polar angles $|\cos\theta| < 0.95$, and 0.94 to 1.03 for forward jets with $0.95 < |\cos\theta| < 0.975$ [37]. For more forward jets with $0.975 < |\cos\theta| < 1.00$ the peak of the response distribution is still between 0.95 and 1.05 (depending on the jet energy), tails to lower energies are substantial and the mean of the distribution is between 0.98 and 0.85, gradually decreasing with jet energy. In general for the jet

energy response distributions, the standard deviation σ of the Gaussian core of the double-sided Crystal Ball fits are in good agreement with RMS_{90} values for almost all jet energies and polar angles, with jet energy resolution values of 3.5–10% for barrel and endcap jets in the presence of 3 TeV backgrounds (Figure 56). For 50 GeV jets, the σ of the fit is considerably lower than the RMS_{90} values, where a decrease is observed from 7% to 6% in the detector barrel for events with beam-induced backgrounds. For very forward jets, the σ of the double-sided Crystal Ball function does not account for the sizeable non-Gaussian tails of the jet energy response and thus the RMS_{90} values are considerably larger. Jet energy resolutions are around 3.5–4.5% for large jet energies beyond 200 GeV, using either measure for quantification. In the forward region ($|\cos\theta| > 0.925$) the σ of the fit is below 6% for most jet energies. The beam-induced background leads to larger tails in the jet energy response distribution in this detector region, which are reflected in the larger values of the RMS_{90} measure. Compared to jet energy resolution values in events without $\gamma\gamma \to$ hadron backgrounds (Figure 54), a degradation of the jet energy resolution is observed for all jet energies. The effect is most pronounced for low energy jets, e.g. for 50 GeV jets, where the increase is from around 4.5% to 7.5%. For high energy jets, the jet energy resolution increase is limited to less than 0.5% points for most of the $|\cos\theta|$ range. Since hadrons from beam-induced backgrounds tend to be produced more in the forward direction, their impact is larger for endcap and forward jets than for barrel jets. For low energy jets the jet energy resolution values are significantly better than those obtained by ATLAS [38] and CMS [39].

In events with overlay of 380 GeV beam-backgrounds from $\gamma\gamma \to$ hadrons, *low energy loose* selection cuts [28] are applied on the PandoraPFOs, to reflect the lower levels of beam-induced backgrounds of the 380 GeV accelerator relative to the 3 TeV accelerator. The impact of beam-induced backgrounds for the 380 GeV accelerator on the jet energy resolution is illustrated by Figure 57. For jet energies above 100 GeV, the 380 GeV beam-induced background levels lead to almost no increase of the jet energy resolution for barrel and endcap jets. Around 0.5–1.0% points can be observed for forward jets. Even for 50 GeV jets in the barrel, 380 GeV beam -induced backgrounds lead only to a mild increase of the jet energy resolution to about 5%. In the outermost part of the barrel and endcaps the jet energy resolution for 50 GeV jets is increased to about 5.5–6.0%, as well as an absolute increase of 2% points and more for forward jets.

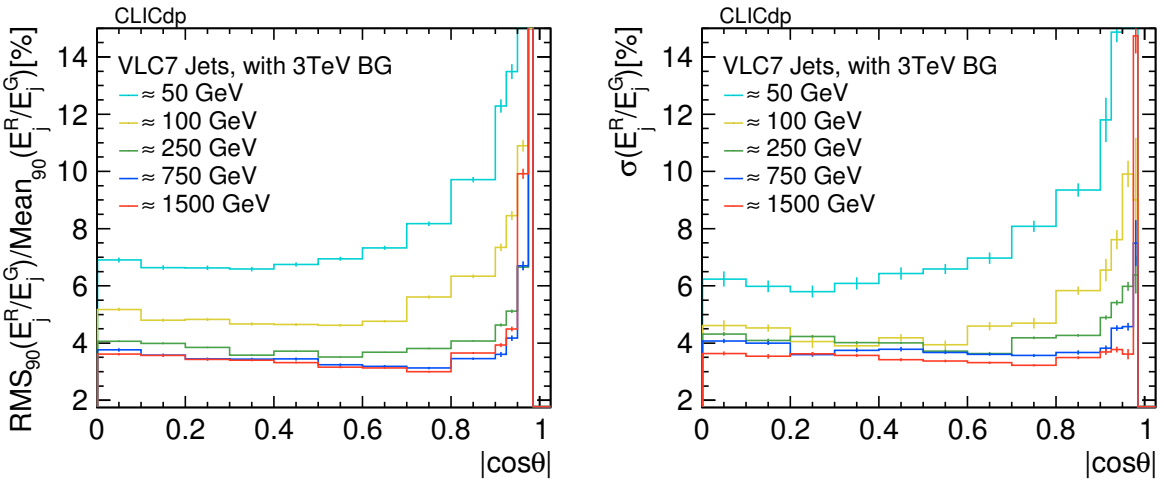

Figure 56: Jet energy resolution for various jet energies as a function of the $|\cos\theta|$ of the quark with 3 TeV $\gamma\gamma \to$ hadron background overlaid on the physics di-jet event. In the first method RMS_{90} is used as measure of the jet energy resolution (left), the standard deviation σ of the Gaussian core of the double-sided Crystal Ball fit quantifies the jet energy resolution in the second method (right). Tight PFO selection cuts are used.

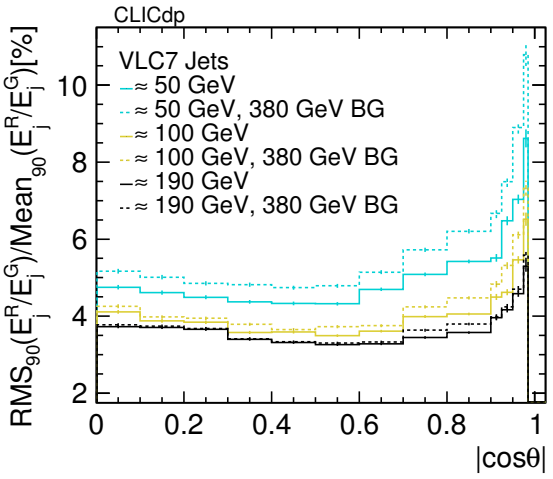

Figure 57: Jet energy resolution for various jet energies as a function of the $|\cos\theta|$ of the quark with and without 380 GeV $\gamma\gamma \to$ hadron background overlay on the physics di-jet event. RMS_{90} is used as measure of the jet energy resolution. Low energy loose PFO selection cuts are used for events with background.

The jet angular resolutions in azimuth ϕ and polar angle θ are studied as functions of jet energies for different regions in polar angle. For events having significant final state gluon radiation, three jets reflect the event topology better than two jets. Since the jet algorithm is run in exclusive mode with two jets, this can lead to a significant bias in jet angular resolutions. In order to diminish the impact of this bias, events are preselected, where the two particle level MC truth jets are back-to-back in azimuth $\Delta\phi(j1,j2) > 2.8 \approx 160^\circ$, which vetoes against underlying multi-jet topologies. Each of the reconstructed jets is matched to its closest MC truth particle level jet. The distribution of ϕ resolutions are studied as a function of the polar angle, and as a function of the jet energy. The detector is divided into four regions of $|\cos\theta|$: the barrel, the transition region (where the jet energy is reconstructed both in barrel and endcap parts of the detector), the endcap, and the forward region. Resolutions in ϕ vary for all energies for almost all regions between 0.3° and 1.0°, as Figure 58 shows. The jet θ resolutions values are slightly better with RMS_{90} values between 0.2° and 0.5° for all energies in almost all detector regions. Once beam backgrounds from $\gamma\gamma \to$ hadrons are overlaid, the θ resolutions increase for 50 GeV jets from 0.5° to about 1.0° (see Figure 59), while for the remaining jet energies the θ resolutions remain around 0.3° to 0.5°. A slight increase in angular resolution for more forward jets can be observed. For jet ϕ resolutions in the barrel region and for most jet energies, the values remain at a similar level between 0.4° to 0.7°; for more forward jets and for all energies, the ϕ resolutions increase relatively by around 25–50%.

4.2.4. Missing Transverse Energy Resolution

The impact of beam background is studied at 3 TeV using missing transverse momentum in light flavour di-jet events and events from semi- and di-leptonic $t\bar{t}$ with genuine missing energy due to neutrinos escaping detection in the detector. The background is simulated using 30 bunch-crossings with on average 3.2 $\gamma\gamma \to$ hadron events per bunch-crossing, overlaid on top of the physics event. At 3 TeV around 1.6 TeV of additional energy is deposited in the reconstruction time window on top of the underlying physics events. In order to mitigate beam background effects p_T and timing cuts (see Section 4.1.4) have been developed for each reconstructed particle type. These aim to reduce the additional energy attributed to beam background to the level of about 100 GeV. Figure 60(left) shows the distribution of the difference between the true and the reconstructed missing transverse momentum originating from neutrinos. The preselection on centrally produced tops avoids a bias due to detector acceptance. The $\gamma\gamma \to$ hadron

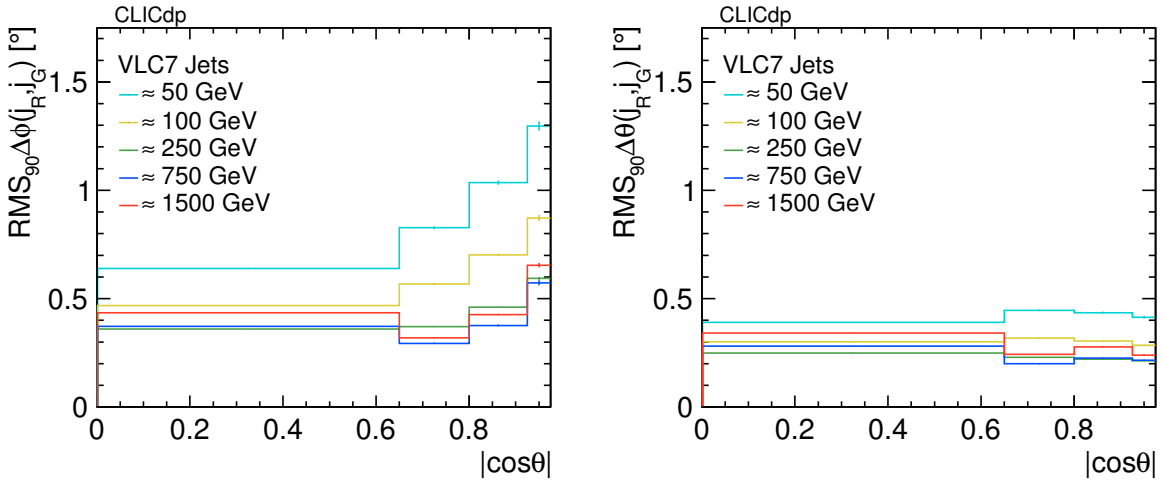

Figure 58: Jet ϕ (left) and θ (right) resolutions for several jet energies in four $|\cos\theta|$ bins in events without any simulation of beam-induced background effects.

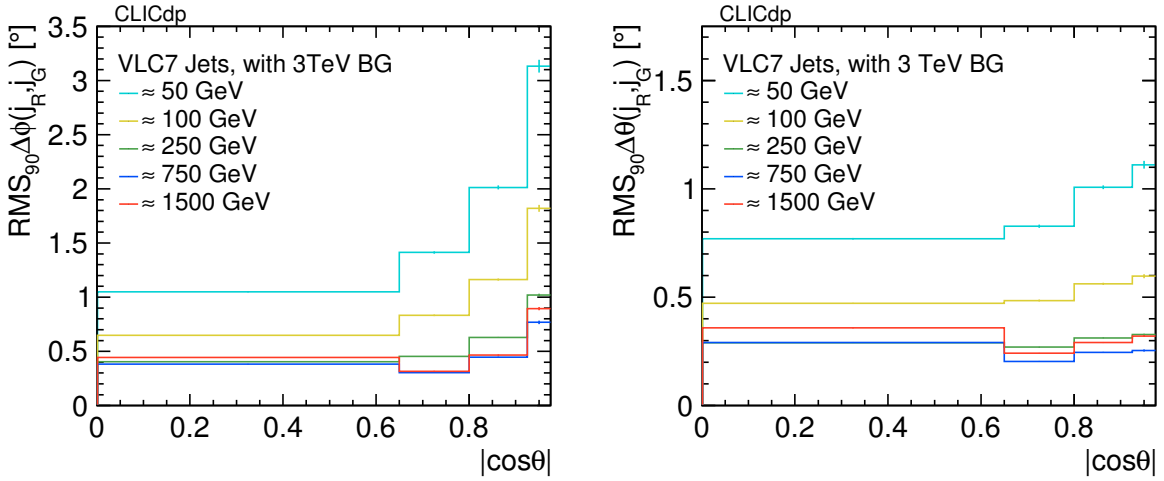

Figure 59: Jet ϕ (left) and θ (right) resolutions for several jet energies in four $|\cos\theta|$ bins in events with 3 TeV beam-induced backgrounds from $\gamma\gamma \to$ hadrons, using tight PFO selection cuts.

background leads to a considerable deterioration of the missing transverse momentum resolution. Applying the p_T cuts and timing cuts on reconstructed particles improves the missing transverse momentum resolution. In events without genuine missing momentum the deterioration in the missing momentum resolution of 20% is reduced to a level of 5% after the selection cuts (Figure 60(right)). The bias in the missing p_T comes from the Lorentz boost of the collision with respect to the detector frame of reference due to the crossing angle, there is a momentum bias towards positive x-direction.

4.2.5. W and Z Mass Separation

The precise reconstruction of masses of resonances in hadronic channels over wide ranges of energies is a challenging task. The ability to separate di-jet masses from hadronic decays of W and Z bosons is studied using the Pandora reconstruction algorithms. The study is carried out using simulated di-boson events, in which only one of the bosons decays into di-quarks, i.e. $ZZ \to \nu\bar{\nu}q\bar{q}$ and $WW \to l\nu qq$. The boson energies in this study vary from 125 GeV, where both bosons are created almost at rest, up to

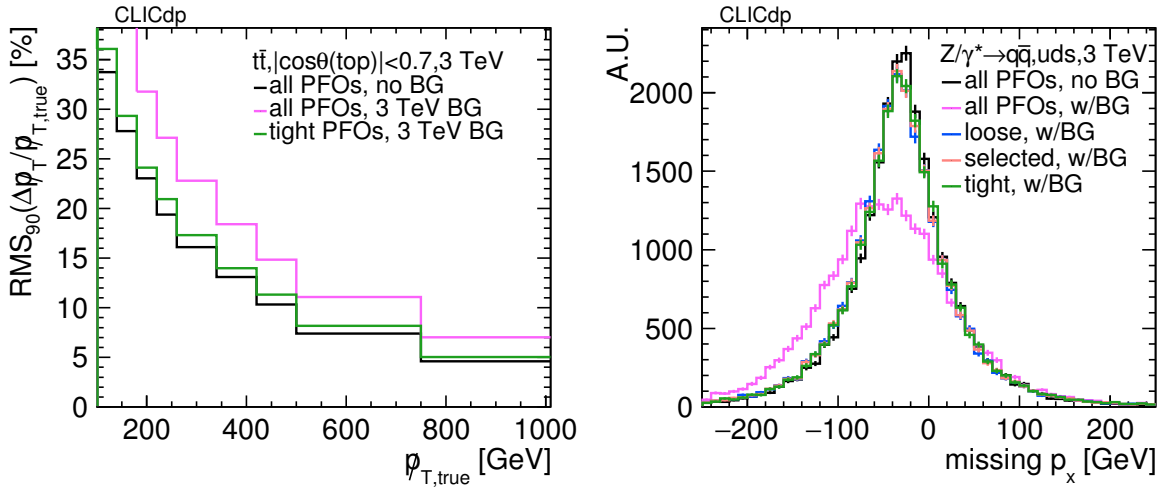

Figure 60: Impact of 3 TeV beam-induced $\gamma\gamma \to$ hadron background overlay on the missing momentum distribution using different preselections on particle flow objects in semi- and di-leptonic $t\bar{t}$ events with genuine missing momentum (left) and in light flavour di-jet events with no genuine missing momentum (right).

1 TeV, where the bosons are strongly boosted. For each vector boson energy, samples were produced without background (no BG) and with 3 TeV beam-induced backgrounds from $\gamma\gamma \to$ hadrons overlaid, representing 30 bunch crossings (3 TeV BG). For low energy bosons of 125 GeV the impact of 380 GeV beam-induced backgrounds is also investigated. Events are reconstructed using the VLC algorithm with parameters $R = 0.7$, $\gamma = \beta = 1$ in exclusive mode, forcing the event into two jets. Prior to jet clustering at particle level, the true charged lepton from the W is removed (together with any associated photons from final state radiation and Bremsstrahlung). At detector level, all reconstructed particles within a cone of $|\cos\alpha| < 0.9$ around the true lepton direction are removed prior to jet clustering. This procedure has virtually no impact on particles from the hadronically decaying W. At particle level, visible stable particles (excluding neutrinos) are used as input for the jet clustering. On the reconstruction level for the no BG samples, all Pandora particle flow objects are used as input for the jet clustering, while tight (low energy loose) selected Pandora particle flow objects are used in the samples including 3 TeV (380 GeV) $\gamma\gamma \to$ hadron backgrounds. To ensure that the event is well contained within the detector acceptance, a cut is imposed on the polar angle of both MC truth jets $|\cos\theta| < 0.9$.

The upper tail and the core of the di-jet mass distribution is described well by a Gaussian function even without this additional preselection criteria for all energies. The di-jet distributions are fitted with a Gaussian, iteratively changing the upper limits of the fit range to 2 σ and the lower fit limit to 2 σ (1 σ without preselection criteria applied to the unclustered energy ratio for 125 GeV bosons), until the fitted σ stabilises within 5%. Figure 61 shows the di-jet mass distributions for W and Z bosons with $E = 500$ GeV with the Gaussian fits in events without and with the simulation of 3 TeV beam-induced backgrounds from $\gamma\gamma \to$ hadrons.

Since the di-jet mass distributions are not further calibrated at the moment, the mean of the fit is shifted to the W or Z mass, fixing the ratio of σ/mean. The rescaled Gaussian distributions are normalised, such that the integral of the distributions is 1. The overlap fraction A_O is then defined by

$$A_O = \left(\int_{x_{int}}^{\infty} \text{gauss}_W(x)\mathrm{d}x + \int_{-\infty}^{x_{int}} \text{gauss}_Z(x)\mathrm{d}x \right) /2,$$

where x_{int} is the intersection mass point of the Gaussian fit of the W and Z di-jet mass distributions between the W and Z masses. The efficiency ε of selecting W's or Z's are represented by the integrals of the Gaussian curves up to x_{int} for W's and from x_{int} onwards for Z's. The ideal Gaussian separation is

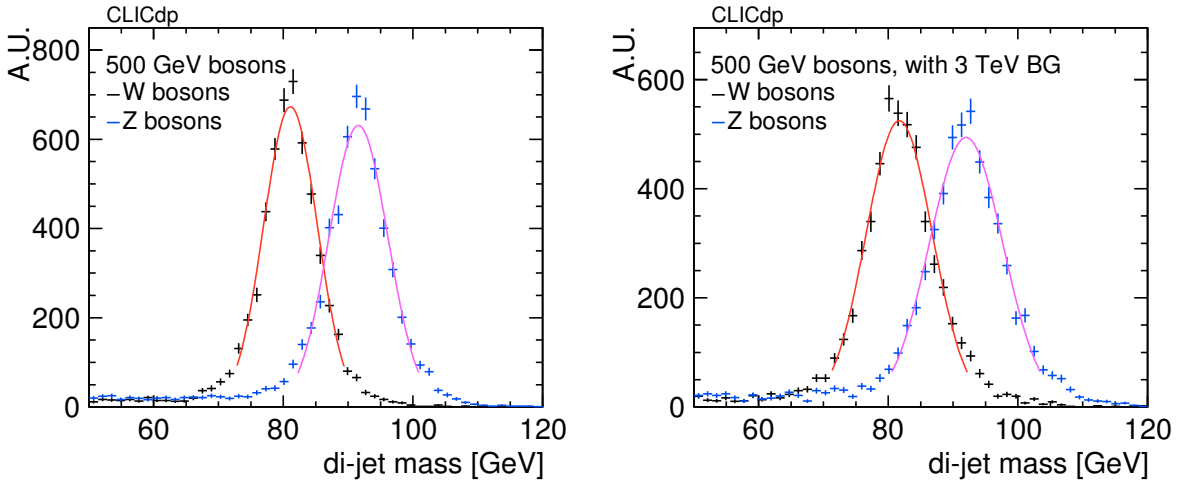

Figure 61: Di-jet mass distributions of hadronically decaying W and Z with $E = 500\,\text{GeV}$ in $\text{WW} \to \text{l}\nu\text{qq}$ and $\text{ZZ} \to \nu\bar{\nu}\text{q}\bar{\text{q}}$ events, together with Gaussian fits of the di-jet mass for events without beam-induced backgrounds (left) and overlay of 3 TeV beam-induced backgrounds from $\gamma\gamma \to$ hadrons (right).

Table 8: Mass resolutions, identification efficiencies, and separation of W and Z peaks for reconstructed W and Z's at different energies, with and without overlaid beam-induced backgrounds from $\gamma\gamma \to$ hadrons. Tight PFO (Low energy loose) selection cuts are used for events with 3 TeV (380 GeV) background.

Background	$E_{\text{W,Z}}$ [GeV]	$\sigma_{m(\text{W})}/m(\text{W})$ [%]	$\sigma_{m(\text{Z})}/m(\text{Z})$ [%]	ε [%]	Separation [σ]
no BG	125	5.5	5.3	88	2.3
	250	5.3	5.4	88	2.3
	500	5.1	4.9	90	2.5
	1000	6.6	6.2	84	2.0
3 TeV BG	125	7.8	7.1	80	1.7
	250	6.9	6.8	82	1.8
	500	6.2	6.1	85	2.0
	1000	7.9	7.2	80	1.7
380 GeV BG	125	6.0	5.5	87	2.2

evaluated using the quantile function with the normal distribution[6]. A different approach using the average mass resolution $\sigma_{\text{avg}} = (\sigma_{\text{Z}} + \sigma_{\text{W}})/2$ found the same results for the separation $\mathscr{S} = (m_{\text{Z}} - m_{\text{W}})/\sigma_{\text{avg}}$.

The di-jet mass resolutions are listed in Table 8, together with identification efficiencies and the separation between W and Z peaks. In events without beam-induced background effects the selection efficiency is between 84% and 90%, which corresponds to an overlap fraction of 10–16%. For very boosted bosons the mass resolution is slightly worse than for bosons at rest or with moderate energies. Once 3 TeV beam-induced backgrounds from $\gamma\gamma \to$ hadrons are taken into account (3 TeV BG), the W and Z selection efficiencies decrease to 80–85%, which corresponds to overlap fractions of 15–20%. The degradation is worse for lower boson energies. The peak separation diminishes from 2.0–2.5 σ to about 1.7–2.0 σ in

[6] separation calculation using ROOT 6.08.00: $2 \cdot |\text{ROOT :: Math :: normal\_quantile}(A_{\text{O}}, 1)|$

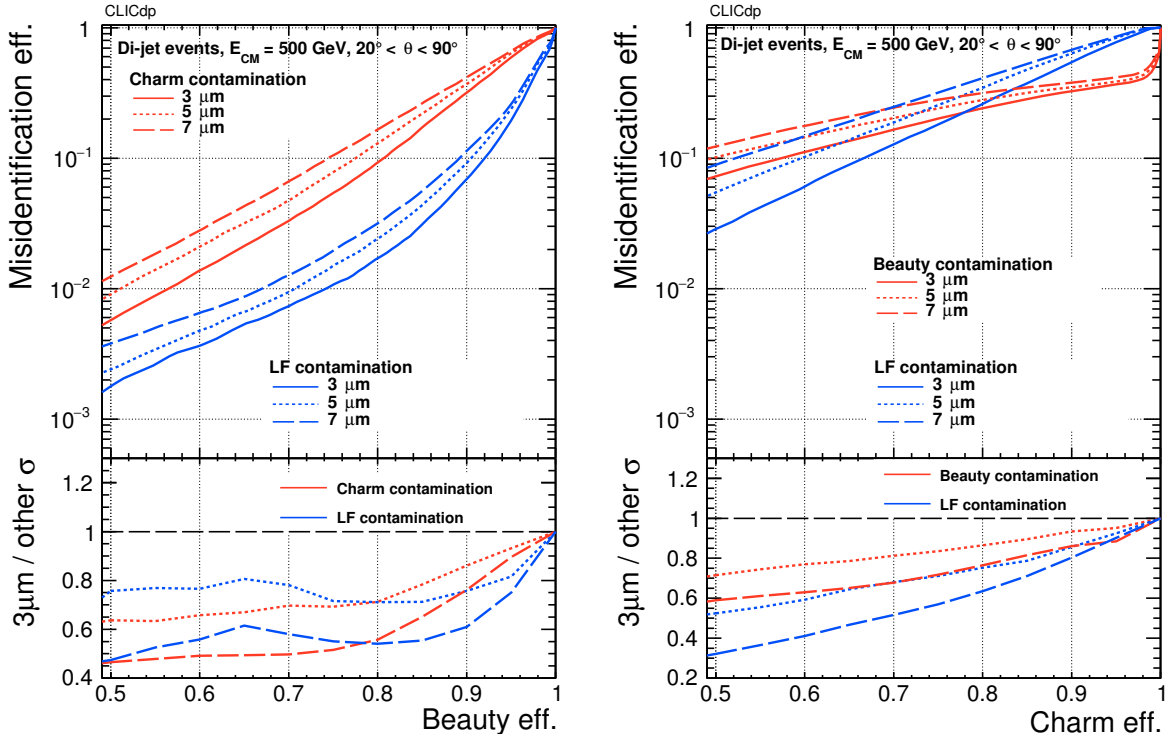

Figure 62: Global performance of beauty tagging (left) and charm tagging (right) for jets in di-jet events at $\sqrt{s} = 500\,\text{GeV}$ with a mixture of polar angles between 20° and 90°. A comparison of performance obtained with different single point resolutions in the vertex detector is presented. On the y-axis, the misidentification probability and the ratio of misidentification probabilities with respect to the nominal (3 µm) single point resolution are given.

the presence of beam-induced background levels of the 3 TeV accelerator. As alternatives, *loose*, *default* and no selection cuts have been applied to PandoraPFOs prior to jet clustering in simulated events with 3 TeV beam-induced backgrounds. These three alternative selection cuts led to wider di-jet mass distributions and a diminished separation power between the two mass peaks. For 380 GeV beam-induced background levels there is a mild effect on the separation power, decreasing from 2.3 σ to 2.2 σ.

4.2.6. Flavour Tagging

Flavour tagging studies were performed initially in the CDR [1, Section 12.3.4] for the CLIC_SiD detector model. These studies were extended [40] to explore more realistic vertex detector geometries, e.g. using spirals instead of forward disks, thus allowing for air flow cooling of the vertex detector system. One of the main findings is related to the material budget: doubling the material per layer in the vertex detector (as required for the more realistic design adapted for CLICdet) leads to a degradation of the flavour tagging performance.

The vertex detector geometry of CLICdet has recently been used for additional studies, using the software chain described in Section 4.1 and the flavour tagging package LCFIPlus [41]. Complementing the above-mentioned exploratory studies, as a first step the dependence of performance on the assumed single point resolution in the vertex detector layers was investigated. The combined impact on flavour tagging performance, when worsening the single point resolution from the nominal 3 µm to 5 µm or 7 µm, was investigated using di-jet samples at 500 GeV and is shown in Figure 62. As expected, the results get worse for the less performant vertexing.

The overall performance of flavour tagging at CLICdet has been tested using the nominal parameters

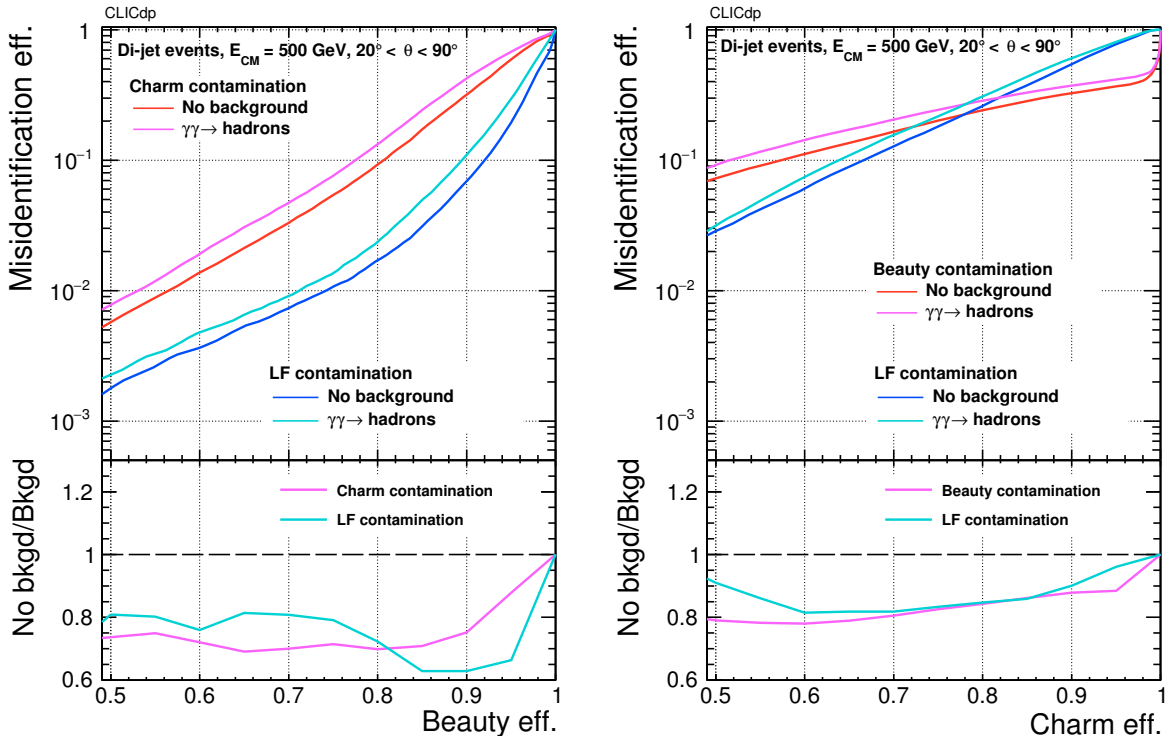

Figure 63: Global performance of beauty tagging (left) and charm tagging (right) for jets in di-jet events at $\sqrt{s} = 500\,\text{GeV}$ with a mixture of polar angles between 20° and 90°. A comparison of performance with and without $\gamma\gamma \to$ hadron background is presented. On the y-axis, the misidentification probability and the ratio of the misidentification probabilities with and without $\gamma\gamma \to$ hadron background are given.

(i.e. 3 µm position resolution), and comparing the beauty and charm tagging results without and with overlay of $\gamma\gamma \to$ hadron background corresponding to 30 bunch crossings. Figure 63 shows the results obtained. The beauty misidentification probability (Figure 63(left)) is assessed separately for charm and light-flavour contamination. At 80% beauty identification efficiency, the misidentification amounts to 10% as charm and 1.5% as light-flavour jets. When 3 TeV $\gamma\gamma \to$ hadron background is overlaid, it amounts to 13% and 2% for charm and light-flavour respectively. Similarly, the charm misidentification probability (Figure 63(right)) is assessed for beauty and light-flavour contamination separately. At 80% charm identification efficiency, the misidentification amounts to 25% as beauty as well as light-flavour jets. When 3 TeV $\gamma\gamma \to$ hadron background is overlaid, it amounts to 30% for both types of contamination.

In order to estimate the impact of track reconstruction on the flavour tagging, the same study has been performed using the true (Monte Carlo) pattern recognition, dubbed *TruthTracking*. The results, shown in Figure 64, indicate that both beauty and charm tagging can be improved by optimising the pattern recognition. In particular, in beauty tagging a reduction of misidentification of a b-quark as a c- or light quark by 20% to 30% can be expected.

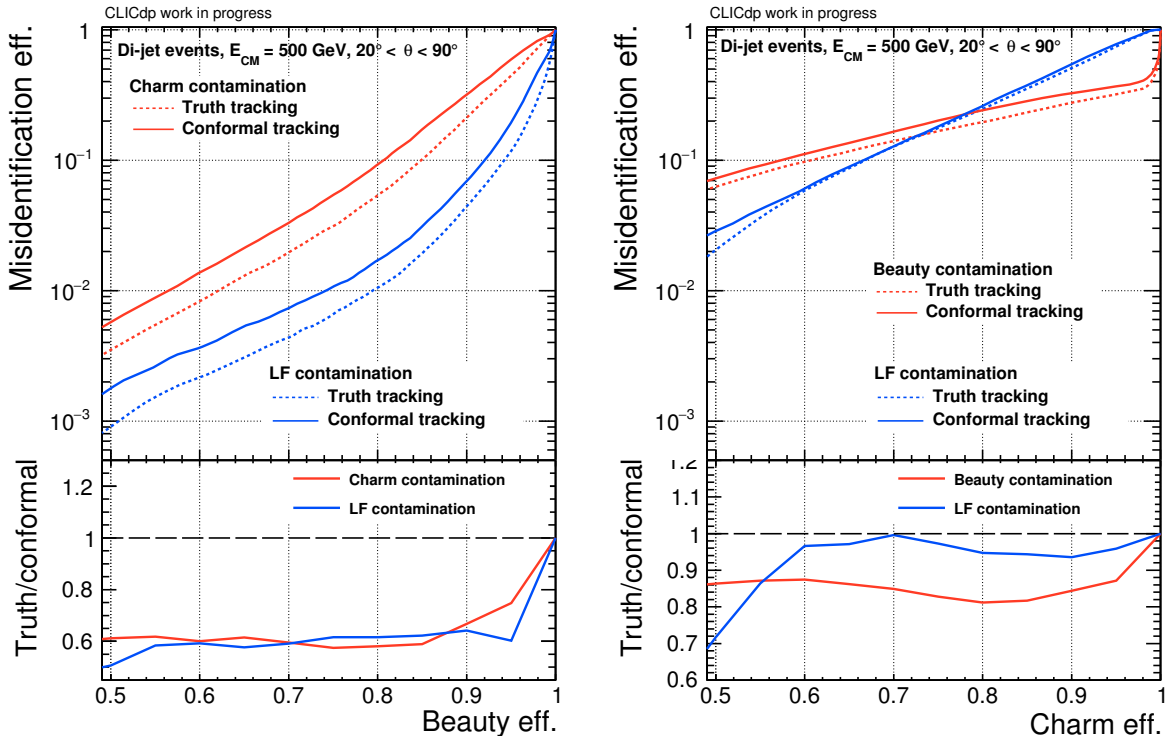

Figure 64: Performances of beauty tagging (left) and charm tagging (right) for jets in di-jet events at $\sqrt{s} = 500\,\text{GeV}$ with a mixture of polar angles between 20° and 90°. A comparison of performance using TruthTracking with respect to ConformalTracking is shown. On the y-axis, the misidentification probability and the ratio of the misidentification probabilities with and without $\gamma\gamma \to$ hadron background are given.

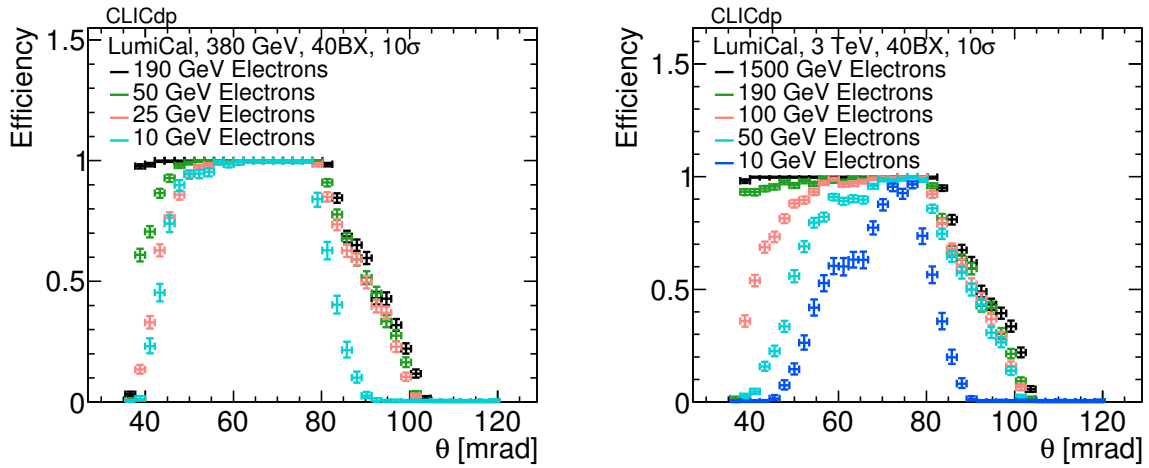

Figure 65: Efficiency of electron detection as a function of the polar angle in the LumiCal for 380 GeV (left) and 3 TeV (right) collisions.

4.2.7. Performance of Very Forward Calorimetry

The efficiencies and fake rates for the LumiCal and BeamCal were studied with mono-energetic electrons of 10 GeV, 25 GeV, 50 GeV, 100 GeV, 190 GeV, 250 GeV, 500 GeV, 1000 GeV and 1500 GeV created in the polar angle range from 9 mrad to 120 mrad. The reconstruction was done with incoherent pair background for the CLIC beams of $\sqrt{s} = 380\,\text{GeV}$ with $L^* = 6\,\text{m}$ and $\sqrt{s} = 3\,\text{TeV}$ with $L^* = 6\,\text{m}$. Because both the LumiCal and BeamCal will have to integrate the signal over multiple bunch crossings, backgrounds equal to 20 ns or 40 bunch crossings were overlaid over each signal electron. Energy deposits for each background event have been recorded and the standard deviation of the distribution calculated. For the LumiCal the pulse height threshold for pad selection was chosen to be 10 standard deviations, and 3 standard deviations for the BeamCal. Details of the analysis, using the "variable energy selection" procedure for pad selection, as well as the methods for tower selection and cluster location are described in [27]. The reconstruction criteria can be adapted, depending on the requirements of the physics analysis, whether higher efficiency or lower fake rates are more beneficial.

For the estimate of the efficiencies and fake rates, an electron is considered to be reconstructed if the angle and energy are matching between the generated electron and the reconstructed cluster. If no matching electron exists a cluster is considered to be *fake*. The reconstructed cluster has to match the generated electron by 5 mrad in polar angle θ, for the azimuthal angle ϕ the conditions[7] $|\cos\phi_{\text{rec}} - \cos\phi_{\text{MC}}| < 0.35$ and $|\sin\phi_{\text{rec}} - \sin\phi_{\text{MC}}| < 0.35$ need to be fulfilled, and the energy needs to be within 50% of the generated value. The conditions are aimed at the worse resolutions of the BeamCal due to the large amount of incoherent pairs affecting the angular and energy resolutions.

The efficiency for the electron reconstruction in the LumiCal is shown in Figure 65. The 190 GeV electrons, the highest energy for the $\sqrt{s} = 380\,\text{GeV}$ case, are well reconstructed between 40 mrad and 85 mrad. At the lower edge of the LumiCal the angular and energy resolutions degrade due to leakage. Starting at about 85 mrad the beam pipe close to the vertex detector starts to shadow the LumiCal, which causes the electrons to shower and degrades the reconstruction efficiency. Due to the background and the selection of the pads with energy deposits significantly above the average backgrounds, the reconstruction efficiency for lower energy electrons is degraded at the inner edge of the LumiCal.

For the $\sqrt{s} = 3\,\text{TeV}$ case electrons between 1.5 TeV and 190 GeV are reconstructed with an efficiency above 90%, for all angles until the LumiCal is shadowed by the beam pipe. For lower energies the background impacts the reconstruction efficiency more and more. 10 GeV electrons can only be reconstructed

[7] This approximately corresponds to $|\phi_{\text{rec}} - \phi_{\text{MC}}| = 25^\circ$, but also takes into account the problem of 0° being equivalent to 360°.

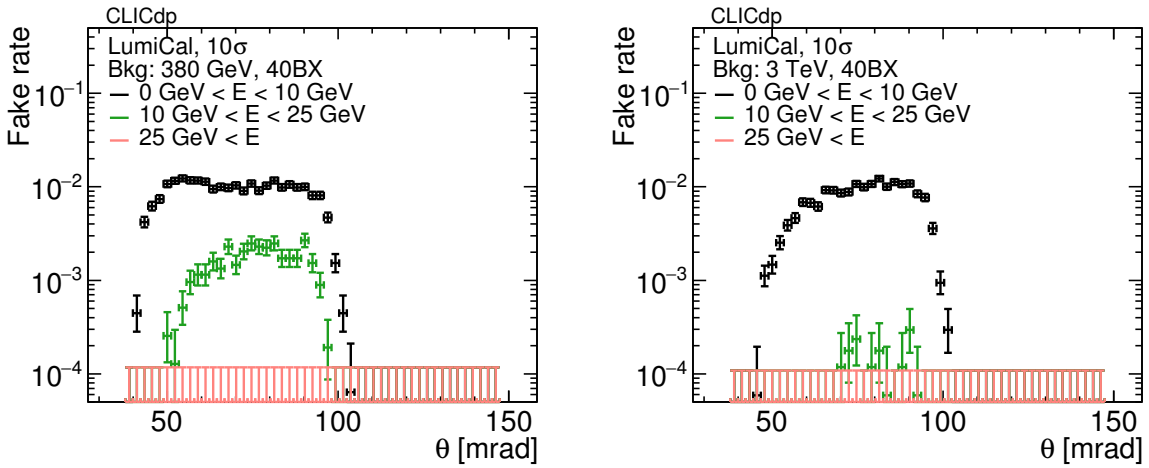

Figure 66: Fake rate for electron reconstruction as a function of the polar angle in the LumiCal at 380 GeV (left) and 3 TeV (right).

with 90% efficiency in the narrow angular region from 70 mrad to 80 mrad.

The achievable efficiencies to identify signal electrons are closely related to the acceptable fake rates (i.e. a background event is identified as signal electron), which are shown in Figure 66. Both for 380 GeV and 3 TeV CLIC the fake rate for energies up to 10 GeV is around 1% between 50 mrad and 80 mrad. For a similar angular region, a fake rate of a few permille is observed for 10 GeV to 25 GeV clusters, and the probability is below 10^{-4} to find any fake clusters above 25 GeV. For the absolute luminosity measurement the highest energy electrons are important, which are already reconstructed with high efficiency using the procedure described above. For studies that use the LumiCal to complement the electromagnetic calorimeter coverage further optimisation is possible.

For an optimal luminosity measurement the polar angle reconstruction plays a very important role. Figure 67 shows the polar angle resolution σ_θ for well reconstructed electrons in the polar angle range between 50 mrad and 75 mrad. For 1.5 TeV electrons a polar angle resolution of about 20 µrad is achieved. The resolutions are obtained from Gaussian fits to the distribution of $\theta_{\text{rec}} - \theta_{\text{MC}}$ for electron energies above 100 GeV. Below this energy the distribution is non-Gaussian and the RMS of the distribution is used instead.

The energy resolution for the LumiCal is shown in Figure 68. The RMS_{90} of the distribution $E_{\text{rec}} - E_{\text{MC}}$ is used for all energies, due to the long non-Gaussian tails introduced by the pad selection criteria.

The reconstruction efficiencies for the BeamCal at 380 GeV and 3 TeV CLIC are shown in Figure 69. At 380 GeV even the highest energy electrons are only reconstructed with 100% efficiency above 25 mrad. At lower radii the backgrounds are so large that only a fraction of the electrons can be reconstructed. However, as Figure 70(left) shows there are only a few low energy fake clusters reconstructed so the threshold to select pads can be reduced, which will increase the reconstruction efficiencies.

For 3 TeV, electrons above 1 TeV are reconstructed with high efficiency starting around 12 mrad. Between 12 mrad and 22 mrad the biggest loss of efficiency is due to the cutout in the BeamCal sensors due to the incoming beam pipe. Beyond 22 mrad all electrons above 1 TeV are reconstructed. 500 GeV electrons can only be reconstructed above 18 mrad. The initial 10% efficiency at the lower edge of the BeamCal for 500 GeV electrons is enhanced by the large background which pushes the energy deposits from the electron above the threshold for reconstruction. The fake rate in the BeamCal at 3 TeV (shown in Figure 70(right)) is also below 10^{-4}. Due to the aggressive rejection of background energy deposits the polar angle (Figure 71) and energy resolutions (Figure 72) are much worse than for the LumiCal. For the BeamCal polar angle resolutions, the RMS of the $\theta_{\text{rec}} - \theta_{\text{MC}}$ distribution is used for all energies. The RMS_{90} of the $E_{\text{rec}} - E_{\text{MC}}$ distributions is used to obtain the energy resolutions.

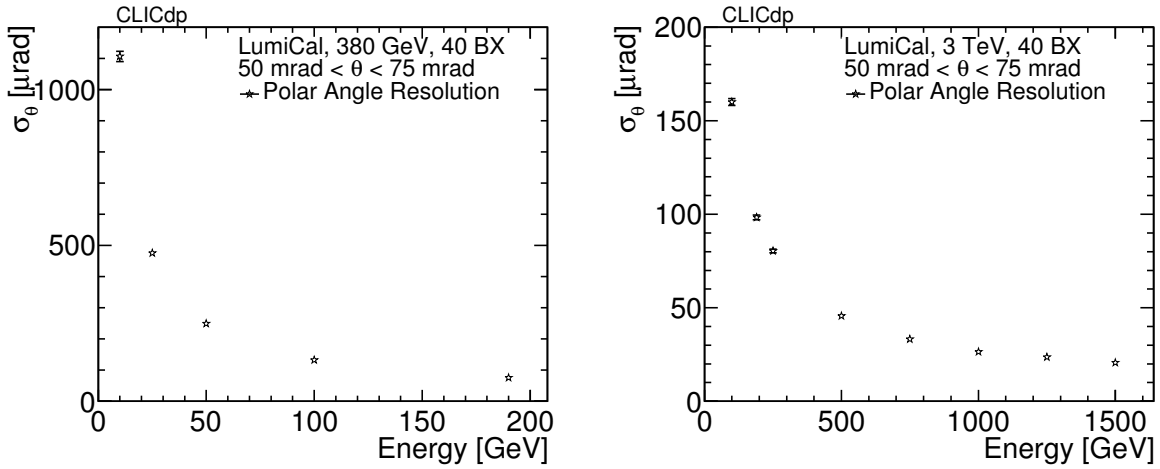

Figure 67: Polar angle resolution of reconstructed electrons as a function of the electron energy in the LumiCal at 380 GeV (left) and 3 TeV (right).

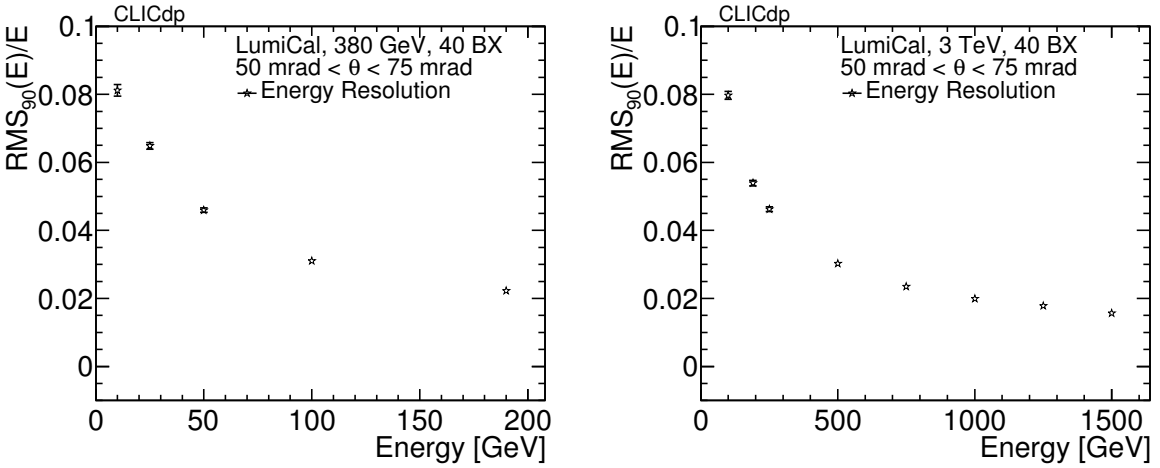

Figure 68: Energy resolution of reconstructed electrons as a function of the electron energy in the LumiCal at 380 GeV (left) and 3 TeV (right).

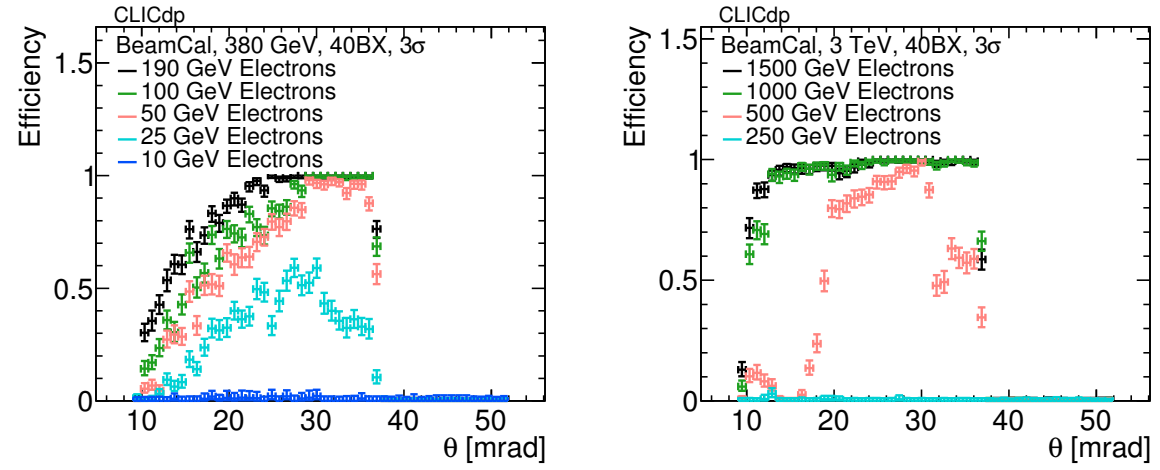

Figure 69: Reconstruction efficiency for electrons as a function of the polar angle in the BeamCal for 380 GeV (left) and 3 TeV (right).

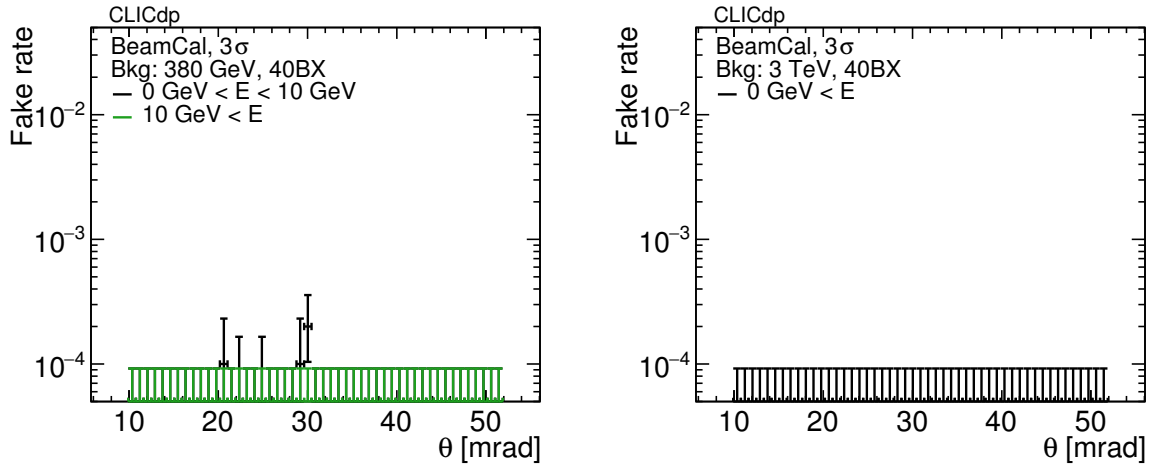

Figure 70: Fake rate for electron reconstruction as a function of the polar angle in the BeamCal at 380 GeV (left) and 3 TeV (right).

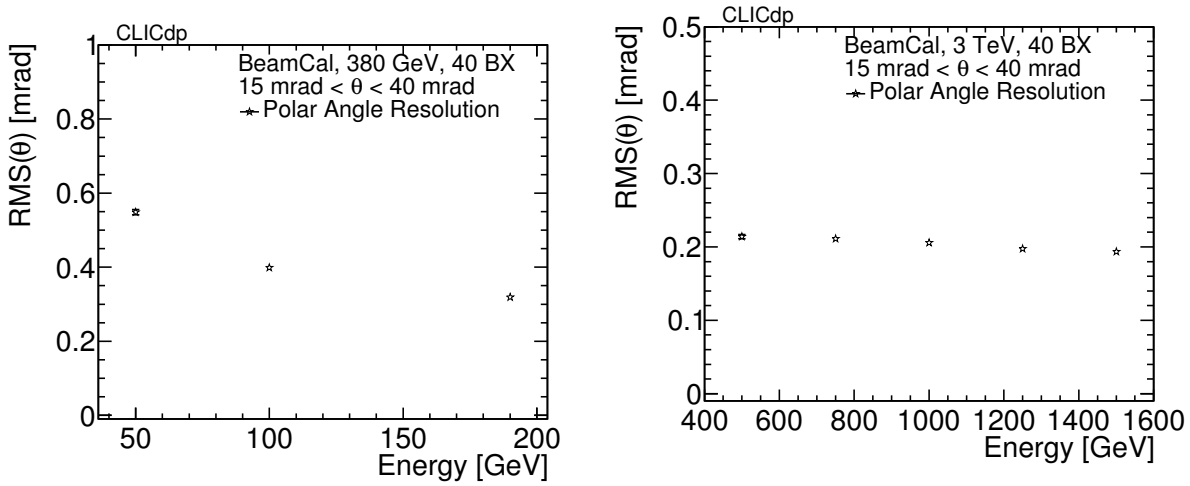

Figure 71: Polar angle resolution of reconstructed electrons as a function of the electron energy in the BeamCal at 380 GeV (left) and 3 TeV (right).

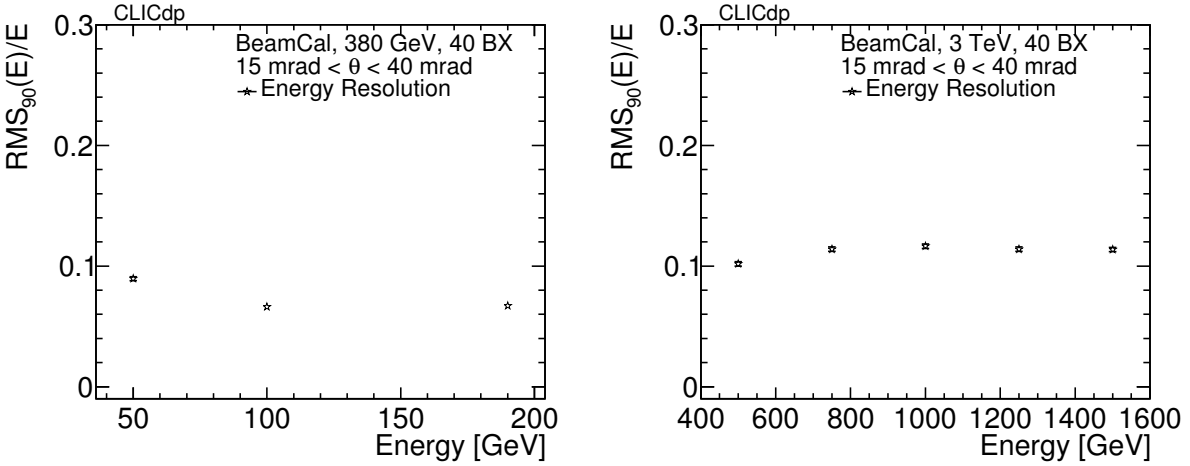

Figure 72: Energy resolution of reconstructed electrons as a function of the electron energy in the BeamCal at 380 GeV (left) and 3 TeV (right).

4.2.8. Forthcoming Studies and Improvements

In the near future, improvements are foreseen in terms of tracking and particle flow reconstruction, as already introduced in Section 4.2.6.

Concerning the tracking, a systematic study is planned to assess the quality of the Kalman filter fit. This effort is expected to improve especially low energy tracks, which have hits correctly assigned by the pattern recognition but rejected by the fit. As a consequence, the fake rate is also expected to decrease.

Possible improvements of the particle flow reconstruction are partially linked to better track reconstruction. Fewer *ghost* tracks and better track parameter reconstruction results in a better link between tracks and clusters. Improvements in the track reconstruction are therefore expected to translate in improved jet energy resolutions. A second area of improvements for particle flow reconstruction are the selection criteria for using tracks.

Finally, better track and particle flow reconstruction will certainly improve the flavour tagging performances.

5. Summary

An overview of the recent CLIC detector model (CLICdet) has been given, together with updated results of beam–beam backgrounds at 380 GeV and 3 TeV CLIC. Occupancies in the CLICdet subdetectors resulting from these backgrounds have been shown. In the case of the HCAL endcap, the high occupancies found need further studies, e.g. to mitigate back- or re-scattering of particles from the very forward region into the HCAL.

The detector performance has been illustrated with a series of results from single particle studies, covering momentum, position and angular resolution as well as particle identification efficiencies. Studies using more complex events (light flavour $Z/\gamma^* \to q\bar{q}$ events, $b\bar{b}$, $t\bar{t}$) show the performance without and with $\gamma\gamma \to$ hadron background overlaid with the physics events. Detailed investigations of the jet energy resolution at all jet energies up to 1.5 TeV, using software compensation, have been performed, and the separation of W and Z mass peaks has been studied. First results for the efficiency and possible contaminations in b- and c-tagging have been obtained, and forthcoming work to improve the performance in this domain has been outlined. Finally, the performance of the very forward electromagnetic calorimeters for electron tagging has been demonstrated.

Acknowledgements

This project has received funding from the European Union's Horizon 2020 Research and Innovation programme under Grant Agreement no. 654168. This work benefited from services provided by the ILC Virtual Organisation, supported by the national resource providers of the EGI Federation. This research was done using resources provided by the Open Science Grid, which is supported by the National Science Foundation and the U.S. Department of Energy's Office of Science.

A. Illustration of Selected Angles

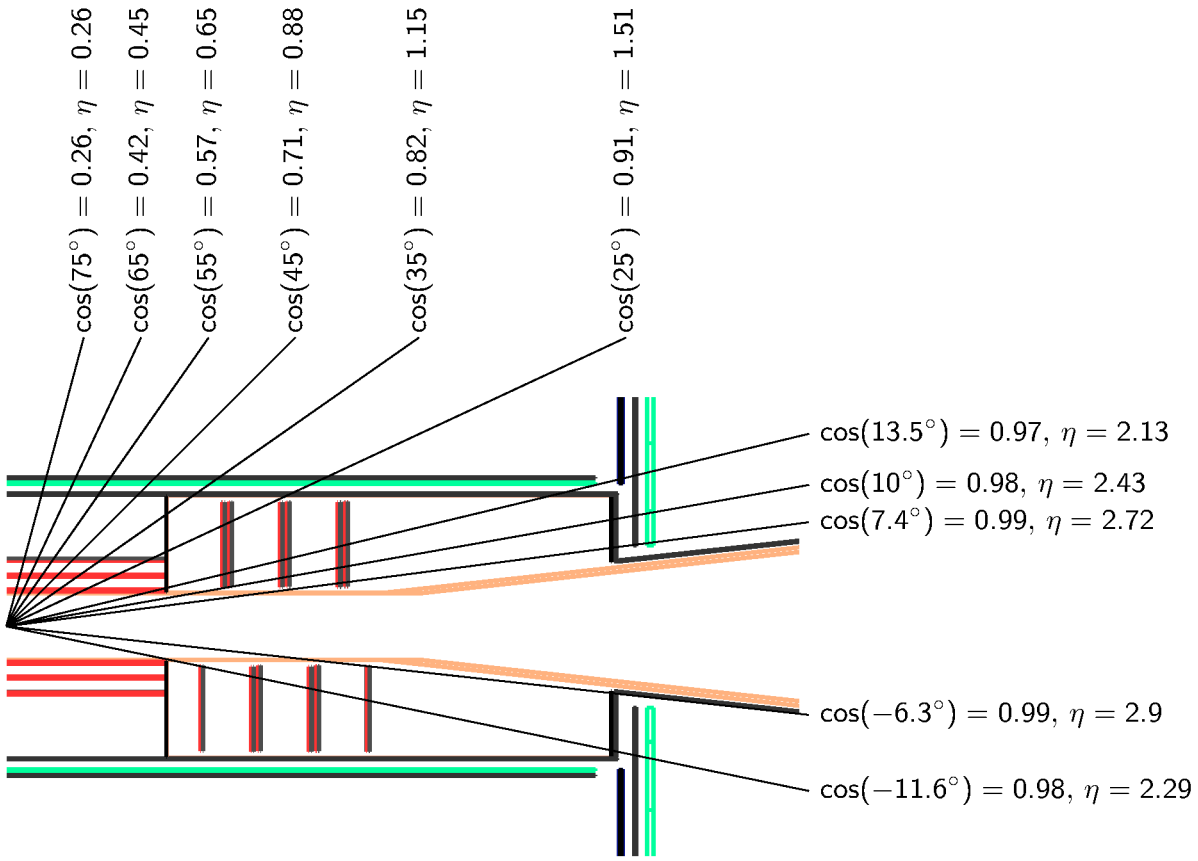

Figure A.1: Illustration of selected angles in the vertex region of CLICdet.

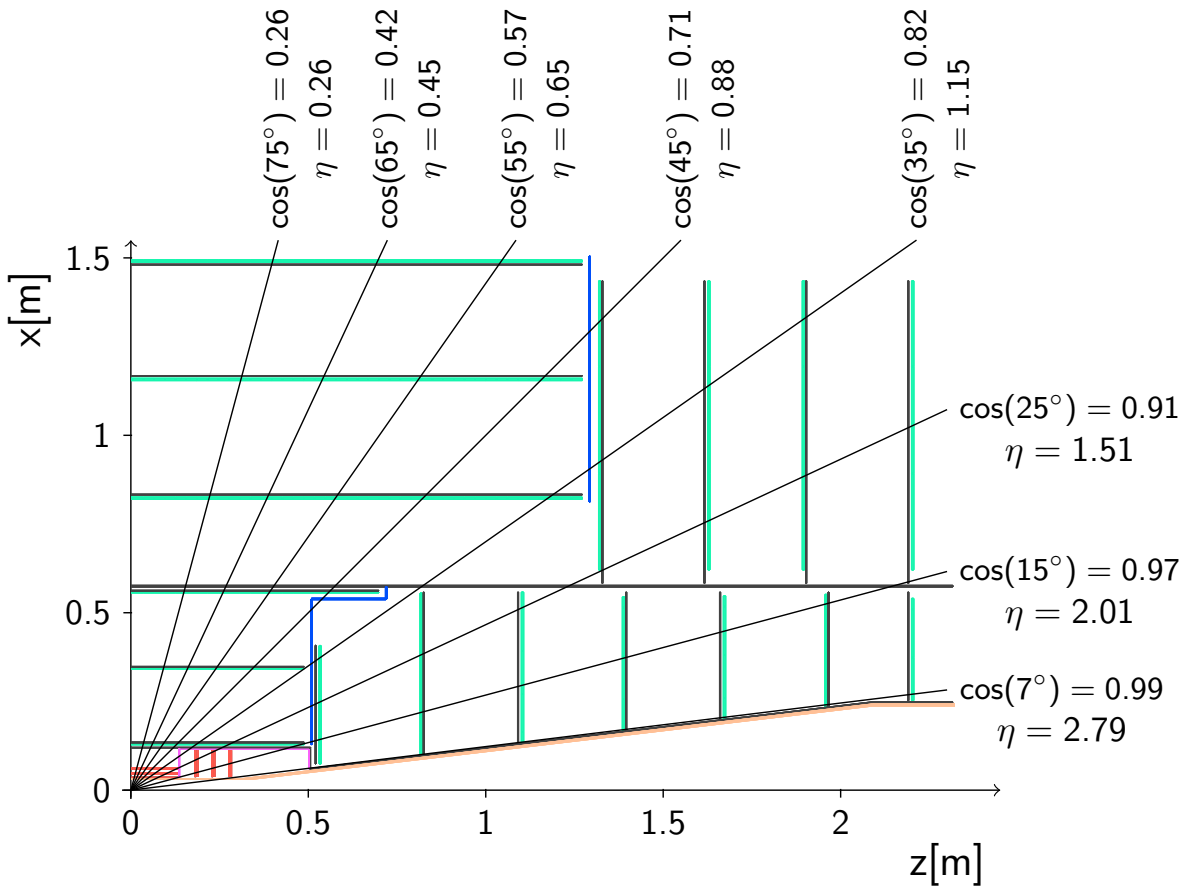

Figure A.2: Illustration of selected angles in the tracker region of CLICdet.

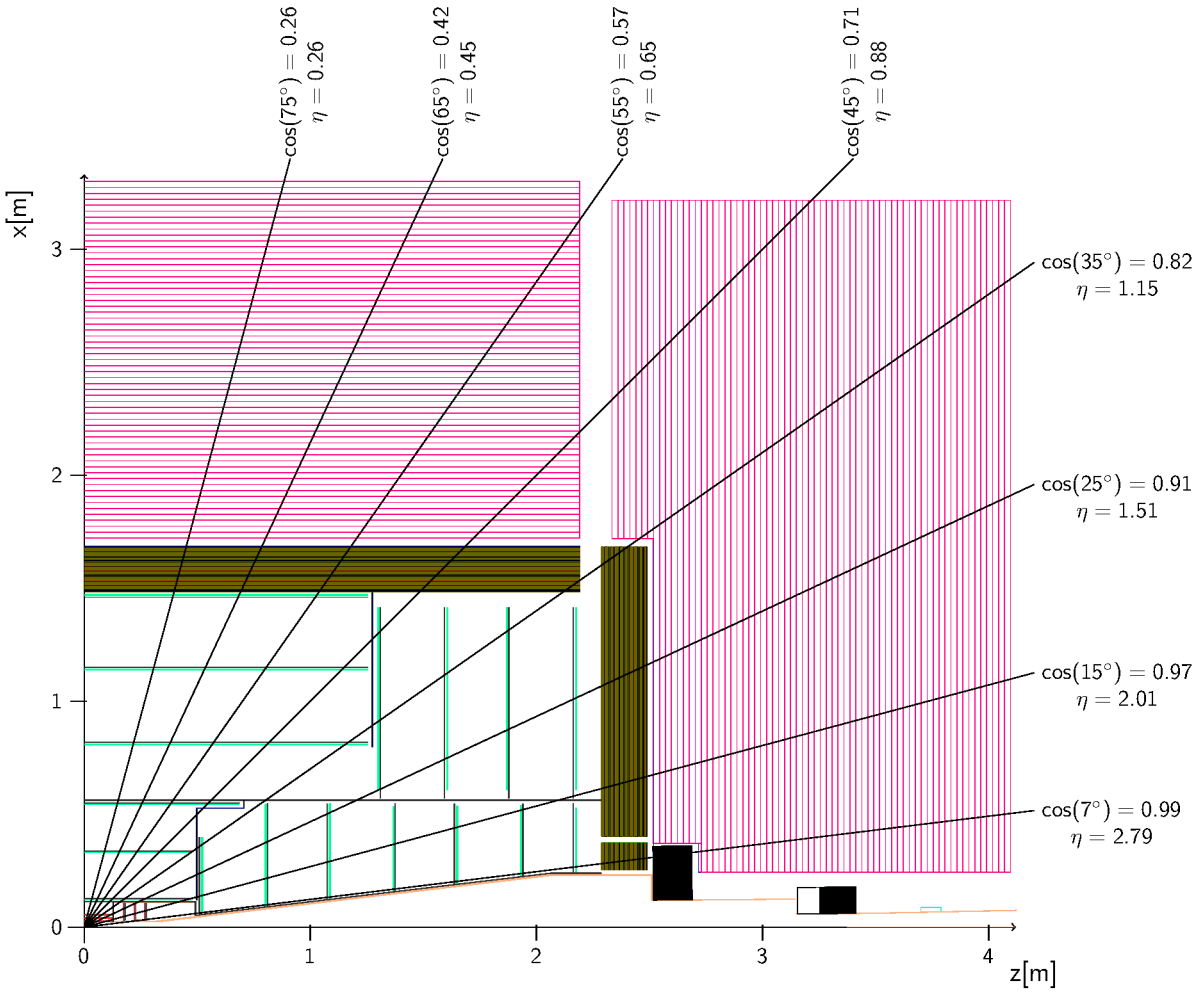

Figure A.3: Illustration of selected angles in CLICdet.

B. Deposited Background Energies in the Calorimeters

Table B.1: Raw deposited energy from beam-induced backgrounds in the CLICdet calorimeters. The numbers correspond to the background for an entire CLIC bunch train and nominal background rates. Safety factors representing the simulation uncertainties are not included.

Energy stage	380 GeV		3 TeV	
Subdetector	Incoherent pairs [GeV]	$\gamma\gamma \to$ hadrons [GeV]	Incoherent pairs [GeV]	$\gamma\gamma \to$ hadrons [GeV]
ECAL barrel	3.6	2.1	14	52
ECAL endcaps[a]	11	9.4	39	250
HCAL barrel	0.05	0.18	0.22	5.0
HCAL endcaps	2874	7.0	11 790	310
ECAL&HCAL	2889	19	11 840	620
LumiCal	69	4.5	280	190
BeamCal	54 730	5.6	270 600	540

[a] Including the ECAL plugs

C. Jet Energy Resolution Plots with Different Y-Axis Ranges

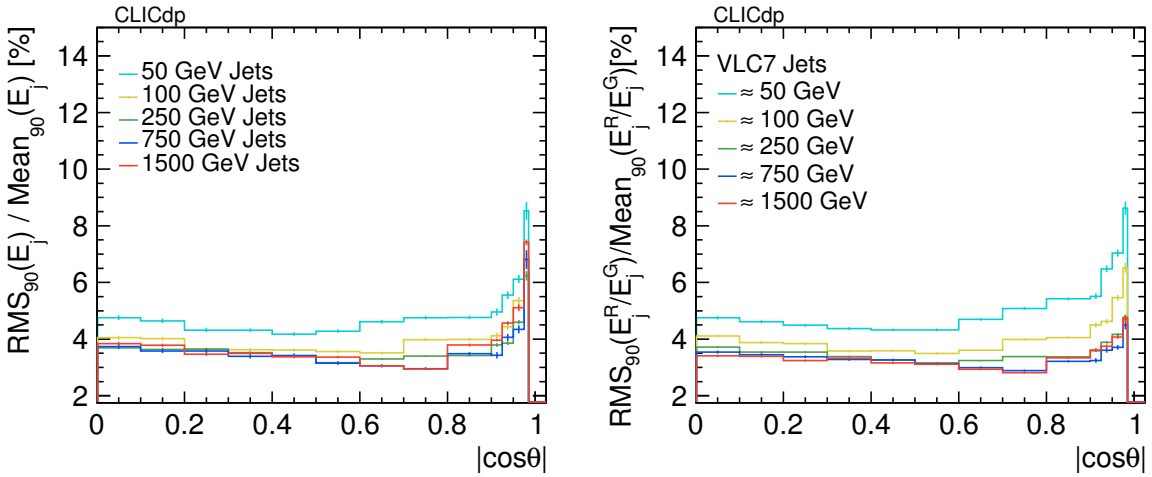

Figure C.1: Jet energy resolution distributions for various jet energies as a function of the $|\cos\theta|$ of the quark using two methods. The first method compares the total reconstructed energy with the energy sum from all visible particles on MC truth (left). The second method compares the jet energy of reconstructed jets and matched MC truth particle jets, using the VLC algorithm with an $R = 0.7$ (VLC7, right)

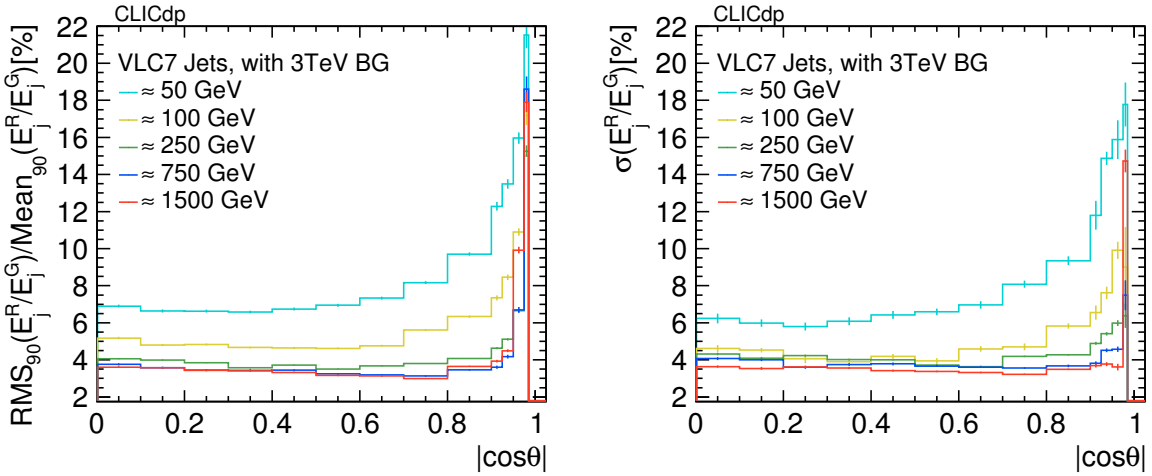

Figure C.2: Jet energy resolution for various jet energies as a function of the $|\cos\theta|$ of the quark with 3 TeV $\gamma\gamma \to$ hadron background overlaid on the physics di-jet event. In the first method RMS_{90} is used as measure of the jet energy resolution (left), the standard deviation σ of the Gaussian core of the double-sided Crystal Ball fit quantifies the jet energy resolution in the second method (right). Tight PFO selection cuts are used.

References

[1] L. Linssen et al., eds., *CLIC Conceptual Design Report: Physics and Detectors at CLIC*, CERN-2012-003, 2012, DOI: 10.5170/CERN-2012-003, arXiv: 1202.5940 [physics.ins-det].

[2] N. Alipour Tehrani et al., *CLICdet: The post-CDR CLIC detector model* (2017), CLICdp-Note-2017-001, URL: https://cds.cern.ch/record/2254048.

[3] A. Nurnberg, D. Dannheim, *Requirements for the CLIC tracker readout* (2017), CLICdp-Note-2017-002, URL: https://cds.cern.ch/record/2261066.

[4] J. Marshall, M. Thomson, *The Pandora Software Development Kit for Pattern Recognition*, Eur. Phys. J. **C75** (2015) 439, DOI: 10.1140/epjc/s10052-015-3659-3, arXiv: 1506.05348 [physics.data-an].

[5] M. A. Thomson, *Particle Flow Calorimetry and the PandoraPFA Algorithm*, Nucl. Instrum. Meth. **A611** (2009) 25, DOI: 10.1016/j.nima.2009.09.009, arXiv: 0907.3577 [physics.ins-det].

[6] J. S. Marshall, A. Münnich, M. Thomson, *Performance of Particle Flow Calorimetry at CLIC*, Nucl. Instrum. Meth. **A700** (2013) 153, DOI: 10.1016/j.nima.2012.10.038, arXiv: 1209.4039 [physics.ins-det].

[7] P. Burrows et al., eds., *Updated baseline for a staged Compact Linear Collider*, CERN-2016-004, 2016, DOI: 10.5170/CERN-2016-004, arXiv: 1608.07537 [physics.ins-det].

[8] R. B. Appleby et al., *Background and Energy Deposition Studies for the CLIC Post-Collision Line*, 2nd International Particle Accelerator Conference (IPAC), EuCARD-CON-2011-016, San Sebastián, Spain, 2011, URL: https://cds.cern.ch/record/1403134.

[9] S. van Dam, A. Sailer, *The occupancy in the Hadronic Calorimeter endcap of the CLIC detector* (2014), CLICdp-Note-2014-004, URL: https://cds.cern.ch/record/1751528.

[10] M. Frank et al., *DD4hep: A Detector Description Toolkit for High Energy Physics Experiments*, J. Phys. Conf. Ser. **513** (2013) 022010, DOI: 10.1088/1742-6596/513/2/022010.

[11] A. Tsaregorodtsev et al., *DIRAC: a community grid solution*, J. Phys. Conf. Ser. **119** (2008) 062048, DOI: 10.1088/1742-6596/119/6/062048.

[12] C. Grefe et al., *ILCDIRAC, a DIRAC extension for the Linear Collider community*, J. Phys. Conf. Ser. **513** (2013) 032077, DOI: 10.1088/1742-6596/513/3/032077.

[13] T. Sjöstrand, S. Mrenna, P. Skands, *PYTHIA 6.4 physics and manual*, JHEP **05** (2006) 026, DOI: 10.1088/1126-6708/2006/05/026, arXiv: hep-ph/0603175 [hep-ph].

[14] W. Kilian, T. Ohl, J. Reuter, *WHIZARD: Simulating Multi-Particle Processes at LHC and ILC*, Eur. Phys. J. **C71** (2011) 1741, DOI: 10.1140/epjc/s10052-011-1742-y, arXiv: 0708.4233 [hep-ph].

[15] M. Moretti, T. Ohl, J. Reuter, *O'Mega: An optimizing matrix element generator*, 2001, arXiv: hep-ph/0102195 [hep-ph].

[16] D. Schulte, *Study of Electromagnetic and Hadronic Background in the Interaction Region of the TESLA Collider*, PhD thesis, University of Hamburg, 1996.

[17] S. Agostinelli et al., *Geant4 – A Simulation Toolkit*, Nucl. Instrum. Meth. **A506** (2003) 250, DOI: 10.1016/S0168-9002(03)01368-8.

[18] J. Allison et al., *Geant4 developments and applications*, IEEE T. Nucl. Sci. **53** (2006) 270, DOI: 10.1109/TNS.2006.869826.

[19] J. Allison et al., *Recent developments in Geant4*, Nucl. Instrum. Meth. **A835** (2016) 186, DOI: 10.1016/j.nima.2016.06.125.

[20] M. Frank et al., *DDG4: A Simulation Framework using the DD4hep Detector Description Toolkit*, J. Phys. Conf. Ser. **664** (2015) 072017, DOI: 10.1088/1742-6596/664/7/072017.

[21] F. Gaede, *Marlin and LCCD: Software tools for the ILC*, Nucl. Instrum. Meth. **A559** (2006) 177, DOI: 10.1016/j.nima.2005.11.138.

[22] A. Sailer et al., *DD4Hep Based Event Reconstruction*, J. Phys. Conf. Ser. **898** (2017) 042017, DOI: 10.1088/1742-6596/898/4/042017.

[23] P. Schade, A. Lucaci-Timoce, *Description of the signal and background event mixing as implemented in the Marlin processor OverlayTiming*, LCD-Note-2011-006, 2011, URL: https://cds.cern.ch/record/1443537.

[24] E. Leogrande, *Conformal tracking for the CLIC detector*, 4th International Workshop Connecting The Dots, CLICdp-Conf-2018-004, Seattle, Washington, 2018, URL: https://cds.cern.ch/record/2630512.

[25] M. Hansroul, H. Jeremie, D. Savard, *Fast circle fit with the conformal mapping method*, Nucl. Instrum. Meth. **270** (1988) 498, DOI: 10.1016/0168-9002(88)90722-X.

[26] M. B. Kennel, *KDTREE 2: Fortran 95 and C++ software to efficiently search for near neighbors in a multi-dimensional Euclidean space*, arXiv: physics/0408067 [physics.data-an].

[27] A. Sailer, A. Sapronov, *High Energy Electron Reconstruction in the BeamCal* (2017), CLICdp-Note-2016-005, arXiv: 1702.06945 [physics.ins-det].

[28] E. Brondolin, A. Sailer, *Optimization of timing selections at 380 GeV CLIC* (2018), CLICdp-Note-2018-003, URL: https://cds.cern.ch/record/2645355.

[29] C. Adloff et al., *Hadronic energy resolution of a highly granular scintillator-steel hadron calorimeter using software compensation techniques*, JINST **7** (2012) P09017, DOI: 10.1088/1748-0221/7/09/P09017.

[30] H. Tran et al., *Software compensation in Particle Flow reconstruction*, Eur. Phys. J. **C77** (2017) 698, DOI: 10.1140/epjc/s10052-017-5298-3, arXiv: 1705.10363 [physics.ins-det].

[31] C. Buttar et al., *Standard Model Handles and Candles Working Group: Tools and Jets Summary Report*, Physics at TeV colliders, La physique du TeV aux collisionneurs, Les Houches 2007 : 11–29 June 2007, 2008, p. 121, arXiv: 0803.0678 [hep-ph].

[32] M. Boronat et al., *Jet reconstruction at high-energy electron–positron colliders*, Eur. Phys. J. **C78** (2018) 144, DOI: 10.1140/epjc/s10052-018-5594-6, arXiv: 1607.05039 [hep-ex].

[33] M. Cacciari, G. P. Salam, G. Soyez, *FastJet User Manual*, Eur. Phys. J. **C72** (2012) 1896, DOI: 10.1140/epjc/s10052-012-1896-2, arXiv: 1111.6097 [hep-ph].

[34] M. Oreglia, *A Study of the Reactions $\psi' \to \gamma\gamma\psi$*, PhD thesis, SLAC, 1980, URL: http://www-public.slac.stanford.edu/sciDoc/docMeta.aspx?slacPubNumber=slac-r-236.

[35] F. James, *MINUIT Function Minimization and Error Analysis: Reference Manual Version 94.1* (1994).

[36] I. Antcheva et al.,
ROOT: A C++ framework for petabyte data storage, statistical analysis and visualization,
Comput. Phys. Commun. **180** (2009) 2499, DOI: 10.1016/j.cpc.2009.08.005,
arXiv: 1508.07749 [physics.data-an].

[37] M. Weber, *Jet Performance at CLIC* (2018), CLICdp-Note-2018-004,
URL: https://cds.cern.ch/record/2648827.

[38] M. Aaboud et al.,
Jet reconstruction and performance using particle flow with the ATLAS Detector,
Eur. Phys. J. **C77** (2017) 466, DOI: 10.1140/epjc/s10052-017-5031-2,
arXiv: 1703.10485 [hep-ex].

[39] V. Khachatryan et al.,
Jet energy scale and resolution in the CMS experiment in pp collisions at 8 TeV,
JINST **12** (2017) P02014, DOI: 10.1088/1748-0221/12/02/P02014,
arXiv: 1607.03663 [hep-ex].

[40] N. Alipour Tehrani, P. Roloff, *Optimisation Studies for the CLIC Vertex-Detector Geometry* (2014), CLICdp-Note-2014-002, URL: https://cds.cern.ch/record/1742993.

[41] T. Suehara, T. Tanabe, *LCFIPlus: A Framework for Jet Analysis in Linear Collider Studies*,
Nucl. Instrum. Meth. **A808** (2016) 109, DOI: 10.1016/j.nima.2015.11.054,
arXiv: 1506.08371 [physics.ins-det].